Mimicking opioid analgesia in cortical pain circuits

Justin G. James[1†], Nora M. McCall[1†], Alex I. Hsu[4,5†], Corinna S. Oswell[1], Gregory J. Salimando[1], Malaika Mahmood[1], Lisa M. Wooldridge[1], Meghan Wachira[1], Adrienne Jo[1], Raquel Adaia Sandoval Ortega[1], Jessica A. Wojick[1], Katherine Beattie [3], Sofia A. Farinas [1], Samar N. Chehimi [1], Amrith Rodrigues [3], Lindsay L. Ejoh [1], Blake A. Kimmey[1], Emily Lo[1], Ghalia Azouz [11], Jose J. Vasquez [11], Matthew R. Banghart [12], Kate Townsend Creasy [4], Kevin T. Beier [11], Charu Ramakrishnan [7], Richard C. Crist [1], Benjamin C. Reiner [1]*, Karl Deisseroth [7,8,9,10]*, Eric A. Yttri [5,6]* ✉, Gregory Corder [1,2,3]* ✉

[1]Dept. of Psychiatry, Perelman School of Medicine, University of Pennsylvania, Philadelphia, PA, USA
[2]Dept. of Neuroscience, Perelman School of Medicine, University of Pennsylvania, Philadelphia, PA, USA
[3]Dept. of Anesthesiology and Critical Care, Perelman School of Medicine, University of Pennsylvania, Philadelphia, PA, USA
[4]Dept. of Biobehavioral Health Sciences, School of Nursing, and Translational Medicine and Human Genetics, Perelman School of Medicine, University of Pennsylvania, Philadelphia, PA, USA
[5]Dept. of Biological Sciences, Carnegie Mellon University, Pittsburgh, PA, USA
[6]Neuroscience Institute, Carnegie Mellon University, Pittsburgh, PA, USA
[7]CNC Program, Stanford University, Stanford, CA, USA
[8]Dept. of Bioengineering, Stanford University, Stanford, CA, USA
[9]Howard Hughes Medical Institute, Stanford University, Stanford, CA, USA
[10]Dept. of Psychiatry & Behavioral Sciences, Stanford University, Stanford, CA, USA
[11]Dept. of Physiology and Biophysics, University of California Irvine, CA, USA
[12]Dept. of Neurobiology, School of Biological Sciences, University of California San Diego, CA, USA

†Co-First Authors
*Co-Senior Authors
✉Correspondence: gcorder@upenn.edu (G.C.) & eyttri@andrew.cmu.edu (E.A.Y.)

Abstract.

The anterior cingulate cortex plays a pivotal role in the cognitive and affective aspects of pain perception. Both endogenous and exogenous opioid signaling within the cingulate mitigate cortical nociception, reducing pain unpleasantness. However, the specific functional and molecular identities of cells mediating opioid analgesia in the cingulate remain elusive. Given the complexity of pain as a sensory and emotional experience, and the richness of ethological pain-related behaviors, we developed a standardized, deep-learning platform for deconstructing the behavior dynamics associated with the affective component of pain in mice—LUPE (Light aUtomated Pain Evaluator). LUPE removes human bias in behavior quantification and accelerated analysis from weeks to hours, which we leveraged to discover that morphine altered attentional and motivational pain behaviors akin to affective analgesia in humans. Through activity-dependent genetics and single-nuclei RNA sequencing, we identified specific ensembles of nociceptive cingulate neuron-types expressing mu-opioid receptors. Tuning receptor expression in these cells bidirectionally modulated morphine analgesia. Moreover, we employed a synthetic opioid receptor promoter-driven approach for cell-type specific optical and chemical genetic viral therapies to mimic morphine's pain-relieving effects in the cingulate, without reinforcement. This approach offers a novel strategy for precision pain management by targeting a key nociceptive cortical circuit with on-demand, non-addictive, and effective analgesia.

Introduction.

Pain is a complex aversive sensory perception, fundamental to adaptive survival *(1)*. Understanding the cognitive and emotional features of pain is crucial for advancing targeted treatments for individuals with pathological pain conditions *(2, 3)*. Current analgesic drugs, such as opioids, bathe the body in chemical compounds, acting on widely expressed molecular targets that promote serious and fatal side effects. By pinpointing specific brain neural circuits for pain-associated aversion, which intersect with the expression of the mu-opioid receptor (MORs) *(4)*—the molecular target of morphine—a new class of effective analgesics can be developed that interfere with the unpleasantness of pain rather than pain sensation, with reduced addiction and respiratory depression side effects *(5, 6)*.

Coordinated neural activity in the anterior cingulate cortex (ACC), and its connected brain regions, are involved in directing attention and anticipating the presentation of salient noxious stimuli, in moment-to-moment behavior switching and future avoidance *(7, 8)*. Immediately, the perception of pain alerts one of a threat and elicits orientation towards the threatening stimulus or injured tissue. Following this orientation, these nociceptive signals are rapidly evaluated and contextualized by recurrent neural circuits for valence and threat-detection to employ an appropriate motivational response—escape, withdrawal, recuperative attending *(9)*. Thus, by quantifying the frequency and transitions between these innate pain-related behaviors, classified as protective or nocifensive, we gain insight into the brain circuitries involved in moment-to-moment neural processes that can provide meaningful information on possible brain targets to therapeutically disrupt pain. Indeed, the ACC is important for encoding the emotional and motivational aspects of pain *(10–16)*. Ablation of the ACC alleviates the emotional suffering of chronic pain patients, but it does not affect their ability to evaluate the intensity of their pain *(17–20)*. Similarly, lesions *(21, 22)*, opioids *(23–26)*, and optogenetic manipulation *(27–33)* of ACC neural circuits attenuate aspects of the affective component of the pain, as shown by a reduction in conditioned place avoidance and aversive behaviors induced by noxious stimuli. In total, these studies point to the same neural circuits in the ACC that drive adaptive behavior to acute noxious stimuli might also be maladaptive during chronic pain *(34, 35)*. Thus, leveraging personalized deep-brain stimulation *(36)* or cell-type-specific gene therapies *(37, 38)* to modulate neural activity in MOR-expressing neurons *(39)* may mimic the prefrontal cortical actions of opioid analgesia without the associated risks of off-target pharmacotherapies *(1)*.

Results.

A standardized machine-vison and deep-learning system for complex pain behaviors.

The complexity of pain cannot be fully assessed, for example, by reflexive withdrawal behaviors—the current standard for preclinical analgesic efficacy evaluation in rodents that assess neither sensory nor affective-evaluative perceptual features of pain, but merely nociceptive intensity detection by peripheral-spinal microcircuits *(40–42)*. Likewise, conditioned place aversion/preference assays *(21, 43, 44)* measure memory recall for pain and analgesic reinforcement but miss acute nociception-driven motivational responses to noxious stimuli, as well as how these behaviors change with experience to represent different behavior strategies *(1)*. To fill the gaps between these classic behavioral pharmacology assays, we set to improve the sensitivity and rigor of assessing pain-related behaviors, in trial-to-trial measurements across different exposures to noxious stimuli. Thus, we developed a new tool, LUPE, to capture and analyze both evoked and spontaneous nocifensive behaviors (**Fig. 1A** and **S1A-I**). The Light aUtomated Pain Evaluator—named for the Algea daemon of Pain & Suffering (λῦπη)—is a standardized, dark/safe environment for nocturnal, prey mice. LUPE removes the human experimenter—both as a looming threat administering noxious stimuli, and as the data-acquirer providing subjective determination of putative pain responses—with greater focus placed on quantifying and detecting the dynamic transition of ethological motor and nocifensive behaviors in freely moving mice as a primary metric to determine "*pain*", or lack thereof as "*analgesia*."

Beyond the standardized LUPE chamber (**Fig. S2**), the analysis algorithm is derived from DeepLabCut (DLC) *(45)* key-point tracking of 20 body points paired with supervised A-SOiD *(46)* and unsupervised B-SOiD *(47)* algorithms, yielding six holistic behavior repertoires (*Still, Walk, Rear, Groom, Lick Left Hindpaw, Lick Right Hindpaw*), built from subsecond behavior syllables (**Fig. 1B,C** and **S1**). To evaluate the quantitative and temporal sensitivity of LUPE to detect dynamic sequences of pain-related behaviors we first used the classic formalin test of acute pain *(48)*. Male and female C57Bl6/J mice were placed within the chamber for two consecutive habituation days (**Fig. S3A**) and then intraplantar injected with either 1% or 5% formalin into the left hindpaw, compared to no-injury control conditions (**Fig. 1D**). LUPE calculated the behavior use probabilities for each of the six repertoires within 1-minute bins across the 30-minute recordings for all n=60 mice in <120-minutes, compared to 50-150-minutes for human BORIS scoring of one behavior for one mouse (upper-bound time for manual scoring = 54,000 minutes for this dataset; **Fig. S1E**). LUPE-generated raster plots, instance and duration, and transition matrices highlight the rapid, moment-to-moment behavior selection in response to noxious chemical stimuli (**Fig. 1E** and **Fig. S4-9**). We observed a stimulus intensity-dependent increase of the probability use and total seconds of the *Lick Left Hindpaw* repertoire for 1% vs. 5% left intraplantar formalin, which tracked the expected temporal increases during Phase-1 (1-10 min) and Phase-2 (10-30 min) (**Fig. 1F**). We next compared the broadly used intraplantar capsaicin test by injecting the TRPV1-agonist into the right hindpaw and observed significant *Lick Right Hindpaw* use and total seconds of engagement (**Fig. 1F**) *(49)*.

Thus, LUPE increases speed, rigor, and reproducibility in preclinical behavioral pain research by accurately tracking behavior dynamics with high precision in a standardized, replicable environment, with the extended benefit of creating loggings of all video recorded behaviors and computer-scored results for long-term record-keeping, and cross-lab verification or re-evaluation of published data.

Morphine disrupts attentional-directed behavior selection during pain experiences.

In rodents, morphine reduces mechanical and thermal nociceptive thresholds at injected doses of ≥10+mg/kg of body weight *(50)*. The recommended initial analgesic dose of morphine sulfate injection in an average human adult is ≥10 mg/70-kg for mild-to-severe pain *(51)*, making the animal equivalent dose 0.23 mg/kg. Accounting for metabolic species differences *(52)*, the rodent 10 mg/kg dose needed to alter sensory thresholds is ~43-fold higher than those used in clinical practice. It is important to note that elevated withdrawal thresholds are not a primary endpoint for opioid analgesia in humans, rather morphine reduces subjective ratings for affective and evaluative ratings *(53, 54)* via action in the medial cortices *(23, 24, 55)*. Thus, we re-evaluated the dose-response analgesic efficacy of morphine to

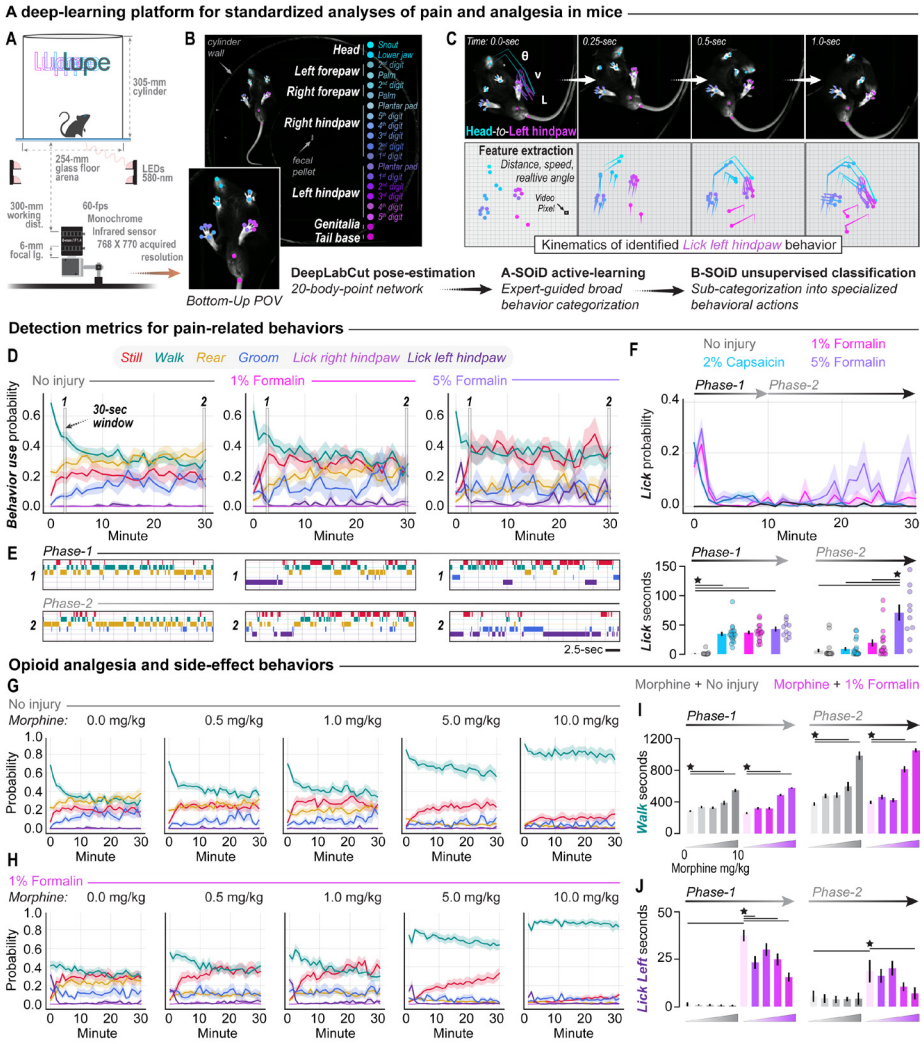

Figure 1. Automated quantification of pain-related behaviors, opioid analgesia, and drug side effects.

(A) The standardized LUPE platform and chamber for high-speed infrared videography. **(B)** A 20-body point DeepLabCut pose-tracking model was built from a bottom-up camera for male & female mouse pain behavior. **(C)** Behavior segmentation models trained iteratively on supervised annotations of holistic behaviors (*e.g.,* licking *vs.* grooming *vs.* walking *vs.* rearing etc.) with A-SOiD are then further subclustered using an unsupervised classification with B-SOiD. **(D)** Temporal probability plots for each of the six primary behavior repertoires in 1-min bins in uninjured mice compared to a left hindpaw injection of the noxious chemical irritant formalin. **(E)** Raster plots of rapidly switching behaviors in a 30-sec window across Phase-1 *vs.* Phase-2 of the formalin test. **(F)** Comparison of injured hindpaw recuperative licking probability and equivalent seconds of active licking in response to injected formalin or capsaicin. **(G,H)** Effects of escalating morphine doses on each behavior repertoire in uninjured (G) or formalin injured (H) mice. **(I)** Summary of altered walking hyperlocomotion to escalating morphine and/or formalin injury exposures. **(J)** Summary of altered nocifensive licking to escalating morphine and/or formalin injury exposures. N=20/group, except n=10 for 5% formalin conditions. One-way ANOVA + Tukey for panels F, I, J. ★ = P < 0.05. Errors bars = s.e.m.

modify the use-probability and pattern of LUPE behavior repertoires in the formalin test. We found that, alone, 5- and 10-mg/kg morphine (intraperitoneal injection) greatly increases *Walk* use probability and distance traveled, while suppressing engagement in the other five repertoires (**Fig. 1G** and **Fig. S4,S5**). In comparison, 0.5- and 1.0-mg/kg morphine does not measurably alter any behavior in no-injury conditions. Following 1% formalin left-hindpaw injection, 5- and 10-mg/kg morphine reduced *Lick Left* use probabilities and total seconds in Phase-1 and Phase-2, while simultaneously biasing the near sole-engagement of the *Walk* repertoire (**Fig. 1H** and **Fig. S4-9**). Counter to previous manual scoring reports, LUPE detected that 0.5 and 1.0-mg/kg morphine reduced formalin-induced affective-motivational licking behavior without the hyperlocomotion confounds of higher doses (**Fig. 1H** and **Fig. S4-9**).

Thus, we infer that the decades' prior use of translationally non-relevant, high-doses of morphine in rodents was likely selected and optimized to modify reflexive detection metrics that are not reflective of the human pain experience and do not assess the effect of morphine on pain affective-evaluative dimensions. In support of this conclusion, opioids produce intense muscle rigidity and hindlimb electromyographic activity *(56, 57)*, as well as stimulant-like hyperlocomotion that massively alter gait and paw-placement *(58)* that obscure accurate measurements with hand-applied filament or thermal probes, or hot-plate chambers. These hyperlocomotive and limb "stiffness" side effects were apparent with 5- and 10- mg/kg injections, but not seen with 0.5- and 1.0-mg/kg morphine. Comparatively, 0.5-mg/kg morphine produces a CPP effect in rats with peripheral nerve injury *(25)* and restores inflammation pain-suppressed wheel running *(59)*, both indirect measures of pain affect alleviation. Combined with our LUPE observations, the use of non-reinforcing *(60)*, 0.5-1.0-mg/kg morphine instills an affective-analgesia that reduces the selection of attentional recuperative behaviors (*e.g.*, directed licking the effected somatic tissue), which we interpret as an imperfect but improved, indirect measure of pain unpleasantness in non-verbal mouse models *(1, 50, 61, 62)*. Although, how and where in the nervous system does morphine interfere with nociception to produce the property of affective analgesia *(50)*?

Mapping an ACC nociceptive hotspot embedded in a brain-wide network that is engaged during chronic pain.

Given the high density of MORs in the ACC *(63–65)* and opioid-induced changes in pain affect in humans and rodents *(25, 53)*, we first sought to first generate a comprehensive atlas of nociceptive, or pain-active, ACC neurons. To begin, we used the TRAP2 activity-dependent transgenic mouse for nociceptive neural tagging (*pain*TRAP) *(1, 66)* via repeated noxious 55ºC water drops to trigger the immediate early gene *Fos* promoter and 4-hyrdoxytamoxifen-inducible Cre recombinase (**Fig. 2A**). In a fluorescent tdTomato reporter line, *pain*TRAP neurons were found across the entire anterior-posterior axis of the ACC, as well as the dorsal (Cg1) and ventral (Cg2) subregions and cortical layers (**Fig. 2B** and **Fig. S10**). However, we identified a peak hotspot of *pain*TRAP neurons within a ~700-µm anterior ACC coordinate (+1.69 – +0.97-mm AP), relative to no-stimulus control mice (*home-cage*TRAP; **Fig. 2C**). This hotspot was located anterior to the mid-cingulate→posterior-insula circuit for sensory-reflexive behaviors *(67, 68)* (**Fig. 2A-D**). Within this "nociceptive hotspot", the contralateral Cg1 Layer 2/3 showed the greatest effect size of noxious stimuli on *pain*TRAP tagging, while Cg1 Layers 5 and 6 were also engaged to a lesser degree, and with variable tagging in Cg2 (**Fig. 2D**). Importantly, two-weeks after the permanent *pain*TRAP fluorophore tagging, these mice were re-exposed to the same 55ºC stimuli, in a new environment, to observe potential re-activation of the *pain*TRAP network via immunostaining nociceptive FOS protein induction (*pain*FOS). Relative to the *home-cage*TRAP controls, we found a 2.3 fold increase in co-labeled *pain*FOS/*pain*TRAP ACC neurons within the nociceptive hotspot (**Fig. 2B,C**), suggesting that *pain*TRAP gains genetic access to a subset of nociceptive ACC cell-types that are re-engaged across pain experiences.

Distinct neural ensembles discriminating negative vs. positive valence processes exist within the prefrontal cortex, which we tagged in response to foot-shocks vs. cocaine exposure, respectively *(69)*. Here, we compared the negative valence *pain*TRAP ensembles to those tagged during positive valence, mating opportunity—*sex*TRAP (**Fig. S11E-G**). We found little overlap between *sex*TRAP tagged neurons and *pain*FOS responsive populations in Cg1. Indeed, most of the *sex*TRAP neurons were localized to the ventral Cg2 region, further highlighting a segregation of valence ensembles. Neural computations are executed by networks, or systems of neurons connected across brain regions, so we next assessed the brain-wide axonal projections of *pain*TRAP ACC neurons compared to all ACC projection pathways using a dual viral anterograde tracing approach. We found that both functionally nociceptive and the total population of cell-types target numerous cortical, subcortical, and brainstem regions, but that there is not a "pain-specific" output or bias for *pain*TRAP neurons to target distinct downstream brain regions (**Fig. S12**).

Chronic pain disorders are linked to changes in both the structure and function of the brain that may differ from those involved in acute pain. To investigate the evolution of brain activity as pain transitions from acute to chronic, we next investigated the larger brain-wide nociceptive network using *pain*TRAP and *pain*FOS mapping with lipid clearing and light-sheet imaging (**Fig. 2E**). Initially, *pain*TRAP neurons were tagged with a nuclear Sun1-sfGFP fluorescent label. These mice either remained uninjured or underwent transection of the left sciatic nerve (SNI, Spared Nerve Injury model: spared sural *(66)*) to induce chronic neuropathic pain. After 3-weeks, we induced FOS before collecting the brains: the injured and neuropathic groups were split again to receive no-stimulus (*home-cage*FOS or *hc*FOS), noxious 55ºC water drops to the left hindpaw

(*pain*FOS), or a light-touch mechanical stimulus to the injured left hindpaw (0.16-g filament; *touch*FOS). After lipid clearing, immunohistochemistry, and light-sheet imaging, an automated algorithm quantified the regional density and pattern of the *pain*TRAP-sfGFP and FOS-expressing cells across 1,100+ unique brain subregions. Analyzing regional increases in *pain*FOS in uninjured mice relative to uninjured *hc*FOS controls, we again found robust engagement of the bilateral anterior ACC nociceptive hotspot (**Fig. 2F *upper right*, 2G *upper left***). Similarly, *touch*FOS in neuropathic pain mice showed increased activity in the contralateral ACC nociceptive hotspot relative to *hc*FOS in neuropathic mice (**Fig. 2F *lower right*, 2G *lower right***). As we observed significant acute *pain*TRAP re-engagement by subsequent acute *pain*FOS (**Fig. 2B**), we next evaluated if the acute *pain*TRAP neurons would also be engaged weeks after SNI by stimuli evoking mechanical allodynia (*touch*FOS). In this brain-wide re-analysis, mechanical allodynia re-engaged a substantial number of *pain*TRAP ACC neurons (**Fig. 2H *lower left***), even more than *pain*FOS re-stimulation in uninjured mice (**Fig. 2I *lower left***), despite inducing lower total FOS counts (**Fig. 2G *upper right***).

From this large-scale nociceptive brain map, we limited further analyses to brain regions implicated in nociceptive processing by the human pain fMRI literature. Specifically,

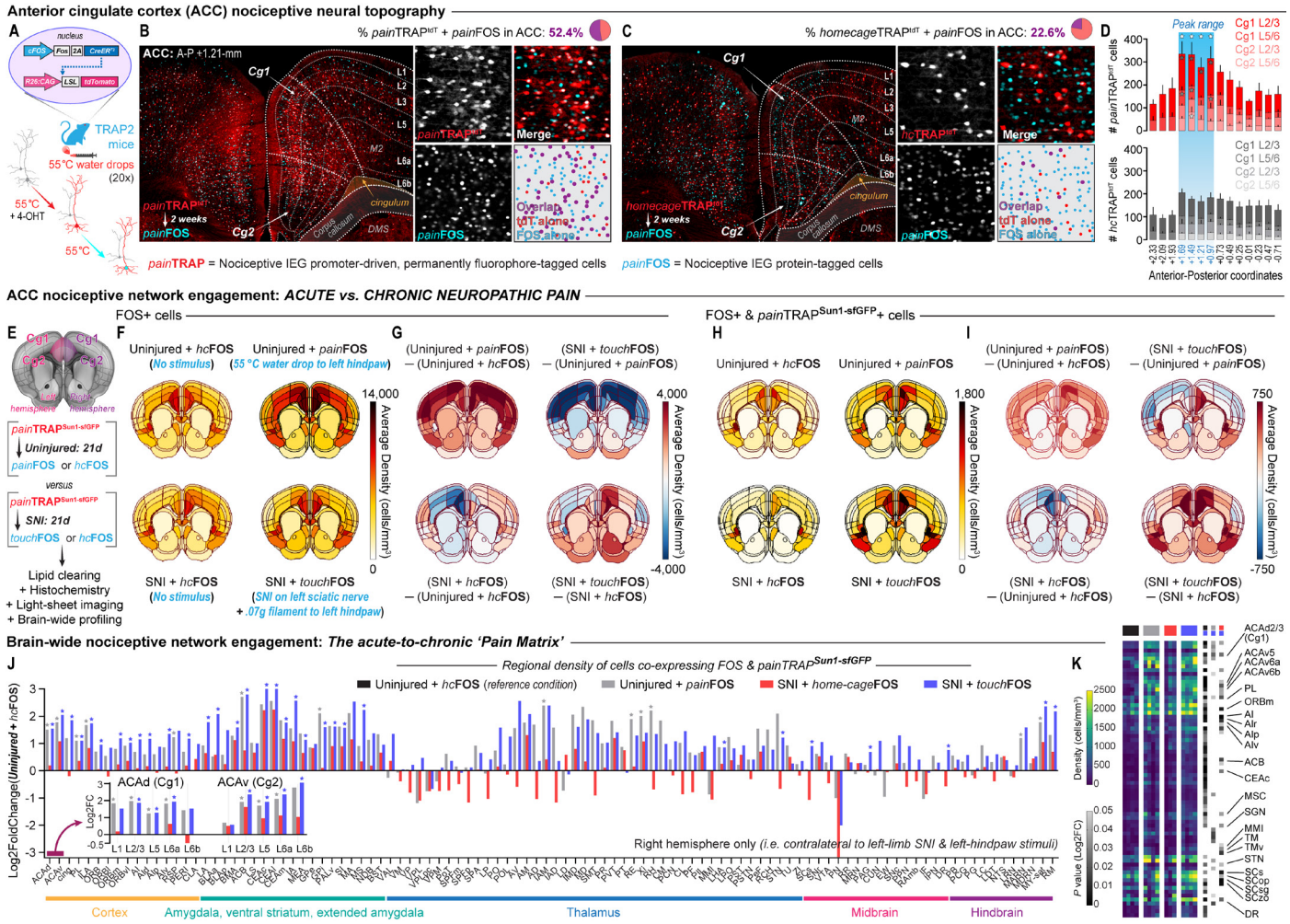

Figure 2. Nociceptive ensembles in the cingulate cortex and across the brain-wide pain matrix.

(A) TRAP2 mice for activity-dependent genetic capture and permanent fluorescent tagging of nociceptive cell-types (*pain*TRAP) and noxious re-engagement visualized with the immediate early gene, FOS (*pain*FOS). **(B,C)** ACC *pain*TRAP tagging and *pain*FOS co-expression, compared to a no-stimulus control condition (*home-cage*TRAP). **(D)** Quantification of *pain*TRAP cells across all layers of the dorsal Cg1 and ventral Cg2, displayed across the entire anterior-posterior extent of the ACC; n=6 male and 6 female per condition. **(E)** Design for whole-brain clearing, light-sheet imaging and regional analysis of *pain*TRAP-Sun1-sfGFP labeled nuclei, and acute *vs.* chronic neuropathic pain FOS from noxious thermal or light-touch stimuli, respectively; n=3-4 males per condition. **(F)** FOS density in the ACC. **(G)** FOS density differences between conditions. **(H)** Density of cells co-expressing *pain*TRAP-Sun1-sfGFP and FOS. **(I)** Density differences between the co-labeled cells across conditions. **(J)** Highlighted brain regions from human fMRI pain studies show the log2 fold change in the brain region density of co-labeled *pain*TRAP-Sun1-sfGFP and FOS relative to the control *Uninjured + hcFOS* condition; $p < 0.05$, no multiple comparison correction. **(K)** Density heatmap comparing the co-labeled density of *pain*TRAP and *touch*FOS in neuropathic pain mice (blue group) relative to all other conditions.

we focused on brain regions within the "pain neuromatrix"*(70)* / Neurological Pain Signature (NPS)*(71)* network encoding the intensity of nociceptive stimuli, as well as the Stimulus Intensity Independent Pain Signature (SIIPS)*(72)* network for pain modulation, which includes the prefrontal cortices (**Fig. 2J**). Normalizing the patterns of co-labeled FOS/*pain*TRAP-Sun1-sfGFP in the uninjured *hc*FOS conditions, we found distinct areas in the right contralateral hemisphere, significantly engaged by acute noxious stimuli (*pain*FOS) but not neuropathic allodynia (SNI + *touch*FOS), such as the thalamic nuclei (interanteromedial, reuniens, xiphoid, and rhomboid) and the magnocellular reticular nucleus (MARN; **Fig 2J**). Otherwise, we found that both acute and neuropathic noxious stimuli activated similar brain-wide regions, largely within the SIIPS regions, in particular the prefrontal cortices (ACC Cg1 and Cg2, prelimbic, orbitofrontal, and insula), nucleus accumbens, and the central-/basolateral-amygdala (**Fig. 2J, inset**). However, relative to the uninjured + *pain*FOS nociceptive pattern, neuropathic mechanical allodynia significantly engaged the acute *pain*TRAP ensemble within Layer 2/3 of dorsal ACC Cg1 (**Fig. 2K**), further implicating the ACC superficial layers in both acute and chronic pain nociceptive processes.

Cingulate cartography of opioidergic and nociceptive cell-types.

To identify the ACC pain-processing cell-types that co-express MORs as potential cellular mediators of morphine analgesia, we next used single-nuclei RNA sequencing to transcriptionally profile this cingulate nociceptive ensemble. Based on the *pain*TRAP hotspot peak noxious coordinates (**Fig. 2D**), we collected bilateral ACC tissue punches in this range (n=4 per condition) from mice with either no-injury or neuropathic pain for 3-days, 3-weeks, or 3-months (bilateral Spared Nerve Injury, SNI *(73)*) for subsequent Differential Expressed Gene (DEG) analysis over the chronic pain development/maintenance timepoints *(74)*. Importantly, 5-min prior to tissue collection we stimulated all mice with a light-touch 0.16-g filament to evoke multiple immediate early gene (IEG) cascades for subsequent "activity scoring" and IEG density mapping *(75, 76)*, and then processed samples for single-nuclei RNA sequencing with the 10X Genomics 3' Gene Expression assay (**Fig. 3A**). All ACC samples were collected and processed on the same day to avoid batch effects. After quality-control steps, we analyzed 104,302 single nuclei and identified 23 distinct cell-type clusters across all expected major cell classes (*e.g.*, neurons, microglia, astrocytes, *etc.*; **Fig. 3B**). Nuclei from all conditions were equally distributed across the 23 clusters, with the one exception of fewer nuclei from the SNI 3-month condition in the parvalbumin (*Pv*) cluster *(77)* (**Fig. 3C** and **Fig. S13**). Based on known cell-class and ACC layer-defining marker genes we parsed the clusters into 14 glutamatergic neuronal, three GABAergic neuronal, and six non-neuronal clusters (**Fig. 3D**).

We plotted the expression of the mu-, delta-, kappa- and nociception- opioid receptors (*Oprm1, Oprd1, Oprk1, Oprl1*, respectively) and the opioid peptides: pre-pro-enkephalin, pro-dynorphin, pro-opiomelanocortin, and pre-pro-nociceptin (*Penk, Pdyn, Pomc, Pnoc*, respectively; **Fig. 3E**) *(78)*. Importantly, *Oprm1* was largely expressed in an increasing graded pattern across glutamatergic pyramidal cell-types, going from the Layer 2/3 intratelencephalic (IT) clusters to the Layer 6 corticothalamic (CT) clusters (**Fig. 3E, H**). Limited *Oprm1* was found in somatostatin (*Sst*) and vasoactive intestinal polypeptide (*Vip*) GABAergic interneurons *(79, 80)*. To localize putative nociceptive cell-types, we used two measures of noxious-evoked IEGs—a weighted distribution 'activity score' and IEG density mapping with Nebulosa of n=25 IEGs (**Fig. 3F,G**). Only three of the 23 cell-types showed increases in IEG panel expression: Cluster 3: L2/3 IT-3, Cluster 6: L5 IT-1, and Cluster-13: L6 CT-2.

As the snRNAseq analysis shows a distribution of *Oprm1* and noxious IEG+ cell-types across all layers of the ACC, we next used fluorescent *in situ* hybridization (FISH) and HALO deep-learning histology quantification to refine the location of opioidergic nociceptive neurons (**Fig. 3I-K** and **Fig. S14,S15**). In male and female C57Bl6/J mice, ~71% of all ACC Cg1 *Oprm1*+ cells co-expressed the glutamatergic pyramidal neuron marker, *Slc17a7* (9,488 of 13,047 *Oprm1*+ cells). The number of *Oprm1*+ cells was near equivalent across layers, but the percentage of total cells within each layer and the density of mRNA transcripts per cell showed a similar increasing graded pattern to the snRNAseq analysis (**Fig. 3J,K**). Similar to *pain*TRAP counts (**Fig. 2**), noxious-induced *Fos* mRNA (*painFos*) was highest in Cg1 Layer 2/3, and ~25% of Cg1 Layer 2/3 *Oprm1*+ cells co-expressed *painFos* (**Fig. 3J**). In compliment, we used an *Oprm1*-2A-Cre;Sun1-sfGFP mouse to tag the lineage population of ACC MOR+ cell-types and assess *pain*FOS across the layers. Again, we found that that Cg1 Layer 2/3 had the largest average percentage of MOR/*pain*FOS co-expressing cells (**Fig. 3L-N** and **Fig. S16**). In the snRNAseq dataset, the L2/3 IT-3 cell-type with the densest IEG score, express several marker genes (*i.e., Baz1a, Penk, Otof*)*(81)*, as well as *Slc17a7* and *Oprm1*. Double FISH for *painFos* and *Otof* co-register primarily in the outer-most Layer 2 (**Fig. 3O**). To refine our understanding of these ACC cell-types, we compared the genetic and functional markers to see if brain-wide connectivity would further pinpoint their identity. To link transcriptomic identities with axonal projections, we compared published databases of PFC CTB-retro labeling *(82, 83)*, the PFC projectome *(84)*, and the PFC Retro-Seq dataset *(85)*. These datasets confer that the nociceptive L2/3 IT-3 cluster is comprised partly of superficial Layer-2 glutamatergic IT neurons expressing *Penk* and *Otof* that project to the BLA (**Fig. S13**). Indeed, a subset of ACC *pain*TRAP axons innervate the BLA in a discrete anterior-medial subnucleus that we previously found to be an amygdalar hot-spot of stable-encoding nociceptive, negative valence-tuned neurons that are necessary for affective-motivational acute and chronic pain behaviors *(66, 86)*.

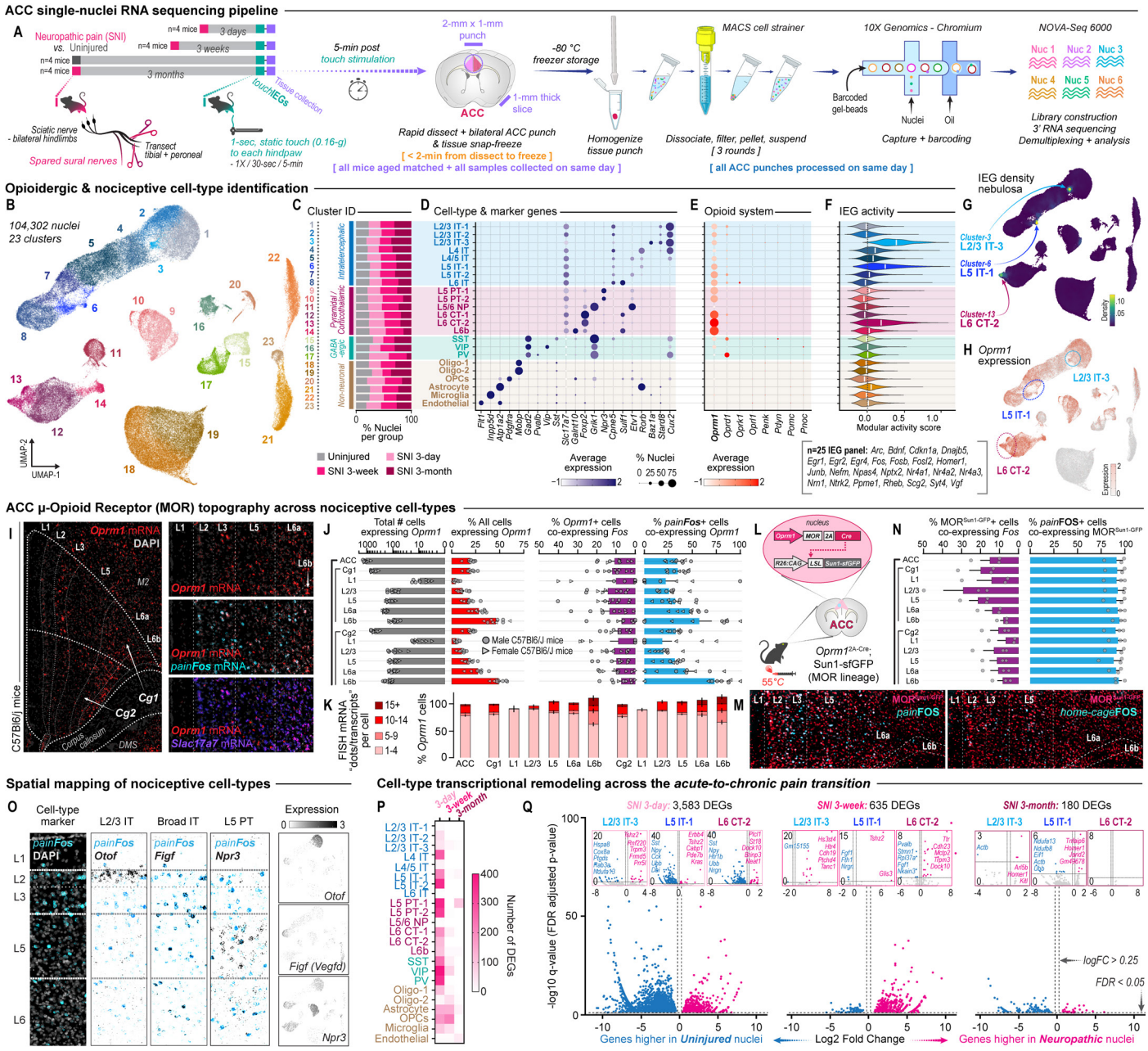

Figure 3. Transcriptomic classification of nociceptive and opioidergic cell-types in the cingulate.

(A) Design of single-nuclei RNA sequencing experiments from ACC punches of mice with bilateral sciatic nerve transections collected after different timepoints of chronic pain development and light-touch-evoked immediate early genes (IEGs); n=4 male mice per condition. **(B)** Dimensionality reduction plot of all nuclei from all groups in 23 cell-type clusters. **(C)** Broad classification of all clusters into neuronal and non-neuronal classes with the percentage of nuclei per condition in each cluster. **(D)** Specific cell-type identities and dot-plot for selected marker genes. **(E)** Dot plot for all opioid receptors and peptides. **(F)** Nociceptive activity score per cluster based on a panel of n=25 IEGs. **(G)** Nebulosa density plot of the IEG panel overlaying the UMAP of cell-type clusters. **(H)** Feature plot for *Oprm1* expression. **(I)** Fluorescent *in situ* hybridization (FISH) for *Oprm1* mRNA, noxious-evoked *Fos* mRNA, and *Slc17a7* mRNA in uninjured male and female mice. **(J)** Noxious-evoked *Fos* mRNA and *Oprm1* mRNA co-expressing ACC cells. **(K)** *Oprm1* mRNA transcripts per cell, per ACC layer. **(L,M)** Fluorescent labeling of MOR lineage populations with an Oprm1-2A-Cre;Sun1-sfGFP mouse. **(N)** Noxious-evoked FOS and MOR co-expressing ACC cells. **(O)** FISH for ACC layer marker genes co-expressing noxious-evoked *Fos* mRNA, and feature plots for the layer cell-type markers *Otof*, *Figf* and *Npr3*. **(P)** Number of up- and down-regulated, differential expressed genes (DEGs) per cell-type cluster across the development of chronic neuropathic pain. **(Q)** Volcano plots for all DEGs across the chronic pain time course with insets highlighting DEGs for the three most noxious IEG-response cell-type clusters.

Neuropathic pain does not leave a lasting transcriptomic imprint on ACC cell-types.

While our whole-brain anatomical mapping of *pain*TRAP and neuropathic *touch*FOS co-responsive cells suggest the ACC is engaged in acute and chronic pain states, the long-term genetic changes in the ACC accompanying peripheral nerve injury remain unclear. To test this, we performed differential expression analysis to identify high-confidence transcriptomic changes across the 3-day, 3-week, and 3-months post-SNI groups using a pseudo-bulk approach with edgeR (false discovery rate [FDR] < 0.05 and $\log_2$ fold change [FC] > |0.25|) for each cell-type cluster and injury time-point compared to the uninjured cell-types. At 3-days post-SNI we noted 3,583 DEGs, with 43, 208 and 184 DEGs for the *pain*IEG+ clusters, L2/3 IT-3, L5 IT-1 and LC CT-2, respectively. Within these three *pain*IEG+ clusters, synaptic gene ontology (SynGO) analysis revealed that the down- and up-regulated genes in each neuronal cell-type were related to pre- and post-synaptic ribosomal functions and translation, synapse organization, and synaptic vesicle cycling *(87)* (**Fig. 3P** and **Fig. S17**). However, contrary to bulk-sequencing reports *(88–90)*, by 3 weeks post-SNI and out to the 3-month timepoint, there were relatively few DEGs in each cell-type such that pathway analysis was not permissible (635 and 180 DEGs at 3-week and 3-month, respectively, across all cell-types; **Fig. 3P,Q**). Within the noxious IEG-defined clusters (**Fig. 3F,G**), increased *Homer1* was found at later timepoints in the Layer 2/3 IT-3 and Layer 5 IT-1 cell-types (**Fig. 3Q insets**), which has been implicated in chronic pain *(91)*. Nonetheless, the return of genetic programs to their uninjured naïve state within many ACC cell-types (despite the persistence of behavioral allodynia and hyperalgesia) aligns with dorsal root ganglia snRNAseq after nerve injury where peripheral nociceptors and other sensory afferent populations return to a naïve transcriptional state between 2-weeks and 2-months post-injury *(92)*. Furthermore, while some reports show decreased MOR expression in the mid-cingulate cortex with chronic pain *(93, 94)*, we did not detect changes in rostral cingulate *Oprm1* expression in any cell-type, at any of the SNI timepoints, which we confirmed via FISH in male and female mice (**Fig. S15**) *(95)*.

ACC MORs are necessary and sufficient for morphine analgesia.

From our three primary observations thus far—1) opioids preferentially modulate pain aversion (**Fig. 1**); 2) the ACC contains nociceptive cell-types (**Fig. 2**); and 3) *Oprm1* is highly expressed in many molecularly distinct ACC cell-types (**Fig. 3**)—we tested the hypothesis that morphine analgesia engages inhibitory signaling in ACC nociceptive *Oprm1*-expressing neural ensembles to reduce the selection of nocifensive behaviors during noxious events. First, to investigate the necessity of MORs for analgesia we injected an AAV-*hSyn*-eGFP-Cre into bilateral ACC of *Oprm1*$^{Flox/Flox}$ mice (**Fig. 4A**) to knockout exons 2 and 3 only in ACC neurons, while leaving all other MORs intact throughout the nervous system. Relative to AAV-*hSyn*-eGFP injected controls, Cre-mediated excision reduced *Oprm1* expression over 50% via qPCR (**Fig. 4B**). Mice were injected with 0.5-mg/kg morphine and assessed for analgesia 30-minutes later. While there were no alterations in von Frey mechanical thresholds in either group, *Oprm1* ACC deletion significantly reduced morphine-mediated attenuation of affective-motional behaviors (*i.e.,* summed durations of licking, guarding, and escape) in response to acute drops of noxious 55ºC water and acetone evaporative cooling (**Fig. 4C**). One week later, the same mice were tested on an inescapable 50ºC hotplate for 60-seconds, while high-speed cameras captured reflexive and affective-motivational behaviors (**Fig. 4H**). Again, *Oprm1* deletion reduced morphine analgesia, as illustrated by the greater duration of attending behavior engagement. Interestingly, for the inescapable hotplate assay, we noted that the temporal dynamics of nocifensive behaviors in wild-type mice without morphine progresses from an initial reflexive retraction of the hindpaw from the hotplate floor that quickly transitions to a bout of attending/licking within ~0.5-2.0-seconds. Morphine increased the time duration between the first reflexive withdrawal and the first attending bout to an average of 7.2-seconds, while ACC *Oprm1* deletion blocked this dissociative effect of morphine (**Fig. 2D *upper right***). Moreover, once mice with ACC *Oprm1* deletion started to engage in attending bouts, they spent a greater percentage of time staying engaged in active attending bouts (**Fig. 4D *lower left***). In the LUPE-scored 1% formalin test, *Oprm1* deletion increased Phase-2 Lick probability and number of *Lick* instances only in female mice given morphine (**Fig. 4E** and **Fig. S18**).

In compliment to *Oprm1* knockdown necessity tests, we next explored the sufficiency of ACC MORs for morphine analgesia by re-expressing human *OPRM1* (hMOR) in MOR total knockout mice. Using an *Oprm1*$^{Cre/Cre}$ line *(96)*, where the Cre recombinase coding sequence was knocked-in the *Oprm1* exon-1 to generate a global embryonic knockout in allelic homozygous mice, we injected an AAV-*Syn*-FLEx-mCherry-2A-hMOR that only expresses hMOR in the appropriate Cre-expressing neurons of the ACC *(97)* (**Fig. 4F**). Relative to AAV-*hSyn*-FLEx-eGFP injected controls, the re-expression vector significantly increased *ORPM1* via qPCR and mCherry immunofluorescence (**Fig. 4G**). We found that morphine (0.5-mg/kg) had no effect on analgesia or hyperlocomotion in the MOR KO mice, while re-expression restored morphine analgesia to disrupt noxious thermal affective-motivational behaviors but without hyperlocomotion (**Fig. 4H**). On the inescapable hotplate assay, hMOR re-expression + morphine increased the latency to engage in recuperative attending and the total amount of time spent attending, while reinstating morphine dissociation between reflexive and affective-motivational behavior engagement (**Fig. 4I**). In the LUPE-scored 1% formalin test, hMOR re-expression + morphine increased Phase-1 Lick probability but reduced it in Phase-2 only in female mice given morphine (**Fig. 4E** and **Fig. S19**).

Together these temporal changes in attentional recuperative licking behaviors suggest that morphine acts upon ACC MOR-expressing neurons to deprioritize pain-related aversion and the selection of nocifensive behavior repertoires.

Chemogenetic inhibition of ACC *Oprm1*+/nociceptive cell-types reduces aversive affective-motivational pain.

Morphine binding to MORs inhibits the receptor-expressing target cell by triggering intracellular Gαi/o signaling and a cascade of pathways that decrease neural firing

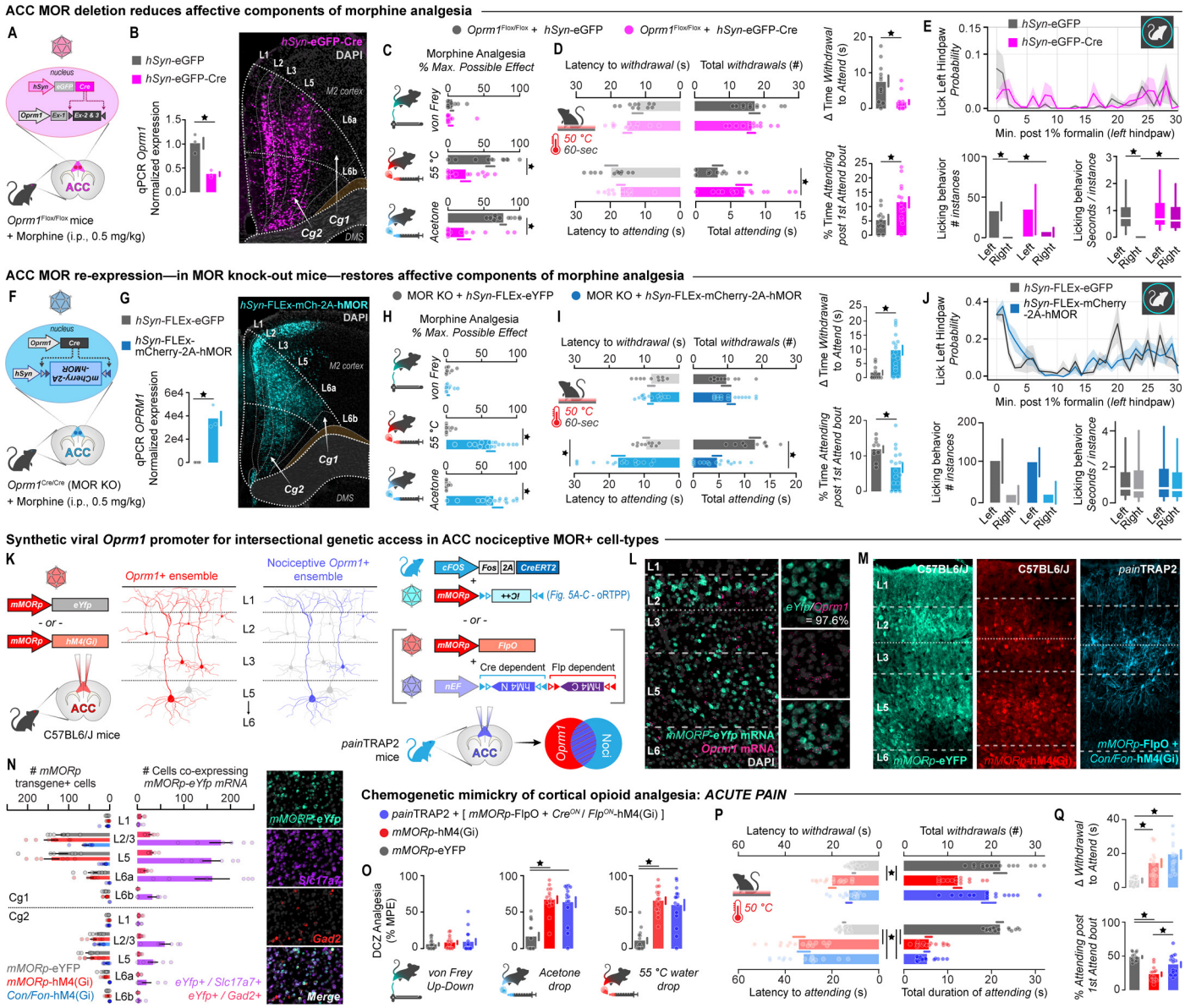

Figure 4. Morphine analgesia is mediated by action on ACC MOR+ cell-types that can be mimicked via viral MOR promoter-driven inhibitory chemogenetics.

(A) Design to virally-delete MORs from ACC neurons in *Oprm1*$^{Flox/Fox}$ mice. **(B)** ACC *Oprm1* qPCR (N=3 per group). **(C)** Morphine (0.5-mg/kg, i.p.) analgesia for mechanical and thermal noxious stimuli (N=11 *hSyn*-eGFP mice, N=14 *hSyn*-eGFP-Cre mice. **(D)** Behavior metrics for thermal thresholds and affective-motivational engagement on an inescapable hotplate after morphine. **(E)** Effects of morphine on LUPE-scored licking behavior in the 1% formalin test. **(F)** Design to virally re-express MORs in an embryonic MOR knockout mouse (N=10 null expression mice, N=16 re-expression mice). **(G)** ACC *OPRM1* qPCR (N=3 per group). **(H)** Morphine analgesia for mechanical and thermal noxious stimuli. **(I)** Behavior metrics for thermal thresholds and affective-motivational engagement on an inescapable hotplate after morphine. **(J)** Effects of morphine on LUPE-scored licking behavior in the 1% formalin test. **(K)** Strategies to deliver inhibitory chemogenetic actuators to MOR+ cell-types (Red: *mMORp*-hM4) or intersectional nociceptive-MOR+ cell-types (Blue: *mMORp*-FlpO + *Cre*^{ON}/*Flp*^{ON}-hM4 in *pain*TRAP mice). **(L)** Co-expression for *mMORp*-driven *eYFP* mRNA and endogenous *Oprm1* mRNA. **(M,N)** *mMORp*-driven fluorophore or hM4 transgene expression across ACC layers (M) with quantification (N, left) and co-expression with glutamatergic (*Slc17a7*) and GABAergic (*Gad2*) cell-type markers (N=6 per group). **(H)** Morphine analgesia for mechanical and thermal noxious stimuli. **(I)** Behavior metrics for thermal thresholds and affective-motivational engagement on an inescapable hotplate after morphine. Two-tailed Student's *t* test for all panels except, One-way ANOVA + Tukey for panels O, P, Q. ★ = P < 0.05. Errors bars = s.e.m.

(4). The class of inhibitory chemogenetic GPCRs, DREADD-hM4, engages similar Gαi/o signaling when the receptor binds to its synthetic agonist, deschloroclozapine (DCZ) *(98)*. As morphine analgesia is driven by MOR signaling in the ACC, we hypothesized that chemogenetic mimicry of morphine anti-nociception via selective inhibition of ACC MOR-expressing neurons would alleviate pain aversion in a circuit-specific manner. Using our recently published *(39)* synthetic mouse mu-opioid receptor promoter (*mMORp*) to gain genetic access to cortical MOR+ cell-types, we cloned the DREADD-hM4 sequence into the *mMORp* vector for AAV-mediated hM4 delivery directly to ACC MOR neurons (AAV-*mMORP*-hM4-mCherry; **Fig. 4K** and **Fig. S20**). In parallel, *mMORp* can be multiplexed with the *pain*TRAP2 mouse (*Fos*-FOS-2A-iCre^{ERT2}) for intersectional chemogenetic inhibition of nociceptive-MOR+ sub-types of neurons (**Fig. 4K**). This is achieved via an INTERSECT genetic approach by co-injected AAVs for *mMORp*-FlpO recombinase and *Cre^{ON}/Flp^{ON}*-hM4-mCherry *(99)*. We found that AAV-*mMORp* has ~97% selectively to express transgenes in the endogenous *Oprm1*+ ACC populations (**Fig. 4L** and **Fig. S20A**), with the greatest transduction in Cg1 *Slc17a7*+ glutamatergic cell-types (**Fig. 4N *right*** and **Fig. S2B-E**). Indeed, control mice expressing *mMORp*-eYFP and DREADD-expressing *mMORp*-hM4 mice showed similar transduction patterns across Layers 2/3, 5, and 6 (**Fig. 4M,N**), which closely matched the pattern seen with *Oprm1* FISH (**Fig. 3I,J**). Interestingly, the dual-dependency INTERSECT approach to express hM4 in *pain*TRAP/MOR+ neurons largely restricted DREADDs to Cg1 Layer 2/3 and superficial Layer 5 (**Fig. 4M,N**), where we observed the highest density of *pain*FOS and *pain*TRAP cells, as well as the *pain*IEG Layer 2/3 IT-3 and Layer 5 IT-1 cell-types (**Fig. 2** and **Fig. 3**).

To evaluate the effects of *mMORp*-driven chemogenetic mimicry of cortical analgesia on acute pain, all mice were injected with DCZ (0.3-mg/kg, i.p.) and tested 30-min later on a panel of behavior tests. We found that both *mMORp*-hM4 and the *mMORp*-FlpO/*pain*TRAP INTERSECT approach produced robust analgesia to reduce pain affective-motivational behaviors to drops of 55°C water and acetone but had no effect on von Frey mechanical thresholds (**Fig. 4O**). Next on the 50°C inescapable hotplate test, both DREADD groups showed increased latencies to engage in attending and an overall reduction in total time spend attending (**Fig. 4P**). Additionally, both manipulations produced similar dissociation between reflexive sensory detection and the motivational engagement to transition to a recuperative attending strategy (**Fig. 4Q *top***). We interpret this to suggest that chemogenetic disruption of ACC nociceptive-MOR+ cells prevents the cortical integration of valence/sensory/motivational information, thereby deprioritizing the engagement in recuperative nocifensive behaviors relative to other possible action selections. Indeed, once an animal did finally switch its behavior to attending/licking, then the behavioral licking/attending sequences were maintained (**Fig. 4Q *bottom*),** suggesting the ACC is needed for initial behavior-selection, but downstream regions maintain behavior, possibly the BLA, PAG, or dorsal medial striatum. In support, of these novel rodent dissociation observations, similar human observations are reported wherein cingulotomy patients show a pain indifference, reduced recuperative behavior, and reduced recall of pain *(19)*.

Mimicking opioid analgesia to reduce chronic pain via circuit-targeted cingulate interventions.

Tonic or spontaneous pain is a prominent debilitation for chronic pain patients. To evaluate the use of cortical *mMORp*-gene therapies for spontaneous chronic pain, we first used inhibitory optogenetic self-administration via a modified closed-loop place preference design for pain relief-mediated negative reinforcement (**Fig. 5A** and **Fig. S21A-C**). In *pain*TRAP mice, we injected into the bilateral ACC a single *mMORp*-driven vector encoding a Cre-dependent, blue-light-activated iC++ chloride channel to express the opsin in nociceptive-MOR+ neurons; then a bilateral fiber optic cannula was implanted over these neurons (**Fig. 5B**). Mice were split into uninjured or neuropathic pain groups. At 3-week post-SNI, all mice went through a 9-day real-time-to-conditioned place preference protocol. Day-1 consisted of a one-day pre-test for initial chamber bias. Next, seven consecutive days of once-daily self-administration (20-min session) where instrumental movement into the trigger-chamber delivered blue LED light (5-mW, continuous). On the final day, mice had unrestricted access to the previous LED-trigger chamber that serves as a conditioned recall session of prior pain-relief during the optical self-administration. In the uninjured group, there was no change in chamber selection during the active optogenetic sessions nor indication of place preference recall (**Fig. 5C**). However, within and between groups, there was a significant change in selection for the LED-trigger chamber in SNI mice that increased across the conditioning sessions. Furthermore, SNI mice developed robust conditioned recall of optogenetic inhibition of *pain*TRAP MOR+ ACC neurons by actively selecting to spend more time in the previously paired LED chamber (**Fig. 5C**). Together, this indicates that inhibition of the ACC nociceptive-MOR+ ensemble may alleviate spontaneous chronic pain. Importantly, inhibition of this ensemble is not self-reinforcing under the uninjured condition (**Fig. 5C**), suggesting reduced addiction-like liabilities.

For additional evaluation on spontaneous pain, we returned to the *mMORp*-DREADD inhibition strategy and leveraged LUPE to identify changes in behavior use probabilities after the induction of neuropathic pain (**Fig. 5D** and **Fig. S21D, S22, S23, S24**). We elected to use *mMORp*-hM4 over the INTERSECT approach to further demonstrate its translatability, as nociceptive activity-dependent genetics is not currently possible in the clinic. At 3-weeks post-SNI, in control *mMORp*-eYFP injected mice, LUPE detected increased spontaneous licking behavior directed toward the injured hindlimb (**Fig. 5F**), as well as reduced instances of

rearing and general locomotion (**Fig. 5G,H**). In SNI mice expressing *mMORp*-hM4, we found that DCZ significantly reduced spontaneous nocifensive licking and restored some re-engagement in active rearing with no effect on the reduced walking. Furthermore, we found that DREADD inhibition acutely reduced evoked affective-motivational re-

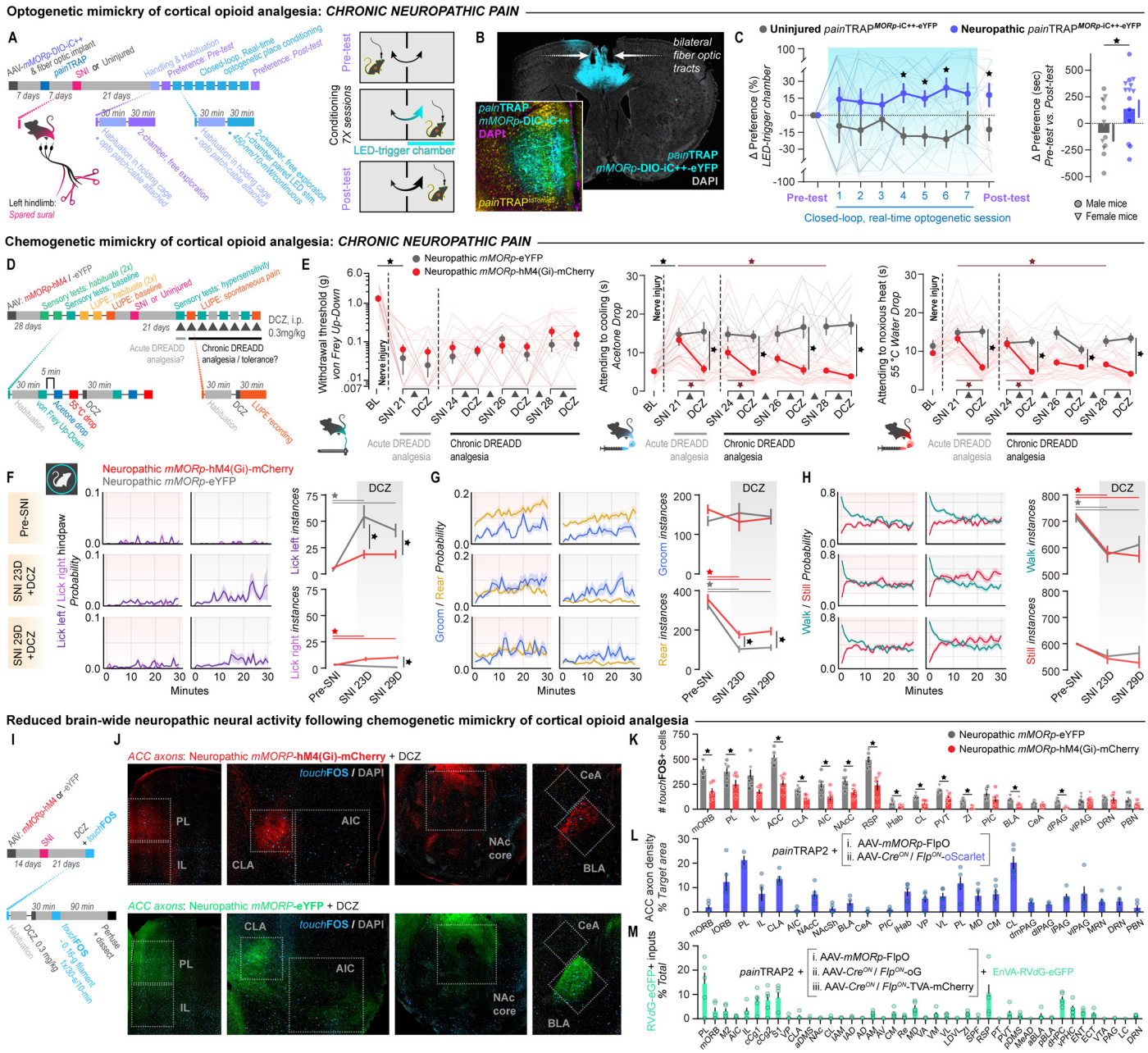

Figure 5. Chronic pain aversion and spontaneous pain can be controlled via an ACC opioidergic gene therapy.

(A) Design for optogenetic inhibition of ACC chronic nociceptive-MOR+ cell-types in a real-time place preference assay. **(B)** *mMORp*-drive iC++ opsin expression and fiber optic placements. **(C)** Cross-day changes in real-time, within-session self-administered inhibition via volitional selection to remain in an LED-triggered chamber, and subsequent conditioned place preference assessment with no LED exposure (N=12 Uninjured mice, N=14 SNI mice). **(D)** Design for chemogenetic inhibition of ACC MOR+ cell-types in neuropathic pain mice (panels D-H: N=20 *mMORp*-eYFP mice, N=30 *mMORp*-hM4; equal sexes). **(E)** Effects of acute and chronic DCZ to engage *mMORp*-hM4 signaling on mechanical hypersensitivity (*left*), cold allodynia (*middle*), and heat hyperalgesia (*right*). **(F)** Effects of mMORp-hM4 inhibition on LUPE-scored neuropathic pain spontaneous behavior repertoires. **(I)** Design to assess brain-wide neuropathic activity with or without *mMORp*-hM4 ACC inhibition. **(J,K)** *mMORp* transgene-expressing ACC axons projecting throughout the brain (J) and light touch-evoked FOS quantification (K) in mice with peripheral nerve injury. **(L)** Axonal projection targets of the nociceptive-MOR+ ACC neural ensemble. **(M)** Brain-wide monosynaptic input neurons to the ACC nociceptive-MOR+ neural ensemble labeled via modified retrograde rabies virus. Two-tailed Student's t test for panel C (right) and K, RM Two-way ANOVA + Bonferonni for panels C (left), E, F, G, H. ★ = P < 0.05. Errors bars = s.e.m.

sponses to acetone and other noxious stimuli without altering hypersensitivity thresholds in SNI mice (**Fig. 5E**), suggesting again that ACC MOR+ neural activities contribute to persistent pain and can be targeted for analgesia *(10)*.

A common problem with opioid drugs is analgesic tolerance, or reduced efficacy at a fixed dose that requires escalation to achieve the same level of pain relief *(50)*. We tested for possible analgesic tolerance to ACC *mMORp*-hM4 DREADD inhibition by administering once-daily DCZ (0.3mg/kg) for 7-days (**Fig. D,E**). However, we were surprised to find that not only did the analgesic effects persist, but that the daily-baseline affective-motivational behaviors to noxious stimuli (when DCZ is cleared) had retuned more than 75% to the pre-SNI sensitivity levels (SNI Day 26/28 timepoints; **Fig. 5E**). This suggests a possible reversal or depotentiation of excitability or circuit plasticity within the large population of MOR+ ACC cell-types that weakens the impact of nociception to prioritize nocifensive behavior selection. Similarly, a recent study also reported an enhanced resolution of inflammation hypersensitivity following when ACC nociceptive cells were inhibited for several days *(34)*.

As noted previously, the ACC *pain*TRAP cells are connected to numerous other brains regions (**Fig. S12**). We find that the nociceptive-MOR+ neurons send long-range axons to the same brain-wide targets *(100)* and receive monosynaptic inputs from other cortical areas (e.g. prelimbic, orbitofrontal, insula, retrosplineal), mediodorsal thalamus, and dorsal/ventral hippocampus (**Fig. 5M**). Given this brain-wide embedded network, we investigated the effect of ACC mMORp-hM4 inhibition to alter chronic pain-related activity throughout the brain by mapping *touch*FOS within ACC nociceptive-MOR+ axonal innervation territories (**Fig. 5I**). Compared to ACC *mMORp*-eYFP control mice with SNI, we found that ACC *mMORp*-hM4 significantly reduced *touch*FOS in multiple cortical, thalamic, subcortical, and midbrain regions (**Fig. 5K**). Thus, this *mMORp* chemogenetic approach can potently modulate brain-wide nociceptive processes to instill robust affective analgesia in chronic pain states.

Discussion.

Like our subjective descriptions of pain, the term "analgesia" encompasses a multi-dimension experience *(1, 19)*. Opioids have been used for millennia for medicinal purposes, specifically to reduce the unpleasantness of pain and make it less bothersome. Today, many prescription analgesics for moderate-to-severe pain are derivatives of opioids: morphine, codeine, oxycodone, hydrocodone, fentanyl, tramadol, methadone, hydromorphone, buprenorphine, tapentadol and more *(4, 101, 102)*. Despite these pain-relieving benefits, the fatal and addictive side effects of these compounds need to be addressed to curtail the Opioid Epidemic *(103, 104)*. While significant reductions in appropriate opioid prescribing have occurred, few safer alternatives to pain management have emerged in recent years, leaving millions of chronic pain patients with limited treatment options. Over the past two decades, clinical trial failures *(5)*, with some recent successes *(105)*, in analgesic drug development were aimed at molecular targets in peripheral sensory afferent neurons or spinal neural circuits with the goal of furthering non-opioid pain management. Clearly, different pain-relieving drugs do not equally interfere with the same underlying mechanisms or parts of the nervous system to alter the perceptual aspects of pain *(106)*. However, while opioids can be administered to the spinal cord for epidural pain-relief, the primary site of analgesic action has been presumed to occur within the brain given the perceived analgesic response effect is not the blockade of pain sensation but a reduction in the perceived unpleasantness of pain. Here, we have identified an ACC ensemble of pain-responsive neurons, across specific populations of superficial and deeper layers, co-expressing the mu-opioid receptor as a mediator of opioid analgesia to reduce pain-related aversion in preclinical rodent models. The cellular identification of this key nociceptive neural ensemble allowed us to leverage a viral vector-based approach to directly mimic the inhibitory effects of morphine on the ACC. Importantly, *MORp*-driven chemogenetics preserves sensory discriminative processes necessary for detecting and localizing noxious stimuli but diminished the unpleasant affective component of pain. Moreover, we did not find evidence of reinforcement in uninjured animals, suggesting reduced addiction liabilities with our ACC opioidergic circuit-targeted therapy *(39)*.

Perceived pain unpleasantness correlates strongly with fMRI activity in the human ACC *(9, 11)*, while patients with intractable chronic pain that were treated with surgical cingulotomy lesions do not report a change in pain perception, intensity discriminations, or reactions to momentary harmful stimuli *(17, 18, 107, 108)*. Rather, their attitude toward pain is modified, dissociating the negative valence from the experience of pain. Here, pain became a sensation and not a threat *(19)*. Cingulotomy results in difficulty sustaining attention and focus, and impairs executive measures of response intention, generation, and persistence *(109, 110)*. The major overall effect of cingulotomy is the attenuation of the patients' continual response, emotionally and behaviorally, to their ever-present pain (i.e., reduced attention switching to and rumination on pain). Like cingulotomy, exogenous opioids separate the sensation of pain from its negative valence and draw of attention *(23, 53)*. Indeed, reports from patients treated with ACC lesions and opiates suggest the relief from the affective symptoms of chronic pain is therapeutically meaningful. Acute pain engages MORs in the dorsal anterior cingulate and lateral prefrontal cortex, and the affective perception of pain is correlated with MOR availability in the ACC, among other brain regions *(23, 24, 55, 94, 111)*. Together, this supports that MOR signaling within the ACC alters the human perception of pain *(15)*. The similarity between the affective mechanisms of morphine and cingulotomy in humans, mirrors our preclinical results with the genetic tuning of MOR expression in the ACC (knock-out *vs.* re-expression) and

with our *MORp*-driven therapy. Thus, we conclude that opioids, as well as our opioid mimicry therapy, inhibit cortical nociceptive functions to reduce the integration of negative valence information within the ACC, resulting in reduced aversive arousal and attentional processes that bias the selection of nocifensive behaviors.

Proposed theories of ACC function center around value appraisal of sensory information and engagement of appropriate motor actions *(15, 112)*, which play a role in measured performance in cognitive *tasks* of *decision*-making based on sensory-guided information *(113)*. During a painful experience, we can define the "*task*" as the sustained attending or motivational behaviors, and the "*decision*" as the selection to engage in these protective and/or escape behaviors. Indeed, ACC nociception preferences an animal to engage in affective-motivational pain attending and escape behaviors *(66)*. Specifically, in line with ethological theory, the detailed behavioral measurements and dynamic transitions quantified from our LUPE experiments indicate that these volitional nocifensive behaviors are constructed of observable, stereotyped behavioral motifs that construct the larger behavior repertoires, which rely on attention and motivation-based signaling in the ACC during active nociceptive processing *(114)*. Advancing methods for assessing the complexity of pain in preclinical animal models is crucial for identifying treatments that target nociception within cognitive-emotional neural circuits. While reflexive withdrawal measures offer valuable insights into noxious detection thresholds, they inadequately capture the nuanced pain affective-evaluative processes influencing the selection of motivational behaviors. In this context, deep learning and machine-vision emerge as pivotal tools enabling automated and precise detection and quantification of pain-related behavior dynamic *(115–117)*, providing valuable insights into the efficacy of analgesics and circuit manipulations. Behavior classifiers, such as LUPE, will not only accelerate the drug discovery process but also enhances assessment objectivity, reducing the potential for human bias and advancing our understanding of pain mechanisms to identify novel candidates for pain management.

Acknowledgements.

This work was supported by: National Institute of Health (NIH) awards NIGMS DP2GM140923 (G.C.), NIDA R00DA043609 (G.C.), NIDA R01DA054374 (G.C., K.B.), NINDS R01NS130044 (G.C., K.B.), NIDA R01DA056599 (G.C., K.B.), NIDA R21DA055846 (B.C.R.), NIDA F32DA053099 (N.M.M), NIDA F32DA055458 (B.A.K.), NIDA F31DA057795 (L.M.W.), NINDS F31NS125927 (J.A.W.), NIDA T32DA028874 (G.S.), the Whitehall Foundation (G.C.), the Howard Hughes Medical Institute (K.D.). We thank the following for shared reagents and technical assistance: Julie Blendy, Angelina Heyeler, Lauren Marconi, Joseph Stzyuncki, Morgan Kindel, and the Penn University Laboratory Animal Resources (ULAR) veterinarians and husbandry staff. We thank Stanford University "Cracking the Neural Code" Program and Gene Vector and Virus Core for custom viruses.

Competing interests.

G.C, K.D., C.R. and G.J.S. are inventors on a provisional patent application through the University of Pennsylvania and Stanford University regarding the custom sequences used to develop, and the applications of *mMORp* and *hMORp* constructs (patent application number: 63/383,462 462 'Human and Murine *Oprm1* Promotes and Uses Thereof').

Data and materials availability.

All mu-opioid receptor promoter viruses (AAV-*mMORp*) will be available for academic use from the Stanford Gene Vector and Virus Core (https://neuroscience.stanford.edu/research/neuroscience-community-labs/gene-vector-and-virus-core) and/or by contacting the lead authors. *Upon manuscript peer-review publication, all data will be unembargoed at Zenodo and GEO.*

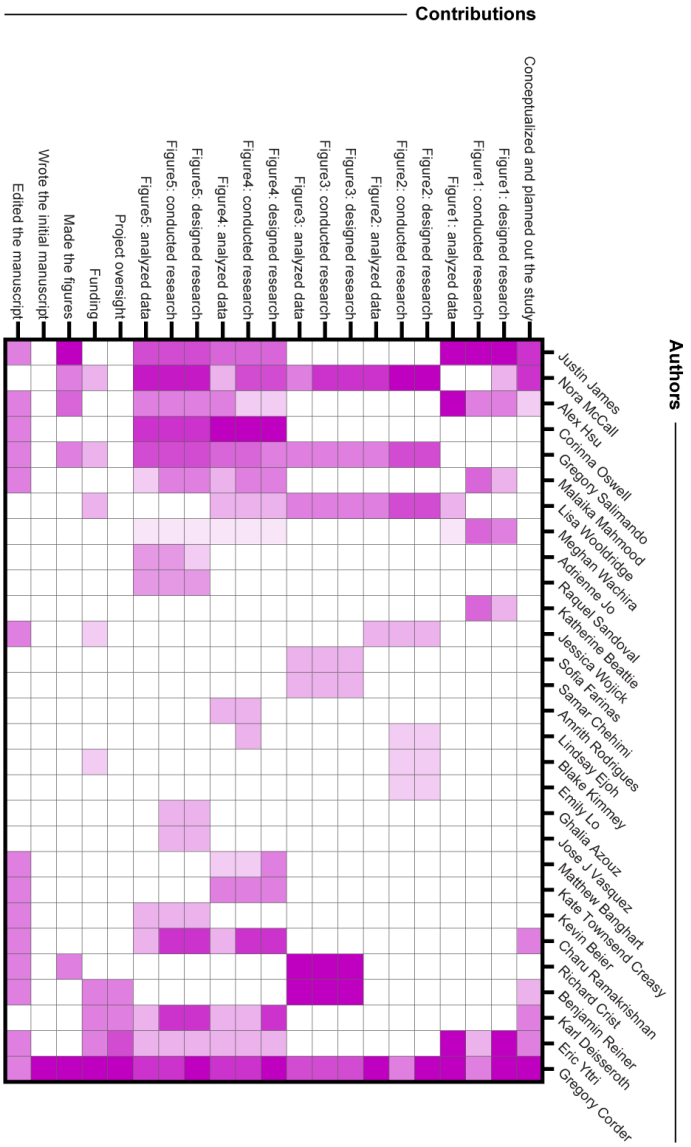

References.

1. B. A. Kimmey, N. M. McCall, L. M. Wooldridge, T. D. Satterthwaite, G. Corder, Engaging endogenous opioid circuits in pain affective processes. *J Neurosci Res* , 1–33 (2020).

2. K. Wiech, Deconstructing the sensation of pain: The influence of cognitive processes on pain perception. *Science (1979)* **354**, 584–587 (2016).

3. L. L. Tan, R. Kuner, Neocortical circuits in pain and pain reliefNat Rev Neurosci **22**, 458–471 (2021).

4. G. Corder, D. C. Castro, M. R. Bruchas, G. Scherrer, Endogenous and Exogenous Opioids in Pain. *Annu Rev Neurosci* , 453–73 (2018).

5. C. J. Woolf, Capturing Novel Non-opioid Pain Targets. *Biol Psychiatry* **87**, 74–81 (2020).

6. T. Grosser, C. J. Woolf, G. A. FitzGerald, Time for nonaddictive relief of pain. *Science (1979)* **355**, 1026–1027 (2017).

7. B. Seymour, Pain : A Precision Signal for Reinforcement Learning and Control. *Neuron* **101**, 1029–1041 (2019).

8. M. Economides, M. Guitart-Masip, Z. Kurth-Nelson, R. J. Dolan, Anterior Cingulate Cortex Instigates Adaptive Switches in Choice by Integrating Immediate and Delayed Components of Value in Ventromedial Prefrontal Cortex. *Journal of Neuroscience* **34**, 3340–3349 (2014).

9. D. D. Price, Psychological and Neural Mechanisms of the Affective Dimension of Pain. *Science (1979)* **288**, 1769–1772 (2000).

10. T. V. P. Bliss, G. L. Collingridge, B. K. Kaang, M. Zhuo, Synaptic plasticity in the anterior cingulate cortex in acute and chronic painNat Rev Neurosci **17**, 485–496 (2016).

11. P. Rainville, Pain Affect Encoded in Human Anterior Cingulate But Not Somatosensory Cortex. *Science (1979)* **277**, 968–971 (1997).

12. A. V. Apkarian, M. C. Bushnell, R. D. Treede, J. K. Zubieta, Human brain mechanisms of pain perception and regulation in health and disease. *European Journal of Pain* **9**, 463–484 (2005).

13. F. Cauda, D. M. E. Torta, K. Sacco, E. Geda, F. D'Agata, T. Costa, S. Duca, G. Geminiani, M. Amanzio, Shared "core" areas between the pain and other task-related networks. *PLoS One* **7** (2012), doi:10.1371/journal.pone.0041929.

14. F. Barthas, J. Sellmeijer, S. Hugel, E. Waltisperger, M. Barrot, I. Yalcin, The anterior cingulate cortex is a critical hub for pain-induced depression. *Biol Psychiatry* **77**, 236–245 (2015).

15. A. J. Shackman, T. V Salomons, H. a Slagter, A. S. Fox, J. J. Winter, R. J. Davidson, The integration of negative affect, pain and cognitive control in the cingulate cortex. *Nat Rev Neurosci* **12**, 154–167 (2011).

16. L. E. Simons, I. Elman, D. Borsook, Psychological processing in chronic pain: A neural systems approach. *Neurosci Biobehav Rev* **39**, 61–78 (2014).

17. E. L. Foltz, E. W. Lowell, Pain "Relief" by Cingulotomy. *J Neurosurg* **19**, 89–100 (1961).

18. E. L. Foltz, L. E. White, Pain "Relief" by Frontal Cingulumotomy. *J Neurosurg* **19**, 89–100 (1962).

19. N. Grahek, *Feeling Pain and Being in Pain* (MIT Press, 2007).

20. R. W. Hurt, H. T. Ballantine, Stereotactic anterior cingulate lesions for persistent pain: a report on 68 cases. *Clin Neurosurg* **21**, 334–351 (1974).

21. J. P. Johansen, H. L. Fields, B. H. Manning, The affective component of pain in rodents: Direct evidence for a contribution of the anterior cingulate cortex. *Proc Natl Acad Sci U S A* **98**, 8077–8082 (2001).

22. S. C. LaGraize, C. J. Labuda, M. A. Rutledge, R. L. Jackson, P. N. Fuchs, Differential effect of anterior cingulate cortex lesion on mechanical hypersensitivity and escape/avoidance behavior in an animal model of neuropathic pain. *Exp Neurol* **188**, 139–148 (2004).

23. J. K. Zubieta, Y. R. Smith, J. A. Bueller, Y. Xu, M. R. Kilbourn, D. M. Jewett, C. R. Meyer, R. A. Koeppe, C. S. Stohler, Regional Mu opioid receptor regulation of sensory and affective dimensions of pain. *Science (1979)* **293**, 311–315 (2001).

24. J.-K. Zubieta, T. A. Ketter, J. A. Bueller, Y. Xu, M. R. Kilbourn, E. A. Young, R. A. Koeppe, *Regulation of Human Affective Responses by Anterior Cingulate and Limbic μ-Opioid Neurotransmission*.

25. X. E. Navratilova, J. Y. Xie, D. Meske, C. Qu, K. Morimura, A. Okun, X. N. Arakawa, M. Ossipov, X. H. L. Fields, F. Porreca, Endogenous Opioid Activity in the Anterior Cingulate Cortex Is Required for Relief of Pain. *Journal of Neuroscience* **35**, 7264–7271 (2015).

26. S. C. LaGraize, J. Borzan, Y. B. Peng, P. N. Fuchs, Selective regulation of pain affect following activation of the opioid anterior cingulate cortex system. *Exp Neurol* **197**, 22–30 (2006).

27. T. T. Hu, R. R. Wang, Y. Du, F. Guo, Y. X. Wu, Y. Wang, S. Wang, X. Y. Li, S. H. Zhang, Z. Chen, Activation of the Intrinsic Pain Inhibitory Circuit from the Midcingulate Cg2 to Zona Incerta Alleviates Neuropathic Pain. *J Neurosci* **39**, 9130–9144 (2019).

28. J. Huang, V. M. Gadotti, L. Chen, I. A. Souza, S. Huang, D. Wang, C. Ramakrishnan, K. Deisseroth, Z. Zhang, G. W. Zamponi, A neuronal circuit for activating descending modulation of neuropathic pain. *Nat Neurosci* **22**, 1659–1668 (2019).

29. V. M. Gadotti, Z. Zhang, J. Huang, G. W. Zamponi, Analgesic effects of optogenetic inhibition of basolateral amygdala inputs into the prefrontal cortex in nerve injured female mice. *Mol Brain* **12**, 10–13 (2019).

30. L. Gu, M. L. Uhelski, S. Anand, M. Romero-Ortega, Y. T. Kim, P. N. Fuchs, S. K. Mohanty, Pain inhibition by optogenetic activation of specific anterior cingulate cortical neurons. *PLoS One* **10**, 1–17 (2015).

31. J. Sellmeijer, V. Mathis, S. Hugel, X.-H. Li, Q. Song, Q.-Y. Chen, F. Barthas, P.-E. Lutz, M. Karatas, A. Luthi, P. Veinante, A. Aertsen, M. Barrot, M. Zhuo, I. Yalcin, Hyperactivity of Anterior Cingulate Cortex Areas 24a/24b Drives Chronic Pain-Induced Anxiodepressive-like Consequences. *The Journal of Neuroscience* **38**, 3102–3115 (2018).

32. H. Zhou, E. Martinez, H. H. Lin, R. Yang, J. A. Dale, K. Liu, D. Huang, J. Wang, Inhibition of the prefrontal projection to the nucleus accumbens enhances pain sensitivity and affect. *Front Cell Neurosci* **12**, 1–13 (2018).

33. K. S. Meda, T. Patel, J. M. Braz, R. Malik, M. L. Turner, H. Seifikar, A. I. Basbaum, V. S. Sohal, Microcircuit Mechanisms through which Mediodorsal Thalamic Input to Anterior Cingulate Cortex Exacerbates Pain-Related Aversion. *Neuron* **102**, 944-959.e3 (2019).

34. X. Qi, K. Cui, Y. Zhang, L. Wang, J. Tong, W. Sun, S. Shao, J. Wang, C. Wang, X. Sun, L. Xiao, K. Xi, S. Cui, F. Liu, L. Ma, J. Zheng, M. Yi, Y. Wan, A nociceptive neuronal ensemble in the dorsomedial prefrontal cortex underlies pain chronicity. *Cell Rep* **41** (2022), doi:10.1016/j.celrep.2022.111833.

35. Q. Zhang, T. Manders, A. P. Tong, R. Yang, A. Garg, E. Martinez, H. Zhou, J. Dale, A. Goyal, L. Urien, G. Yang, Z. Chen, J. Wang, Chronic pain induces generalized enhancement of aversion. (2017), doi:10.7554/eLife.25302.001.

36. J. C. Motzkin, I. Kanungo, M. D'Esposito, P. Shirvalkar, Network targets for therapeutic brain stimulation: towards personalized therapy for pain. *Frontiers in Pain Research* **4** (2023), doi:10.3389/fpain.2023.1156108.

37. S. V. Ovsepian, S. G. Waxman, Gene therapy for chronic pain: emerging opportunities in target-rich peripheral nociceptors. *Nat Rev Neurosci* **24**, 252–265 (2023).

38. M. Mata, S. Hao, D. J. Fink, Applications of Gene Therapy to the Treatment of Chronic Pain. , 42–48 (2008).

39. G. J. Salimando, S. Tremblay, B. A. Kimmey, J. Li, S. A. Rogers, J. A. Wojick, N. M. McCall, L. M. Wooldridge, A. Rodrigues, T. Borner, K. L. Gardiner, S. S. Jayakar, I. Singeç, C. J. Woolf, M. R. Hayes, B. C. De Jonghe, F. C. Bennett, M. L. Bennett, J. A. Blendy, M. L. Platt, K. T. Creasy, W. R. Renthal, C. Ramakrishnan, K. Deisseroth, G. Corder, Human OPRM1 and murine Oprm1 promoter driven viral constructs for genetic access to μ-opioidergic cell types. *Nat Commun* **14** (2023), doi:10.1038/s41467-023-41407-2.

40. G. Bove, Mechanical sensory threshold testing using nylon monofilaments: The pain field's "Tin Standard"*Pain* **124**, 13–17 (2006).

41. T. King, F. Porreca, *Preclinical Assessment of Pain: Improving Models in Discovery Research* (; http://www.springer.com/series/7854).

42. C. J. Vierck, P. T. Hansson, R. P. Yezierski, Clinical and preclinical pain assessment: Are we measuring the same thing?*Pain* **135**, 7–10 (2008).

43. T. King, L. Vera-Portocarrero, T. Gutierrez, T. W. Vanderah, G. Dussor, J. Lai, H. L. Fields, F. Porreca, Unmasking the tonic-aversive state in neuropathic pain. *Nat Neurosci* **12**, 1364–1366 (2009).

44. J. P. Johansen, H. L. Fields, Glutamatergic activation of anterior cingulate cortex produces an aversive teaching signal. *Nat Neurosci* **7**, 398–403 (2004).

45. T. Nath, A. Mathis, A. C. Chen, A. Patel, M. Bethge, M. W. Mathis, Using DeepLabCut for 3D markerless pose estimation across species and behaviors. *Nat Protoc* **14**, 2152–2176 (2019).

46. J. F. Tillmann, A. I. Hsu, M. K. Schwarz, E. A. Yttri, A-SOiD, an active-learning platform for expert-guided, data-efficient discovery of behavior. *Nat Methods* (2024), doi:10.1038/s41592-024-02200-1.

47. A. I. Hsu, E. A. Yttri, B-SOiD, an open-source unsupervised algorithm for identification and fast prediction of behaviors. *Nat Commun* **12**, 1–13 (2021).

48. S. Hunskaar, O. B. Fasmer, K. Hole, *Formalin test in mice, a useful technique for evaluating mild analgesics* (1985).

49. M. Caterina, A. Basbaum, D. Julius, Impaired nociception and pain sensation in mice lacking the capsaicin receptor. *Science (1979)* **288**, 306–313 (2000).

50. G. Corder, V. L. Tawfik, D. Wang, E. Sypek, S. Low, J. Dickenson, B. Barres, C. Bohlen, G. Scherrer, Loss of μ-opioid receptor signaling in nociceptors, and not spinal microglia, abrogates morphine tolerance without disrupting analgesic efficacy. *Nat Med* **23**, 164–173 (2017).

51. https://www.pfizermedicalinformation.com/morphine-0/dosage-admin.

52. A. J. S. Nair, A simple practice guide for dose conversion between animals and human. *J Basic Clin Pharm* **2**, 27–31 (2016).

53. R. C. Kupers, H. Konings ', H. Adriaensen, J. M. Gybels, *Clinical Section Morphine differentially affects the sensory and affective pain ratings in neurogenic and idiopathic forms of pain* (1991; http://journals.lww.com/pain).

54. I. Gilron, J. M. Bailey, D. Tu, R. R. Holden, D. F. Weaver, R. L. Houlden, *Morphine, Gabapentin, or Their Combination for Neuropathic Pain* (2005; www.nejm.org).

55. I. Liberzon, J. K. Zubieta, L. M. Fig, K. L. Phan, R. a Koeppe, S. F. Taylor, mu-Opioid receptors and limbic responses to aversive emotional stimuli. *Proc Natl Acad Sci U S A* **99**, 7084–7089 (2002).

56. M. Vankova, G. Koob, Role Central Mu, Delta-1, and Kappa-1 Opioid Receptors in Opioid-induced Muscle Rigidity in the Rat. *Anesthesiology* **85**, 574–583 (1996).

57. D. L. J. BILBEY, H. SALEM, M. H. GROSSMAN, THE ANATOMICAL BASIS OF THE STRAUB PHENOMENON. *Br J Pharmacol Chemother* **15**, 540–543 (1960).

58. V. E. Brings, M. A. Payne, R. W. Gereau, Opioids alter paw placement during walking, confounding assessment of analgesic efficacy in a postsurgical pain model in mice. *Pain Rep* **7**, E1035 (2022).

59. E. J. Cobos, N. Ghasemlou, D. Araldi, D. Segal, K. Duong, C. J. Woolf, Inflammation-induced decrease in voluntary wheel running in mice: A nonreflexive test for evaluating inflammatory pain and analgesia. *Pain* **153**, 876–884 (2012).

60. C. W. Hutto, J. R. And, W. F. Crowder, C. W. Hutto, W. F. Crowder, *Dosage Choices of Rats for Morphine, for Heroin, and Between Morphine and Heroin* (1997).

61. A. Manglik, H. Lin, D. K. Aryal, J. D. Mccorvy, D. Dengler, G. Corder, A. Levit, R. C. Kling, V. Bernat, H. Hübner, X. Huang, M. F. Sassano, P. M. Giguère, S. Löber, D. Duan, G. Scherrer, B. K. Kobilka, P. Gmeiner, B. L. Roth, B. K. Shoichet, Structure-based discovery of opioid analgesics with reduced side effects. *Nature*, 1–6 (2016).

62. G. Corder, B. Ahanonu, B. F. Grewe, D. Wang, M. J. Schnitzer, G. Scherrer, An amygdalar neural ensemble that encodes the unpleasantness of pain. *Science (1979)* **363**, 276–281 (2019).

63. A. Mansour, C. A. Fox, S. Burke, F. Meng, R. C. Thompson, H. Akil, S. J. Watson, Mu, delta, and kappa opioid receptor mRNA expression in the rat CNS: An in situ hybridization study. *Journal of Comparative Neurology* **350**, 412–438 (1994).

64. U. Baumgärtner, H. G. Buchholz, A. Bellosevich, W. Magerl, T. Siessmeier, R. Rolke, S. Höhnemann, M. Piel, F. Rösch, H. J. Wester, G. Henriksen, P. Stoeter, P. Bartenstein, R. D. Treede, M. Schreckenberger, High opiate receptor binding potential in the human lateral pain system. *Neuroimage* **30**, 692–699 (2006).

65. B. Vogt, R. Wiley, E. Jensen, Localization of Mu and delta opioid receptors to anterior cingulate afferents and projection neurons and input/output model of Mu regulation. *Exp Neurol* , 83–92 (1995).

66. G. Corder, B. Ahanonu, B. F. Grewe, D. Wang, M. J. Schnitzer, G. Scherrer, An amygdalar neural ensemble that encodes the unpleasantness of pain. *Science (1979)* **363**, 276–281 (2019).

67. L. L. Tan, P. Pelzer, C. Heinl, W. Tang, V. Gangadharan, H. Flor, R. Sprengel, T. Kuner, R. Kuner, A pathway from midcingulate cortex to posterior insula gates nociceptive hypersensitivity. *Nat Neurosci* **20**, 1591–1601 (2017).

68. N. R. Ntamati, M. A. Acuña, T. Nevian, Pain-induced adaptations in the claustro-cingulate pathway. *Cell Rep* **42** (2023), doi:10.1016/j.celrep.2023.112506.

69. L. Ye, W. E. Allen, K. R. Thompson, Q. Tian, B. Hsueh, C. Ramakrishnan, A. C. Wang, J. H. Jennings, A. Adhikari, C. H. Halpern, I. B. Witten, A. L. Barth, L. Luo, J. A. McNab, K. Deisseroth, Wiring and Molecular Features of Prefrontal Ensembles Representing Distinct Experiences. *Cell* **165**, 1776–1788 (2016).

70. G. D. Iannetti, A. Mouraux, From the neuromatrix to the pain matrix (and back)*Exp Brain Res* **205**, 1–12 (2010).

71. T. D. Wager, L. Y. Atlas, M. A. Lindquist, M. Roy, C.-W. Woo, E. Kross, An fMRI-Based Neurologic Signature of Physical Pain. *New England Journal of Medicine* **368**, 1388–1397 (2013).

72. C. W. Woo, L. Schmidt, A. Krishnan, M. Jepma, M. Roy, M. A. Lindquist, L. Y. Atlas, T. D. Wager, Quantifying cerebral contributions to pain beyond nociception. *Nat Commun* **8** (2017), doi:10.1038/ncomms14211.

73. S. D. Shields, W. A. Eckert, A. I. Basbaum, Spared Nerve Injury Model of Neuropathic Pain in the Mouse: A Behavioral and Anatomic Analysis. *Journal of Pain* **4**, 465–470 (2003).

74. N. B. Finnerup, R. Kuner, T. S. Jensen, Neuropathic pain: Frommechanisms to treatment. *Physiol Rev* **101**, 259–301 (2021).

75. N. Renier, E. L. Adams, C. Kirst, Z. Wu, R. Azevedo, J. Kohl, A. E. Autry, L. Kadiri, K. Umadevi Venkataraju, Y. Zhou, V. X. Wang, C. Y. Tang, O. Olsen, C. Dulac, P. Osten, M. Tessier-Lavigne, Mapping of Brain Activity by Automated Volume Analysis of Immediate Early Genes. *Cell* **165**, 1789–1802 (2016).

76. S. Hrvatin, D. R. Hochbaum, M. A. Nagy, M. Cicconet, K. Robertson, L. Cheadle, R. Zilionis, A. Ratner, R. Borges-Monroy, A. M. Klein, B. L. Sabatini, M. E. Greenberg, Single-cell analysis of experience-dependent transcriptomic states in the mouse visual cortex. *Nat Neurosci* **21**, 120–129 (2018).

77. S. Shiers, G. Pradhan, J. Mwirigi, G. Mejia, A. Ahmad, S. Kroener, T. Price, Neuropathic pain creates an enduring prefrontal cortex dysfunction corrected by the type II diabetic drug metformin but not by gabapentin. *Journal of Neuroscience* **38**, 7337–7350 (2018).

78. A. Mansour, H. Akil, S. Watson, Mu, delta, and kappa opioid receptor mRNA expression in the rat CNS: an in situ hybridization study. *J Comp Neurol* , 412–38 (1994).

79. K. A. Cummings, S. Bayshtok, T. N. Dong, P. J. Kenny, R. L. Clem, Control of fear by discrete prefrontal GABAergic populations encoding valence-specific information. *Neuron* **110**, 3036-3052.e5 (2022).

80. R. H. Cole, K. Moussawi, M. E. Joffe, Opioid modulation of prefrontal cortex cells and circuits*Neuropharmacology* **248** (2024), doi:10.1016/j.neuropharm.2024.109891.

81. C. Condylis, A. Ghanbari, N. Manjrekar, K. Bistrong, S. Yao, Z. Yao, T. N. Nguyen, H. Zeng, B. Tasic, J. L. Chen, Dense functional and molecular readout of a circuit hub in sensory cortex. *Science (1979)* **375** (2022), doi:10.1126/science.abl5981.

82. L. M. McGarry, A. G. Carter, Prefrontal Cortex Drives Distinct Projection Neurons in the Basolateral Amygdala. *Cell Rep* **21**, 1426–1433 (2017).

83. K. Manoocheri, A. G. Carter, Rostral and caudal basolateral amygdala engage distinct circuits in the prelimbic and infralimbic prefrontal cortex. *Elife* **11** (2022), doi:10.7554/ELIFE.82688.

84. L. Gao, S. Liu, L. Gou, Y. Hu, Y. Liu, L. Deng, D. Ma, H. Wang, Q. Yang, Z. Chen, D. Liu, S. Qiu, X. Wang, D. Wang, X. Wang, B. Ren, Q. Liu, T. Chen, X. Shi, H. Yao, C. Xu, C. T. Li, Y. Sun, A. Li, Q. Luo, H. Gong, N. Xu, J. Yan, Single-neuron projectome of mouse prefrontal cortex. *Nat Neurosci* **25**, 515–529 (2022).

85. J. H. Lui, N. D. Nguyen, S. M. Grutzner, S. Darmanis, D. Peixoto, M. J. Wagner, W. E. Allen, J. M. Kebschull, E. B. Richman, J. Ren, W. T. Newsome, S. R. Quake, L. Luo, Differential encoding in prefrontal cortex projection neuron classes across cognitive tasks. *Cell* **184**, 489-506.e26 (2021).

86. J. A. Wojick, A. Paranjapye, J. K. Chiu, M. Mahmood, C. Oswell, B. A. Kimmey, L. M. Wooldridge, N. M. Mccall, A. Han, L. L. Ejoh, S. N. Chehimi, R. C. Crist, B. C. Reiner, E. Korb, G. Corder, A nociceptive amygdala-striatal pathway for chronic pain aversion. *bioRxiv* (2024), doi:10.1101/2024.02.12.579947.

87. F. Koopmans, P. van Nierop, M. Andres-Alonso, A. Byrnes, T. Cijsouw, M. P. Coba, L. N. Cornelisse, R. J. Farrell, H. L. Goldschmidt, D. P. Howrigan, N. K. Hussain, C. Imig, A. P. H. de Jong, H. Jung, M. Kohansalnodehi, B. Kramarz, N. Lipstein, R. C. Lovering, H. MacGillavry, V. Mariano, H. Mi, M. Ninov, D. Osumi-Sutherland, R. Pielot, K. H. Smalla, H. Tang, K. Tashman, R. F. G. Toonen, C. Verpelli, R. Reig-Viader, K. Watanabe, J. van Weering, T. Achsel, G. Ashrafi, N. Asi, T. C. Brown, P. De Camilli, M. Feuermann, R. E. Foulger, P. Gaudet, A. Joglekar, A. Kanellopoulos, R. Malenka, R. A. Nicoll, C. Pulido, J. de Juan-Sanz, M. Sheng, T. C. Südhof, H. U. Tilgner, C. Bagni, À. Bayés, T. Biederer, N. Brose, J. J. E. Chua, D. C. Dieterich, E. D. Gundelfinger, C. Hoogenraad, R. L. Huganir, R. Jahn, P. S. Kaeser, E. Kim, M. R. Kreutz, P. S. McPherson, B. M. Neale, V. O'Connor, D. Posthuma, T. A. Ryan, C. Sala, G. Feng, S.

E. Hyman, P. D. Thomas, A. B. Smit, M. Verhage, SynGO: An Evidence-Based, Expert-Curated Knowledge Base for the Synapse. *Neuron* **103**, 217-234.e4 (2019).

88. S. Alvarado, M. Tajerian, M. Millecamps, M. Suderman, L. S. Stone, M. Szyf, Peripheral Nerve Injury is Accompanied by Chronic Transcriptome-Wide Changes in the Mouse Prefrontal Cortex. *Mol Pain* **9**, 1744-8069-9-21 (2013).

89. X. T. Qiu, C. Guo, L. T. Ma, X. N. Li, Q. Y. Zhang, F. S. Huang, M. M. Zhang, Y. Bai, G. B. Liang, Y. Q. Li, Transcriptomic and proteomic profiling of the anterior cingulate cortex in neuropathic pain model rats. *Front Mol Neurosci* **16** (2023), doi:10.3389/fnmol.2023.1164426.

90. L. Topham, S. Gregoire, H. M. Kang, M. Salmon-Divon, E. Lax, M. Millecamps, M. Szyf, L. S. Stone, The transition from acute to chronic pain: dynamic epigenetic reprogramming of the mouse prefrontal cortex up to 1 year after nerve injury. *Pain* **161**, 2394–2409 (2020).

91. I. Obara, S. P. Goulding, J. H. Hu, M. Klugmann, P. F. Worley, K. K. Szumlinski, Nerve injury-induced changes in Homer/glutamate receptor signaling contribute to the development and maintenance of neuropathic pain. *Pain* **154**, 1932–1945 (2013).

92. W. Renthal, I. Tochitsky, L. Yang, Y. C. Cheng, E. Li, R. Kawaguchi, D. H. Geschwind, C. J. Woolf, Transcriptional Reprogramming of Distinct Peripheral Sensory Neuron Subtypes after Axonal Injury. *Neuron* **108**, 128-144.e9 (2020).

93. N. Üçeyler, H. G. Buchholz, S. Kewenig, S. J. Ament, F. Birklein, M. Schreckenberger, C. Sommer, Cortical Binding Potential of Opioid Receptors in Patients With Fibromyalgia Syndrome and Reduced Systemic Interleukin-4 Levels – A Pilot Study. *Front Neurosci* **14** (2020), doi:10.3389/fnins.2020.00512.

94. R. E. Harris, D. J. Clauw, D. J. Scott, S. A. McLean, R. H. Gracely, J. K. Zubieta, Decreased central μ-opioid receptor availability in fibromyalgia. *Journal of Neuroscience* **27**, 10000–10006 (2007).

95. S. J. Thompson, M. H. Pitcher, L. S. Stone, F. Tarum, G. Niu, X. Chen, D. O. Kiesewetter, P. Schweinhardt, M. Catherine Bushnell, Chronic neuropathic pain reduces opioid receptor availability with associated anhedonia in rat. *Pain* **159**, 1856–1866 (2018).

96. S. Liu, D.-I. Kim, G. Oh, G. M. Pao, J.-H. Kim, R. D. Palmiter, M. R. Banghart, K.-F. Lee, R. M. Evans, S. Han, Neural basis of opioid-induced respiratory depression and its rescue. , doi:10.1073/pnas.2022134118/-/DCSupplemental.

97. X. Jenny He, J. Patel, C. E. Weiss, X. Ma, B. L. Bloodgood, M. R. Banghart, Convergent, functionally independent signaling by mu and delta opioid receptors in hippocampal parvalbumin interneurons. , doi:10.7554/eLife.

98. Y. Nagai, N. Miyakawa, H. Takuwa, Y. Hori, K. Oyama, B. Ji, M. Takahashi, X. P. Huang, S. T. Slocum, J. F. DiBerto, Y. Xiong, T. Urushihata, T. Hirabayashi, A. Fujimoto, K. Mimura, J. G. English, J. Liu, K. ichi Inoue, K. Kumata, C. Seki, M. Ono, M. Shimojo, M. R. Zhang, Y. Tomita, J. Nakahara, T. Suhara, M. Takada, M. Higuchi, J. Jin, B. L. Roth, T. Minamimoto, Deschloroclozapine, a potent and selective chemogenetic actuator enables rapid neuronal and behavioral modulations in mice and monkeys. *Nat Neurosci* **23**, 1157–1167 (2020).

99. L. Fenno, J. Mattis, C. Ramakrishnan, M. Hyun, Targeting cells with single vectors using multiple-feature Boolean logic. *Nat Methods* **11**, 763–72 (2014).

100. A. Tinnermann, C. Sprenger, C. Büchel, Opioid analgesia alters corticospinal coupling along the descending pain system in healthy participants. *Elife* **11** (2022), doi:10.7554/eLife.74293.

101. M. D. , F. S. S. M. D. , M. P. H. , J. W. M. A. , A. Y. A. B. A. , R. J. D. Ph. , M. P. H. M. A. , K. M. M. D. , K. D. S. M. D. , M. S. , Y. Y. M. S. , and R. F. Ph. D. Roger Chou, *Systematic Review on Opioid Treatments for Chronic Pain: Surveillance Report 3* (2022; https://www.ncbi.nlm.nih.gov/books/NBK556255/table/ch4.tab1).

102. M. Ari, J. T. Alexander, G. Weyer, Prescribing Opioids for Pain*JAMA* **329**, 1789–1790 (2023).

103. N. Volkow, T. McLellan, Opioid Abuse in Chronic Pain — Misconceptions and Mitigation Strategies. *N Engl J Med* **374** (2016), doi:10.1056/NEJMra1507771.

104. N. D. Volkow, F. S. Collins, The Role of Science in Addressing the Opioid Crisis. *NEJM* **377**, 391–394 (2017).

105. J. Jones, D. J. Correll, S. M. Lechner, I. Jazic, X. Miao, D. Shaw, C. Simard, J. D. Osteen, B. Hare, A. Beaton, T. Bertoch, A. Buvanendran, A. S. Habib, L. J. Pizzi, R. A. Pollak, S. G. Weiner, C. Bozic, P. Negulescu, P. F. White, Selective Inhibition of Na V 1.8 with VX-548 for Acute Pain. *New England Journal of Medicine* **389**, 393–405 (2023).

106. A. S. Yekkirala, D. P. Roberson, B. P. Bean, C. J. Woolf, Breaking barriers to novel analgesic drug development*Nat Rev Drug Discov* **16**, 545–564 (2017).

107. N. Agarwal, P. A. Choi, S. S. Shin, D. R. Hansberry, A. Mammis, Anterior cingulotomy for intractable pain. *Interdiscip Neurosurg* **6**, 80–83 (2016).

108. H. T. Ballantine, W. L. Cassidy, N. B. Flanagan, R. Marino, Stereotaxic Anterior Cingulotomy for Neuropsychiatric Illness and Intractable Pain. *J Neurosurg* **26**, 488–495 (1967).

109. H. W. R.A. Cohen, R.F. Kaplan, D.J. Moser, M.A. Jenkins, Impairments of attention after cingulotomy. *Neurology* **53** (1999), doi:https://doi.org/10.1212/WNL.53.4.819.

110. R. A. Cohen, R. Paul, T. M. Zawacki, D. Moser, L. Sweet, H. Wilkinson, Emotion and personality changes following cingulotomy. *Emotion* **1**, 38–50 (2001).

111. I. K. Martikainen, M. Pecina, T. M. Love, E. B. Nuechterlein, C. M. Cummiford, C. R. Green, R. E. Harris, C. S. Stohler, J.-K. Zubieta, Alterations in Endogenous Opioid Functional Measures in Chronic Back Pain. *Journal of Neuroscience* **33**, 14729–14737 (2013).

112. D. M. Yee, J. L. Crawford, T. S. Braver, Dorsal Anterior Cingulate Cortex Encodes the Subjective Motivational Value of Cognitive Task Performance a. *bioRxiv* , 2020.09.20.305482 (2020).

113. M. Sarafyazd, M. Jazayeri, Hierarchical reasoning by neural circuits in the frontal cortex. *Science (1979)* **364** (2019), doi:10.1126/science.aav8911.

114. A. Finkelstein, L. Fontolan, M. N. Economo, N. Li, S. Romani, Attractor dynamics gate cortical information flow during decision-making. *bioRxiv* (2019), doi:http://dx.doi.org/10.1101/2019.12.14.876425.

115. J. M. Jones, W. Foster, C. R. Twomey, J. Burdge, O. M. Ahmed, T. D. Pereira, J. A. Wojick, G. Corder, J. B. Plotkin, I. Abdus-Saboor, A machine-vision approach for automated pain measurement at millisecond timescales. *Elife* **9**, 1–22 (2020).

116. M. Bohic, L. A. Pattison, Z. A. Jhumka, H. Rossi, J. K. Thackray, M. Ricci, N. Mossazghi, W. Foster, S. Ogundare, C. R. Twomey, H. Hilton, J. Arnold, M. A. Tischfield, E. A. Yttri, E. St. John Smith, I. Abdus-Saboor, V. E. Abraira, Mapping the neuroethological signatures of pain, analgesia, and recovery in mice. *Neuron* **111**, 2811-2830.e8 (2023).

117. Z. Zhang, D. P. Roberson, M. Kotoda, B. Boivin, J. P. Bohnslav, R. González-Cano, D. A. Yarmolinsky, B. L. Turnes, N. K. Wimalasena, S. Q. Neufeld, L. B. Barrett, N. L. M. Quintão, V. Fattori, D. G. Taub, A. B. Wiltschko, N. A. Andrews, C. D. Harvey, S. R. Datta, C. J. Woolf, Automated preclinical detection of mechanical pain hypersensitivity and analgesia. *Pain* **163**, 2326–2336 (2022).

118. L. A. DeNardo, C. D. Liu, W. E. Allen, E. L. Adams, D. Friedmann, L. Fu, C. J. Guenthner, M. Tessier-Lavigne, L. Luo, Temporal evolution of cortical ensembles promoting remote memory retrieval. *Nat Neurosci* **22**, 460–469 (2019).

119. G. Corder, B. Ahanonu, B. F. Grewe, D. Wang, M. J. Schnitzer, G. Scherrer, An amygdalar neural ensemble that encodes the unpleasantness of pain. *Science (1979)* **363**, 276–281 (2019).

120. D. C. Castro, C. S. Oswell, E. T. Zhang, C. E. Pedersen, S. C. Piantadosi, M. A. Rossi, A. C. Hunker, A. Guglin, J. A. Morón, L. S. Zweifel, G. D. Stuber, M. R. Bruchas, An endogenous opioid circuit determines state-dependent reward consumption. *Nature* **598**, 646–651 (2021).

121. S. H. Yang, E. Yang, J. Lee, J. Y. Kim, H. Yoo, H. S. Park, J. T. Jung, D. Lee, S. Chun, Y. S. Jo, G. H. Pyeon, J.-Y. Park, H. W. Lee, H. Kim, Neural mechanism of acute stress regulation by trace aminergic signalling in the lateral habenula in male mice. *Nat Commun* **14**, 2435 (2023).

122. D. Seo, E. T. Zhang, S. C. Piantadosi, D. J. Marcus, L. E. Motard, B. K. Kan, A. M. Gomez, T. K. Nguyen, L. Xia, M. R. Bruchas, A locus coeruleus to dentate gyrus noradrenergic circuit modulates aversive contextual processing. *Neuron* **109**, 2116-2130.e6 (2021).

123. E. Cipollari, H. J. Szapary, A. Picataggi, J. T. Billheimer, C. A. Lyssenko, G. S. Ying, L. M. Shaw, M. A. Kling, R. Kaddurah-Daouk, D. J. Rader, D. Praticò, N. N. Lyssenko, Correlates and Predictors of Cerebrospinal Fluid Cholesterol Efflux Capacity from Neural Cells, a Family of Biomarkers for Cholesterol Epidemiology in Alzheimer's Disease. *Journal of Alzheimer's Disease* **74**, 563–578 (2020).

124. A.-H. Pool, H. Poldsam, S. Chen, M. Thomson, Y. Oka, Recovery of missing single-cell RNA-sequencing data with optimized transcriptomic references. *Nat Methods* **20**, 1506–1515 (2023).

125. M. D. Young, S. Behjati, SoupX removes ambient RNA contamination from droplet-based single-cell RNA sequencing data. *Gigascience* **9** (2020), doi:10.1093/gigascience/giaa151.

126. Z. Yao, C. T. J. van Velthoven, T. N. Nguyen, J. Goldy, A. E. Sedeno-Cortes, F. Baftizadeh, D. Bertagnolli, T. Casper, M. Chiang, K. Crichton, S.-L. Ding, O. Fong, E. Garren, A. Glandon, N. W. Gouwens, J. Gray, L. T. Graybuck, M. J. Hawrylycz, D. Hirschstein, M. Kroll, K. Lathia, C. Lee, B. Levi, D. McMillen, S. Mok, T. Pham, Q. Ren, C. Rimorin, N. Shapovalova, J. Sulc, S. M. Sunkin, M. Tieu, A. Torkelson, H. Tung, K. Ward, N. Dee, K. A. Smith, B. Tasic, H. Zeng, A taxonomy of transcriptomic cell types across the isocortex and hippocampal formation. *Cell* **184**, 3222-3241.e26 (2021).

127. S. R. Chaplan, F. W. Bach, J. W. Pogrel, J. M. Chung, T. L. Yaksh, Quantitative assessment of tactile allodynia in the rat paw. *J Neurosci Methods* **53**, 55–63 (1994).

128. S. Hunskaar, O. B. Fasmer, K. Hole, Formalin test in mice, a useful technique for evaluating mild analgesics. *J Neurosci Methods* **14**, 69–76 (1985).

129. G. Corder, B. Ahanonu, B. F. Grewe, D. Wang, M. J. Schnitzer, G. Scherrer, An amygdalar neural ensemble that encodes the unpleasantness of pain. *Science (1979)* **363**, 276–281 (2019).

130. B. L. Roth, Neuron Primer DREADDs for Neuroscientists. , doi:10.1016/j.neuron.2016.01.040.

Supplementary Materials.

Methods.

Animals.
All experimental procedures were approved by the Institutional Animal Care and Use Committee of the University of Pennsylvania and performed in accordance with the US National Institutes of Health (NIH) guidelines. Male and female mice aged 2-5 months were housed 2-5 per cage and maintained on a 12-hour reverse light-dark cycle in a temperature and humidity-controlled environment. All experiments were performed during the dark cycle. Mice had ad-libitum food and water access throughout experiments. For behavioral, anatomical, and transcriptomic experiments, we utilized *Fos*-FOS-2A-iCreER^{T2} or "TRAP2" mice (Fos$^{tm2.1(icre/ERT2)Luo)Luo}$/Jackson Laboratory, stock #030323) *(118)* bred to homozygosity, C57BL/6J wild type mice, Oprm1$^{Cre/Cre}$ mice, and Oprm1$^{fl/fl}$ mice. Additional anatomical experiments utilized TRAP2 mice crossed with *Ai9* (B6.Cg-Gt(ROSA)26Sor$^{tm9(CAG-tdTomato)Hze}$/J) reporter mice that express a tdTomato fluorophore in a Cre-dependent manner ("TRAP2:tdTomato") purchased from Jackson Laboratory, stock #007909 bred to heterozygosity or homozygosity for both genes.

Mouse μ-Opioid Receptor promoter (mMORp).
mMORp is a 1.5 Kb segment selected and amplified from mouse genomic DNA using cgcacgcgtgagaacatatggttggacaaaattc and ggcaccggtggaagggagggagcatgggctgtgag as the 5' and 3' end primers respectively. All *mMORp* plasmids were constructed on an AAV backbone by inserting either the *mMORp* promoter ahead of the gene of interest (i.e., iC++-eYFP) using M1ul and AgeI restriction sites. Every plasmid was sequence verified. Next, all AAVs were produced at the Stanford Neuroscience Gene Vector and Virus Core. Genomic titer was determined by quantitative PCR of the WPRE element. All viruses were tested in cultured neurons for fluorescence expression prior to use *in vivo*.

Viral Vectors.
All viral vectors were either purchased from Addgene.org, or custom designed and packaged by the authors as indicated. All AAVs

were aliquoted and stored at -80°C until use and then stored at 4°C for a maximum of four days. The following AAVs were used:

- AAV1-mMORp-DIO-iC++ (titer: 1.35e12 vg/mL)
- AAV1-mMORp-hM4(Gi)-mCherry (titer: 1.7e12 vg/mL)
- AAV1-mMORp-eYFP (titer: 1.0e12 vg/mL)
- AAV1-mMORp-Flpo (titer: 9.2e11 vg/mL)
- AAV1-mMORp-eYFP (titer: 1.0e12 vg/mL)
- AAV1-mMORp-Flpo (titer: 9.2e11 vg/mL)
- AAV5-nEF-Con/Fon-hM4Di-mCherry (7.4e12 vg/mL)
- AAV1-nEF-Con/Fon-oG (titer: 2.8e12 vg/mL)
- AAV1-nEF-Con/Fon-TVA-mCherry (titer: 2.8e12 vg/mL)
- ΔG-RABV-GFP (titer: 4.3e8 vg/mL; Beier Lab, UCI)
- AAVDJ-Syn-DIO-mCh-2A-MOR (titer: 1.13e12 vg/mL)
- AAV9-hSyn-HI.eGFP-Cre (Addgene 105540-AAV9; titer: 5.44e11 vg/mL)
- AAV9-hSyn-GFP (Addgene 50465-AAV9; titer: 1.9e11 vg/mL)
- AAV5-hSyn-DIO-EGFP (Addgene 50457-AAV5; Titer: 1.3e12 vg/mL)

Stereotaxic surgery.
Adult mice (~8 weeks of age) were anesthetized with isoflurane gas in oxygen (initial dose = 5%, maintenance dose = 1.5%), and fitted into WPI or Kopf stereotaxic frames for all surgical procedures. 10 µL Nanofil Hamilton syringes (WPI) with 33 G beveled needles were used to intracranially infuse AAVs into the ACC. The following coordinates were used, based on the Paxinos mouse brain atlas, to target these regions of interest: ACC (from Bregma, AP: -1.50 mm, ML: ± 0.3 mm, DV:−1.5 mm). Mice were given a 3–8-week recovery period to allow ample time for viral diffusion and transduction to occur. For all surgical procedures in mice, meloxicam (5 mg/kg) was administered subcutaneously at the start of the surgery, and a single 0.25 mL injection of sterile saline was provided upon completion. All mice were monitored and given meloxicam for up to three days following surgical procedures.

Chronic neuropathic pain model.
As described previously *(119)*, to induce a chronic pain state, we used a modified version of the Spared Nerve Injury (SNI) model of neuropathic pain, as previously described (70). This model entails surgical section of two of the sciatic nerve branches (common peroneal and tibial branches) while sparing the third (sural branch). Following SNI, the receptive field of the lateral aspect of the hindpaw skin (innervated by the sural nerve) displays hypersensitivity to tactile and cool stimuli, eliciting pathological reflexive and affective-motivational behaviors (allodynia). To perform this peripheral nerve injury procedure, anesthesia was induced and maintained throughout surgery with isoflurane (4% induction, 1.5% maintenance in oxygen). The left and/or hind leg was shaved and wiped clean with alcohol and betadine. We made a 1-cm incision in the skin of the mid-dorsal thigh, approximately where the sciatic nerve trifurcates. The biceps femoris and semimembranosus muscles were gently separated from one another with blunt scissors, thereby creating a <1-cm opening between the muscle groups to expose the common peroneal, tibial, and sural branches of the sciatic nerve. Next, ~2 mm of both the common peroneal and tibial nerves were transected and removed, without suturing and with care not to distend the sural nerve. The leg muscles are left uncultured and the skin was closed with tissue adhesive (3M Vetbond), followed by a Betadine application. During recovery from surgery, mice were placed under a heat lamp until awake and achieved normal balanced movement. Mice were then returned to their home cage and closely monitored over the following three days for well-being.

TRAP2 protocol.
<u>*Noci*TRAP</u>
*Noci*TRAP induction was performed similarly to previously described *(119)*. We habituated mice to a testing room for two to three consecutive days. During these habituation days, no nociceptive stimuli were delivered and no baseline thresholds were measured (i.e. mice were naïve to pain experience before the TRAP procedure). We placed individual mice within red plastic cylinders (~9-cm D), with a red lid, on a raised perforated, flat metal platform (61-cm x 26-cm). The experimenter's sat in the testing room for the thirty minutes of habituation; this was done to mitigate potential alterations to the animal's stress and endogenous antinociception levels. To execute the TRAP procedure, we placed mice in their habituated cylinder for 30 min, and then a 55°C water droplet was applied to the central-lateral plantar pad of the left hindpaw) once every 30 s over 10 min. Following the water stimulations, the mice remained in the cylinder for an additional 60 min before injection of 4-hydroxytamoxifen (4-OHT, 40 mg/kg in vehicle; subcutaneous). After the injection, the mice remained in the cylinder for an additional 4 hours to match the temporal profile for c-FOS expression, at which time the mice were returned to the home cage.

<u>*Home-cage*TRAP</u>
*Home-cage*TRAP induction was performed without habituation. At least 2 hours into the dark cycle, mice were gently removed from their home cages. Mice were then injected with 4-OHT (40 mg/kg in vehicle; subcutaneous) and returned to their home cages.

<u>*Sex*TRAP</u>
The process of *sex*TRAP began with habituation of mice to "home away from home" (HAFH) cages for one hour a day for four consecutive days beginning at least 2 hours into the dark cycle. During these habituation sessions, animals were isolated in HAFH cage and no stimuli were delivered. On the fifth day, mice were placed alone in HAFH cages for one hour, then were administered 4-OHT (40 mg/kg in vehicle; subcutaneous) before being gently placed back in HAFH cages. Immediately after injection, an age-matched, mating-receptive (estrus or proestrus phase of estrus cycle) conspecific of the opposite sex was introduced to the HAFH cage for four hours to match the temporal profile for 4-OHT. During the social interaction, a video recording was taken to allow for post-hoc manual quantification of mounting behaviors. After that, mice were returned to their home cages.

Immunohistochemistry.
Animals were anesthetized using FatalPlus (Vortech) and transcardially perfused with 0.1 M phosphate buffered saline (PBS), followed by 10% normal buffered formalin solution (NBF, Sigma, HT501128). Brains were quickly removed and post-fixed in 10% NBF for 24 hours at 4 °C, and then cryo-protected in a 30% sucrose solution made in 0.1 M PBS until sinking to the bottom of their storage tube (~48 h). Brains were then frozen in Tissue Tek O.C.T. compound (Thermo Scientific), coronally sectioned on a cryostat (CM3050S, Leica Biosystems) at 30 µm or 50 µm and the sections stored in 0.1 M PBS. Floating sections were permeabilized in a solution of 0.1 M PBS containing 0.3% Triton X-100 (PBS-T) for 30 min at room temperature and then blocked in a solution of 0.3% PBS-T and 5% normal donkey serum (NDS) for 2 hours before being incubated with primary antibodies (1˚Abs included: chicken anti-GFP [1:1000, Abcam, ab13970], guinea pig anti-FOS [1:1000, Synaptic Systems, 226308], rabbit anti-FOS [1:1000, Synaptic System, 226008],rabbit anti-DsRed [1:1000, Takara Bio, 632496]; prepared in a 0.3% PBS-T, 5% NDS solution

for ~16 h at room temperature. Following washing three times for 10 min in PBS-T, secondary antibodies (2°Abs included: Alexa-Fluor 647 donkey anti-rabbit [1:500, Thermo Scientific, A31573], Alexa-Fluor 488 donkey anti-chicken [1:500, Jackson Immuno, 703-545-155], Alexa-Fluor 555 donkey anti-rabbit [1:500, Thermo Scientific, A31572] Alexa-Fluor 647 donkey anti-guinea pig [1:500, Jackson Immuno, 706-605-148], prepared in a 0.3% PBS-T, 5% NDS solution were applied for ~2h at room temperature, after which the sections were washed again three times for 5 mins in PBS-T, then again three times for 10 min in PBS-T, and then counterstained in a solution of 0.1 M PBS containing DAPI (1:10,000, Sigma, D9542). Fully stained sections were mounted onto Superfrost Plus microscope slides (Fisher Scientific) and allowed to dry and adhere to the slides before being mounted with Fluoromount-G Mounting Medium (Invitrogen, 00-4958-02) and cover slipped.

Fluorescence *in situ* hybridization.

Animals were anesthetized using isoflurane gas in oxygen, and the brains were quickly removed and fresh frozen in O.C.T. using Super Friendly Freeze-It Spray (Thermo Fisher Scientific). Brains were stored at −80° C until cut on a cryostat to produce 16 µm coronal sections of the ACC. Sections were adhered to Superfrost Plus microscope slides, and immediately refrozen before being stored at −80° C. Following the manufacturer's protocol for fresh frozen tissue for the V2 RNAscope manual assay (Advanced Cell Diagnostics), slides were fixed for 15 min in ice-cold 10% NBF and then dehydrated in a sequence of ethanol serial dilutions (50%, 70%, and 100%). Slides were briefly air-dried, and then a hydrophobic barrier was drawn around the tissue sections using a Pap Pen (Vector Labs). Slides were then incubated with hydrogen peroxide solution for 10 min, washed in distilled water, and then treated with the Protease IV solution for 30 min at room temperature in a humidified chamber. Following protease treatment, C1 and C2 cDNA probe mixtures specific for mouse tissue were prepared at a dilution of 50:1, respectively, using the following probes from Advanced Cell Diagnostics: *Fos* (C1, 316921), *Drd2* (C2, 406501-C2), and *Drd1* (C3, 406491-C3). Sections were incubated with cDNA probes (2 h), and then underwent a series of signal amplification steps using FL v2 Amp 1 (30 min), FL v2 Amp 2 (30 min) and FL v2 Amp 3 (15 min). 2 min of washing in 1x RNAscope wash buffer was performed between each step, and all incubation steps with probes and amplification reagents were performed using a HybEZ oven (ACD Bio) at 40° C. Sections then underwent fluorophore staining via treatment with a serious of TSA Plus HRP solutions and Opal 520, 570, and 620 fluorescent dyes (1:5000, Akoya Biosystems, FP1487001KT, FP1495001KT). All HRP solutions (C1-C2) were applied for 15 min and Opal dyes for 30 min at 40° C, with an additional HRP blocker solution added between each iteration of this process (15 min at 40° C) and rinsing of sections between all steps with the wash buffer. Lastly, sections were stained for DAPI using the reagent provided by the Fluorescent Multiplex Kit. Following DAPI staining, sections were mounted, and cover slipped using Fluoromount-G mounting medium and left to dry overnight in a dark, cool place. Sections from all mice were collected in pairs, using one section for incubation with the cDNA probes and another for incubation with a probe for bacterial mRNA (dapB, ACD Bio, 310043) to serve as a negative control.

Imaging and Quantification.

All tissue was imaged on a Keyence BZ-X all-in-one fluorescent microscope at 48-bit resolution using the following objectives: PlanApo-λ x4, PlanApo-λ x20 and PlanApo-λ x40. All image processing prior to quantification was performed with the Keyence BZ-X analyzer software (version 1.4.0.1). Quantification of neurons expressing fluorophores was performed via manual counting of TIFF images in Photoshop (Adobe, 2021) using the Counter function or using HALO software (Indica Labs), which is a validated tool for automatic quantification of fluorescently-labeled neurons in brain tissue *(120–122)*. Counts were made using 20X magnified z-stack images of a designated regions of interest (ROI). For axon density quantification, immunohistochemistry was performed to amplify the GFP signal and visualize ipsilateral BLA^{noci} axons throughout the brain in 50 µm tissue free floating slices as described above. Areas with dense axon innervation were identified using 4X imaging. Areas implicated in emotion and nociception were selected for additional 20X imaging with Z-stacks. These regions of interest (ROIs) were initially visualized at 20X to determine the region with the highest fluorescence. The exposures for FITC and CY3 were adjusted to avoid overexposed pixels for the brightest area. This exposure was kept consistent for all slices for an individual mouse. For an individual ROI, one slice per mouse was included. ROIs were drawn in ImageJ and threshold intensity was measured. The maximum intensity was set to a value of 1.0 and all ROIs are reported as intensity compared to the maximum.

We used HALO software for all quantifications. One representative 16 µm slice containing ACC (selected from 1.1-1.3mm anterior of bregma) was quantified per mouse, using HALO Image Analysis software (Indica Labs). The borders for left and right ACC, Cg1, Cg2, L1, L2/3, L5, L6a, and L6b were hand-drawn as individual annotation layers, using the Allen Brain Reference Atlas as a guide. Slices were visually inspected for damage, dust or other debris, and bound probe, and these areas were manually excluded from their respective annotation layers. Colocalization of nuclei (DAPI) with *Oprm1*, *Fos*, and *Vglut* mRNA puncta was automatically quantified using the FISH module (version 3.2.3) and traditional nuclear segmentation. Setting parameters were optimized by comparing performance across 6 slices, randomly selected across experimental groups, and confirming proper detection by visual inspection. Identical parameters were applied across all slices in the data set.

Quantitative PCR.

Cellular RNA was extracted with RNAzol (Sigma-Aldrich, R4533) according to manufacturer's protocol, and cDNA was synthesized from 1 ug RNA (Applied Biosystems, #4374966). cDNA was diluted 1:10 and assessed for mRNA transcript levels by qPCR with SYBR Green Mix (Applied Biosystems, #A25741) on a QuantStudio7 Flex Real-Time PCR System (Thermo Fisher). Oligonucleotide primer sequences for target and reference genes are as follows: mouse_GAPDH (forward: AACGACCCCTTCATTGACCT, reverse: TGGAAGATGGTGATGGGCTT), mouse_L30 (forward: ATGGTGGCCGCAAAGAAGACGAA, reverse: CCTCAAAGCTGGACAGTTGTTGGCA), mouse_*OPRM1* (forward: CTGCAAGAGTTGCATGGACAG, reverse: TCAGATGACATTCACCTGCCAA). The fold change in the target mRNA abundance was normalized by the reference gene GAPDH, was calculated using the $2^{-\Delta\Delta C_T}$ method *(123)*.

Single nuclei RNA sequencing.

<u>Nuclei preparation</u>

A single punch of the right side of the BLA measuring 2 mm in width and 1 mm in depth, was used to prepare the nuclei suspensions. Nuclei isolation was performed utilizing the Minute™ single nucleus isolation kit designed for neuronal tissue/cells (Cat# BN-020, Invent Biotechnologies). Briefly, the tissue was homogenized

using a pestle in a 1.5 mL LoBind Eppendorf tube. Subsequently, the cells were resuspended in 700 µl of cold lysis buffer and RNAse inhibitor and incubated on ice for 5 minutes. The homogenate was then transferred to a filter within a collection tube and incubated at -20ºC for 8 minutes. Following this, the tubes were centrifuged at 13,000 x g for 30 seconds, the filter was discarded, and the samples were centrifuged at 600 x g for 5 minutes. The resulting pellet underwent one wash with 200 µL of PBS + 5% BSA and then resuspended in 60 µL of PBS + 1% BSA. The concentration of nuclei in the final suspension was assessed by staining with Trypan Blue and counted using a hemacytometer. The suspension was diluted to an optimal concentration of 500-1000 nuclei/µL.

Single-Nuclei Gene Expression Assay

Nuclei suspensions were used as input for the 10x Genomics 3' gene expression assay (v3.1), following manufacturer protocols. A total of 20,000 nuclei were loaded into the 10x Genomics microfluidics Chromium controller, with the aim of recovering approximately 10,000-12,000 nuclei per sample. Subsequently, sequencing libraries were constructed, and unique dual indexed libraries were pooled together at equimolar concentrations of 1.75 nM and sequenced on the Illumina NovaSeq 6000, using 28 cycles for Read 1, 10 cycles for the i7 index, 10 cycles for the i5 index, and 90 cycles for Read 2.

Data analysis

Preprocessing of snRNAseq data.

Paired end sequencing reads were processed using 10x Genomics Cellranger v5.0.1. Reads were aligned to the mm10 genome optimized for single cell sequencing through a hybrid intronic read recovery approach *(124)*. In short, reads with valid barcodes were trimmed by TSO sequence, and aligned using STAR v2.7.1 with MAPQ adjustment. Intronic reads were removed and high-confidence mapped reads were filtered for multimapping and UMI correction. Empty GEMs were also removed as part of the pipeline. DESeq2 was used to compare expression at the 3-day, 3-week, and 3-month timepoints to control animals for each cluster. Pseudobulked expression differences were assessed by Wald test and a false discovery rate (FDR) of 0.05 was used to correct for multiple testing.

Clustering and comparison.

Count matrices for each individual sample were converted to Seurat objects using Seurat 4.3, and nuclei were filtered with thresholds of > 200 minimum features and < 5% mitochondrial reads. Initial dimensionality reduction and clustering was performed to enable removal of cell free mRNA using SoupX *(125)*. SCTransform was used to normalize and scale expression data and all samples were combined using the Seurat integration method. Putative doublets identified by DoubletFinder, as well as residual clusters with mixed cell type markers or high mean UMI, were removed. The cleaned dataset was clustered using the first 20 PCs at a resolution of 0.3. Cluster identity was determined by expression of known marker genes.

Modular activity scoring.

Modular activity scores were calculated for all clusters using AddModuleScore with the list of the 25 putative immediate early genes (*Arc*, *Bdnf*, *Cdkn1a*, *Dnajb5*, *Egr1*, *Egr2*, *Egr4*, *Fos*, *Fosb*, *Fosl2*, *Homer1*, *Junb*, *Nefm*, *Npas4*, *Nr4a1*, *Nr4a2*, *Nr4a3*, *Nrn1*, *Ntrk2*, *Rheb*, *Sgsm1*, *Syt4*, *Vgf*) against a control feature score of 5 *(126)*.

Gene ontology analysis.

Gene ontology (GO) analyses were performed for DEGs between uninjured and SNI conditions. GO analysis was performed via PANTHER (protein analysis through evolutionary relationships) v 18.0 on genes that were upregulated in the SNI conditions using the Statistical enrichment test with Bonferroni correction and a p-value cutoff of 0.05. The list of DEGs was assessed for biological processes, molecular function, and cellular components.

Behavioral tests.

All experiments took place during the dark phase of the cycle (0930 hour to 1830 hour). Group and singly housed mice were allowed a 1–2-week acclimation period to housing conditions in the vivarium prior to starting any behavior testing. Additionally, three to five days before the start of testing, mice were handled daily to help reduce experimenter-induced stress. On test days, mice were brought into procedure rooms ~1 hour before the start of any experiment to allow for acclimatization to the environment. Mice were provided food and water *ad libitum* during this period. For multi-day testing conducted in the same procedure rooms, animals were transferred into individual "home away from home" secondary cages ~1 hour prior to the start of testing and were only returned to their home cages at the end of the test day. All testing and acclimatization were conducted under red light conditions (< 10 lux), with exposure to bright light kept to a minimum to not disrupt the animals' reverse light cycle schedule. Equipment used during testing was cleaned with a 70% ethanol solution before starting, and in between, each behavioral trial to mask odors and other scents.

Von Frey filament touch test.

To evaluate mechanical reflexive sensitivity, we used a logarithmically increasing set of 8 von Frey filaments (Stoelting), ranging in gram force from 0.07 to 6.0 grams. Mice were placed on a metal hexagonal-mesh floored platform (24 in x 10 in) within a transparent red cylinder (3.5 in x 6 in). The filaments were then applied perpendicular to the left plantar hind paw with sufficient force to cause a slight bending of the filament. A positive response was characterized as a rapid withdrawal of the paw away from the stimulus within 4 secs. Using the Up-Down statistical method *(127)*, the 50% withdrawal mechanical threshold scores were calculated for each mouse and then averaged across the experimental groups. For the two rounds of inhibitory chemogenetic testing conducted using this assay, mice were administered a dose of either the drug DCZ intrathecally at a dose of 10 pg (first round, 5 weeks post-surgery) or CNO systemically at a dose of 3 mg/kg by body weight (second round, 8 weeks post-surgery, 3 weeks post-DCZ trials), with animals being returned to their home cages for ~30 mins after injecetions.

Hotplate thermal tests (static & dynamic).

To evaluate thermal sensitivity, we used an inescapable hotplate set to ~50-52.5ºC. The computer-controlled hotplate (6.5 in x 6.5 in floor, Bioseb) was surrounded by a 15 in high clear plastic chamber and a web camera was positioned at the front of the chamber to continuously record animals to use for post hoc behavioral analysis. For the static temperature tests conducted for chemogenetic inhibition studies, mice were administered either a 10 pg intrathecal dose of DCZ or a 3 mg/kg systemic dose of CNO (**Fig. 3c**), and then returned to their home cages for ~30 mins to allow for complete absorption of drugs prior to the start of behavioral testing. Mice were then gently placed on the hotplate floor and removed from the chamber after 30 secs. Behaviors were scored in real-time for the latency to the first paw withdrawal, the total duration of paw licking, and the total number of jumps/escape events observed over the entire trial period.

Formalin chemical test.

To evaluate chemical induced nocifensive responses, mice received an intraplantar 10 µL injection of a 4% formalin solution. Mice were lightly restrained in a prone position with the left hind limb held between the thumb and fore finger of the non-dominant hand, while a formalin-loaded glass Hamilton syringe with a 30G needle was held in the dominant hand. The needle was inserted in the middle of the left hind paw at a ~30º angle and the formalin solution was injected over a ~2 sec period. Next, the mice were quickly placed within transparent red cylinder on a stage with a clear plastic floor, with a mirror angled at 45º underneath, while a web camera recorded behavior from both underneath and to the side of the apparatus for 60 mins. These videos were then blind scored in 2-min bins for reflexive paw flinches, paw guarding, paw licking and jumps. Time course data was summed into the classically defined phases of the formalin test*(128)*: 1st phase, interphase and 2nd phase, which reflect different engagements of peripheral and central sensitization mechanisms. For all chemogenetic inhibitory studies, mice were administered a systemic injection of CNO i.p. (3 mg/kg body weight), after which they were returned to their home cage for ~30 mins prior to the start of testing to allow for full absorption of the drug to occur.

Hot water hind paw stimulation test.
To evaluate responses to acute, noxious thermal stimulations during fiber photometry testing, we used a hot water hind paw application protocol described previously *(129)*. In brief, animals were placed in transparent red cylinders placed on top of a metal hexagonal-mesh floored platform, while a small hot plate was used to heat distilled water to ~70-72ºC. Using a 1 mL syringe, a drop of the hot water was quickly applied to the underside of the left plantar hind paw (temp = 55-57ºC at time of application). This process was repeated for a total of 10 applications, with each droplet applied at a 1 min interval. Animals were continuously recorded by a web camera positioned to face the front of the cylinder in which the animal was housed, and all relevant behaviors time-locked to calcium mediated events were scored post-hoc using the video footage. Responses to these noxious stimuli were also tested following acute i.p. administration of morphine (~10 mg/kg body weight). After injection, animals were placed back in their home away from home cages for 30 mins to allow for complete absorption of the drug. Hot water hind paw stimulation testing then proceeded as described above in the naïve condition.

Sensory testing for pain affective-motivational and nociceptive reflex behavioral assays
To evaluate mechanical reflexive sensitivity, we used a logarithmically increasing set of 8 von Frey filaments (Stoelting), ranging in gram force from 0.07- to 6.0-g. These filaments were applied perpendicular to the plantar hindpaw with sufficient force to cause a slight bending of the filament. A positive response was characterized as a rapid withdrawal of the paw away from the stimulus within 4 seconds. Using the Up-Down statistical method, the 50% withdrawal mechanical threshold scores were calculated for each mouse and then averaged across the experimental groups *(119)*.

To evaluate affective-motivational responses evoked by mechanical stimulation, we used a sharp 25G syringe needle (pin prick) *(119)*. The pin prick was applied as a sub-second poke to the hindpaw, and the duration of attending behavior was collected for up to 30 s after the stimulation. To evaluate affective-motivational responses evoked by thermal stimulation *(119)*, we applied either a single, unilateral 55ºC drop of water or acetone (evaporative cooling) to the left hindpaw, and the duration of attending behavior was collected for up to 30 s after the stimulation. Only one drop stimulation was applied on a given testing session. Additionally, we used an inescapable hotplate set to 50º C. The computer-controlled hotplate (6.5 in x 6.5 in floor, Bioseb) was surrounded by a 15 in high clear plastic chamber and two web cameras were positioned at the front or side of the chamber to continuously record animals to use for post hoc behavioral analysis. For the tests conducted for chemogenetic activation studies, mice were administered CNO 30 min prior to the start of behavior testing to allow for complete absorption of the drug and previous sensory testing fd*(130)*. Mice were gently placed in the center of the hotplate floor and removed after 60 seconds.

Closed-loop, Optogenetic Real-Time Place Preference (oRTPP) & Conditioned Place preference (oCPP).
First, *pain*TRAP2 mice injected with AAV1-*mMORp*-DIO-iC++ and bilateral fiber-optic implants (200-µm diameter, 0.66-NA, 700-µm pitch between each fiber center; Thorlabs), with SNI or no-injury, were habituated for 30-min a day for 5-days in a holding cage. For basal place-preference measurements (*Pre-test session*), mice with attached patch cables, were placed in a two-chamber acrylic box (60 × 25 × 30 cm3), with each side of the chamber measuring 30 × 25 cm2), at room temperature (~23 ºC), under ~10 lux red-light. Each chamber had different contextual pattern cues on the wall: one side had a black-and-white-striped pattern and the other a dotted pattern. Mouse movements were recorded in real-time with an overhead top-view Basler camera connected to Ethovision tracking software (Noldus), connected via a mini-I/O box to a 450-nm LED and pulse-wave generator (Prizmatix), for 30-min. Chamber preference times were quantified by Ethovision for the amount of time spent in each chamber. Using a biased-design, based on the quantified basal preference, mice received LED stimulation in the non-preferred chamber, as our hypothesis was that activation of iC++ would reduce spontaneous pain and drive increased dwell-time in the LED-paired chamber. The following day, to assess oRTPP, mice were placed in the center of the apparatus for a 30-min session. During this session, Ethovision body-contour tracking of the mouse center-point activated the blue LED when the center-point was detected in the originally non-preferred chamber, which in turn delivered 10-mW continuous light through the bifurcating fiber optic implants for the entire duration that the mouse center-point was detected in the chamber; the LED would turn off when the mouse center-point was detected in the other chamber (i.e. Closed-loop protocol). This procedure was repeated daily for seven consecutive sessions to oRTPP-induced learning rates over time. After the Pre-test, and seven closed-loop optogenetic sessions, we performed one Post-test session to assess if a conditioned place preference had developed. Here, mice remained connected to the patch cables but no light was delivered, and the time spent in each chamber was calculated. Increased time in the formally LED-paired chamber indicates a learned preference for iC++-mediated inhibition of ACC nociceptive MOR+ cell-types.

Drugs and Delivery.
For chemogenetic studies, deschloroclozapine (DCZ dihydrochloride, water soluble; HelloBio, HB9126) was delivered intrathecally at a dose of 10 pg in 5 µL saline, and clozapine N-oxide (CNO dihydrochloride, water soluble; HelloBio HB6149) was delivered i.p. systemically at a dose of 3.0 mg/kg body weight. For fiber photometry behavioral testing, morphine sulfate (Hikma) was delivered acutely i.p. at a dose of 10 mg/kg body weight, or chronically at concentrations of 0.3 mg/mL and 0.5 mg/mL by mixing into drinking water along with 0.2% saccharin sodium hydrate (Sigma)

in the animals' drinking water. Precipitated withdrawal was inducing during photometry studies by administering naloxone hydrochloride (HelloBio, HB2451; i.p., 3 mg/kg body weight).

Whole-brain clearing, imaging and analysis.
We used ~8-week old male and female TRAP2;Sun1-sfGFP double transgenic mice (homozygous for both alleles) for whole-brain mapping of nociceptive tagged cells and c-FOS immunolabeling. Brain samples from all groups were collected and processed on the same day to limit possible batch effects. First, all mice underwent the acute *pain*TRAP protocol to permanently label nociceptive cells with Sun1-sfGFP (a nuclear-envelop protein fused with green fluorescent protein, which was selected to improve automated cell counting by avoiding fluorophores filling cellular processes and obscuring cell somas. Then, 3-days later, mice in the neuropathic-pain groups underwent the SNI nerve injury procedure for transection of the tibial and common peroneal branches of the left hindlimb's sciatic nerve, while the no-injury groups remained uninjured. Next, 20-days later all mice, in all conditions/groups, were handled and habituated to a testing apparatus for one session. Then at 21-days post-SNI, the nerve-injured mice were returned to the testing apparatus and underwent either 1) *touch*FOS: a light-touch mechanical stimulation protocol to elicit expression of the immediate early gene cFOS consisting of a 1-sec static touch to the lateral edge of the hypersensitivity left hindpaw [the spared-sural innervation area]), once every 30-sec for 10-min; or 2) *home-cage*FOS: no stimulation. The no-injury group mice were underwent either 1) *pain*FOS: drops of noxious 55°C water (~50-µl) to the left hindpaw, once every 30-sec for 10-min; or 2) *home-cage*FOS: no stimulation. After 90-min from the end of the stimulation protocols, all mice were perfused with 10% formalin and the brains were harvested and fixed overnight in 10% formalin for 24-hr before being transferred to 1X PBS + 0.4 azide. Whole-brain clearing, imaging and automated analysis were performed by LifeCanvas Technologies through a contracted service. In brief, fixed whole brains were prepared with SHIELD (stabilization under harsh conditions via intramolecular epoxide linkages to prevent degradation) to preserve protein antigenicity before being actively cleared and immunolabelled with propidium iodide (cell registration), a GFP antibody and a c-FOS antibody using SmartBatch+. Labelled brains were indexed by EasyIndex and imaged by volumetric lightsheet microscopy (SmartSPIM), followed by image post-processing, cell quantification, atlas registration (Allen Institute CCF_v3) and regional graphics. The number and density of FOS+, GFP+, and the co-expression of FOS + GFP+ cells were calculated for each subregion of the Allen Brain Atlas and visualized as the raw counts or the log2 fold change in each brain subregion, relative to the control condition shown in Figure 4 and associated Supplemental Figures.

LUPE – Light aUtoamted Pain Evaluator.
Design

- Video Acquisition
  - Frame Size / Resolution
    - Frame width = 768 pixels
    - Frame height = 770 pixels
  - Basler Camera Settings
    - Analog Control
      - Gain [db] = 10.0
      - Gamma = 2.0
    - Acquisition Control
      - Exposure Time = Standard
      - Exposure Mode = Timed
      - Exposure Time = 1550.0
      - Trigger Selector = Frame Start
    - Recording Settings
      - Set Fixed Playback Speed = 60.0 fps
      - Quality = Max
      - Recording Buffer Size = 128 frames
      - Records a frame every 16 ms

Pose Estimation via DeepLabCut
Assigning 2D markerless pose estimation of mice within LUPE was achieved through the DeepLabCut (DLC) program (version 2.3.5-8). DLC was favored for this purpose because of its capability to track body-points at high confidence when animals perform diverse behaviors as well as its ability to accurately report if a body part is visible in a given frame. Its extensive toolkit, documentation, and forums allow flexible user input and manipulation when creating models.

Body-points considered for assigning pose in the LUPE-DLC Model were based on the clarity and frequency of appearance, involvement in behavior sequences, and prospective analyses performed. As such, 20 body-points were included in the LUPE pose estimation network built in DLC: snout, upper mouth, middle forepaw digit and palm of left and right forepaws, all digits and palm of left and right hindpaws, genital region, and tail base.

Model was trained iteratively 17 times for up to 350,000 iterations per training when loss and learning rate plateaued. Network architecture and augmentation method chosen was resnet_50 and imgaug, respectively. Percent of dataset trained on was 95% with the remaining 5% remaining used as test dataset for evaluation. For the final training iteration, the mean average Euclidean error between the manual labels and the ones predicted by model was 2.2 pixels (0.073 cm) for training dataset error and 2.33 pixels (0.077 cm) for test dataset error.

Frames for labeling were extracted manually focused on specific behavior sequences and individual frames not accurately or confidently labeled by the model. After each training, frames for data input were added as needed for accuracy and confidence to label videos trained on and novel videos analyzed through LUPE not trained in the model. The total number of frames labeled was 14554, with 10,825 (74.38%) and 3,729 (25.62%) frames coming from male and female video data files, respectively. There were 169 total number of unique, mouse video files that frames were extracted from (133, 78.69% male; 36, 21.31% female). The behavioral assays chosen for recording and model input capture different experimental paradigms and chemically evoked manipulations. From this, the model is able to assign pose data points with high accuracy and confidence for both male and female mouse video data from a variety of behavioral data.

The male video data included: subcutaneous saline injection response (210, 1.94%), subcutaneous morphine 10 mg/kg response (1105, 10.21%), left hindpaw intraplantar capsaicin response (666, 6.15%), left hindpaw intraplantar 1% formalin (960, 8.87%), left hindpaw intraplantar 5% formalin (1271, 11.74%), habituation to LUPE chamber (720, 6.65%), formalin left hindpaw intraplantar injection (829, 7.66%), formalin right hindpaw intraplantar injection (719, 6.64%), formalin cheek injection (472, 4.36%), SNI left hindpaw injury day-0 (170, 1.57%), SNI left hindpaw injury day-3 (508, 4.69%), SNI left hindpaw injury day-7 (380, 3.51%), SNI left hindpaw injury day-21 (255, 2.36%), SNI right hindpaw injury day-0 (652, 6.02%), SNI right hindpaw injury day-

3 (508, 4.69%), SNI right hindpaw injury day-7 (510, 4.71%), SNI right hindpaw injury day-21 (254, 2.35%), and naloxone precipitated morphine withdrawal (636, 5.88%).

The female video data included: subcutaneous morphine 10 mg/kg response (133, 3.57%), habituation to LUPE chamber (320, 8.59%), formalin left hindpaw intraplantar injection (148, 3.97), formalin right hindpaw intraplantar injection (150, 4.02%), SNI left hindpaw injury day-0 (1050, 28.17%), SNI left hindpaw injury day-3 (450, 12.07 %), SNI left hindpaw injury day-7 (350, 9.39%), SNI right hindpaw injury day-0 (826, 22.16%), SNI right hindpaw injury day-3 (150, 4.02%), and SNI right hindpaw injury day-7 (150, 4.02%).

Behavior Classification via A-SOiD/B-SOiD

We trained a Random Forest Classifier to predict 5 different behaviors (still, walking, rearing, grooming, licking hindpaw) given the pose estimation of the previously described 20 body parts. This supervised classifier is refined using an active learning approach over 27 iterations, with a total of 51,377 frames (still: 11,599, walking: 12,809, rearing: 7,270, grooming: 12,719, and licking hindpaw: 6,971). Upon reaching an average f1 score amongst the 5 classes was 93.5%, we predicted all existing pose files and segmented licking hindpaw into licking left hindpaw and licking right hindpaw as they were clearly dissociable. After splitting the laterality of licking hindpaw, we retrained the Random Forest Classifier to expand its classification from 5 classes to 6 classes. The final average f1 score amongst 6 classes was 94.3%.

LUPE Analyses

Once the model is trained, we predicted all the behavioral data in this paper with the same Random Forest Classifier model. Due to the nature of intermittent pose estimation noise, we decided to smooth the output behavior to only consider continuous bouts that are >= 200ms.

To analyze behavior ratio over time (seen in Figure 1 and Figure 5), we calculated the counts for each behavior for each minute then normalized by the total number of frames. This quantification allows us to track when a particular behavior occurs during each session. To explore the variability across animals, we plotted the mean +- standard error of the mean.
To analyze the distance traveled, one body-point that is high in confidence for pose detection and is always present in behavioral sequences was chosen, being the tail base, to calculate the Euclidean distance between consecutive frames of the tail base position. This was calculated by subtracting the x- and y-coordinates of the tail base between consecutive frames and then calculating the Euclidean norm of the resulting vector. Distance calculated in pixels was then converted to a specified, being centimeters, using a conversion factor of 0.0330828 cm/pixels. This conversion factor is unique to the aspect ratio of our frames and resolution of the video data. To explore the variability across animals, we plotted the mean +- standard error of the mean.

Heatmaps of the distance traveled were generated by constructing a 2D histogram of the tail base x- and y-coordinates. The code functions by binning the pose data points into a specified number of bins (being 50 in this case) along each x- and y-coordinate ranges. The 'counts' collected represent the frequency of occurrences in the 2D histogram that fall in each bin representing a range of x- and y-coordinates.

Supplemental Figures.

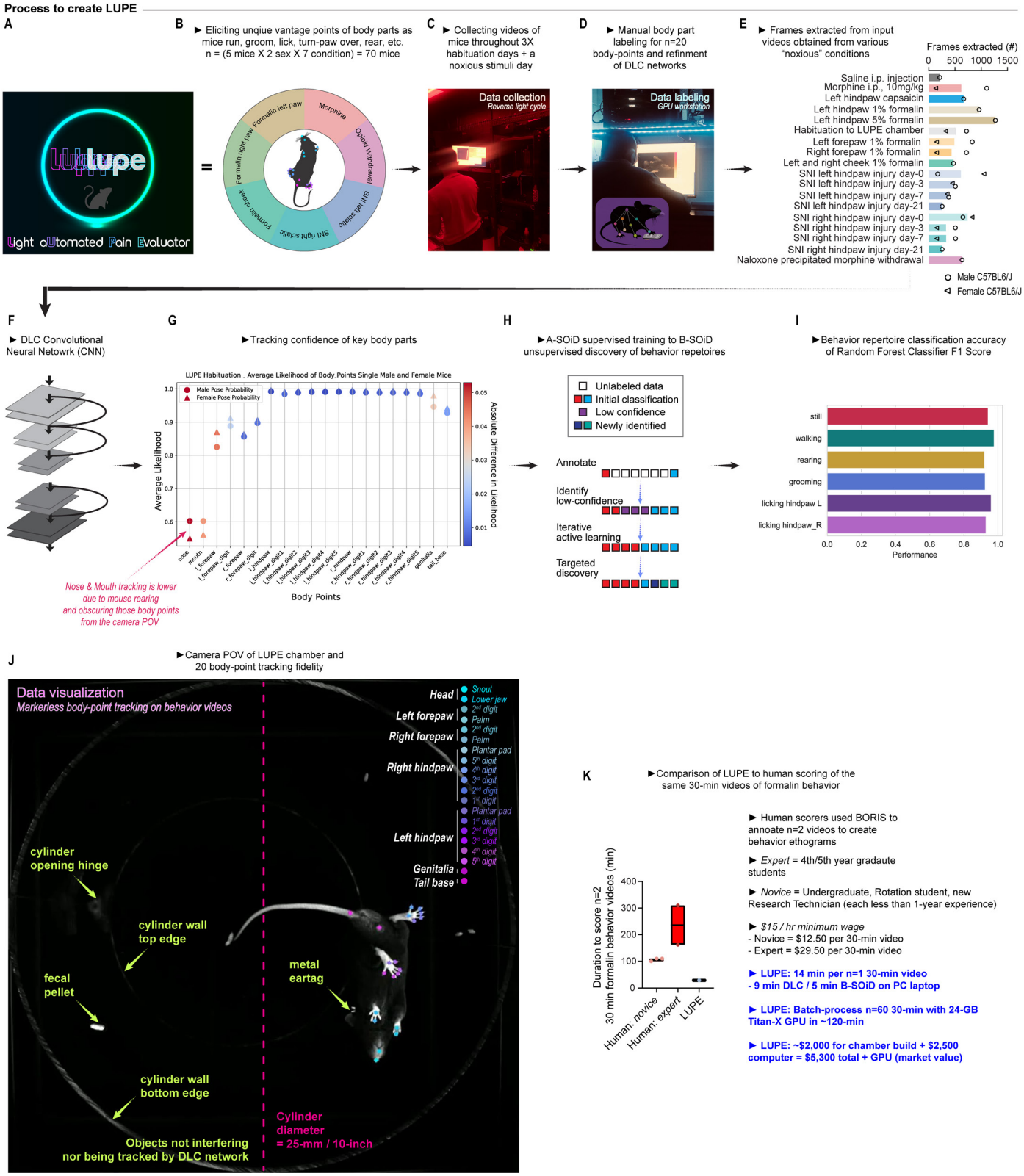

Fig. S1. Process to create the LUPE analysis package. (A) LUPE (**L**ight a**U**tomated **P**ain **E**valuator), a novel method for studying pain in mice in a controlled environment that allows for streamlined ethological behavior classification using open-source, machine learning algorithms for pose estimation and behavior classification. **(B)** Model training data includes video data from different pain and analgesia behavioral assays, capturing a range of behavior sequences with diverse pose dynamics. **(C)** Experimental assays were collected under reverse light cycles. Video data was collected for the first three days when mice habituated to behavior room and LUPE chamber and on the fourth day when pain or analgesia assay was performed. **(D)** Input data for the LUPE-DLC network included manually extracted frames that were labeled with 20 body-points for each training iteration using a graphics processing unit (GPU). **(E)** Sum of

frames labeled per experimental conditions per sex were manually selected based on sequences of behaviors where pose was not labeled confidently or correctly by the model. **(F)** This procedure of training evaluation, manual frame extraction and labeling, and re-training was iterative, taking advantage of DLC's convolutional neural network algorithm until pose-estimation performance was qualitatively and **(G)** quantitatively confident and accurate. The quantitative evaluation of the LUPE-DLC model was based on the computed mean average Euclidean error (MAE) between the manual labels and the ones predicted by DLC after each training iteration. The labeled test (DLC produced, unseen images) and training images were evaluated qualitatively to confirm model predictions aligned with required accuracy for pose assignment. **(H)** After developing the LUPE-DLC network, A-SOiD's active-learning algorithm translated the 2-dimensional pose of the 20 body-points into meaningful behavioral classification. **(I)** The A-SOiD active-learning training procedure was iterated 27 times until the model successfully classified six behavior motifs of interest at high degree of confidence assessed by the random forest classifier F1 score. **(J)** Example image of the bottom-up camera perspective of the LUPE chamber details the maintained pose-estimation of the 20 body-points of interest while ignoring noise of the background in the image. **(K)** To compare the savings of time and money by utilizing LUPE networks, time to complete behavior classification for two 30-minute behavior assays was compared between LUPE and novice (n=2) and expert (n=2) human scorers. LUPE outcompeted human-scorers by requiring approximately 14 minutes to complete behavior classification of one 30-minute behavior recording.

LUPE chamber: Off-the-shelf components to build a highly reproducible apparatus for standardized behavior conditions, at low-cost

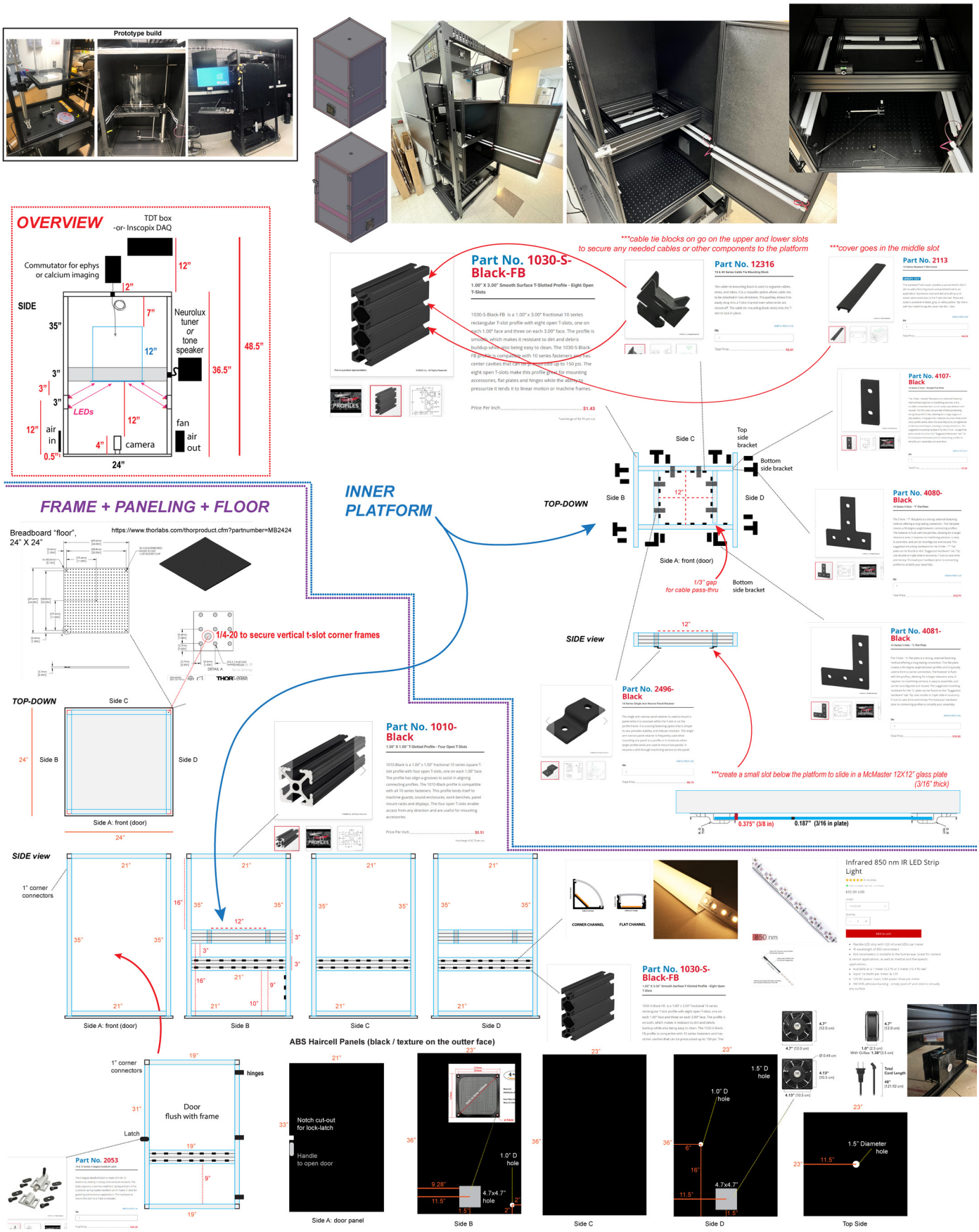

Fig. S2. Process to create the LUPE chamber. The standardized chamber consists of commercially available components, such as plastic sheeting, 80/20 t-slot frames and brackets, and infra-red 850-nm LED strips. The exact build speci-

fications, specifically the distance from the camera lens to the glass floor plate and location of the LEDs, provide a consistent video recording environment that can be easily replicated with and across labs. All dimensions and part numbers are listed in the figure layout. The approximate total time to build the LUPE chamber is 2.5 hours.

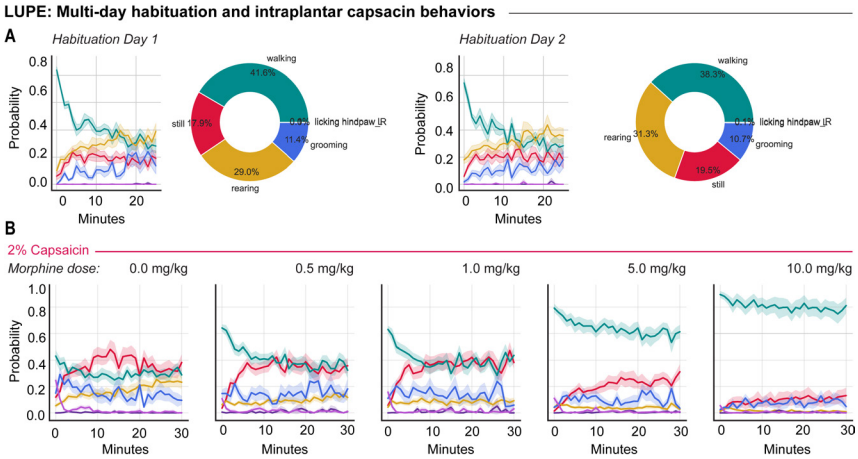

Fig. S3. **(A)** Temporal probability plots for each of the six primary behavior repertoires in 1-min bins in uninjured mice and percentage of total time per repertoire for two consecutive habituation days. **(B)** Effects of escalating morphine doses on each behavior repertoire in 2% capsaicin injured mice.

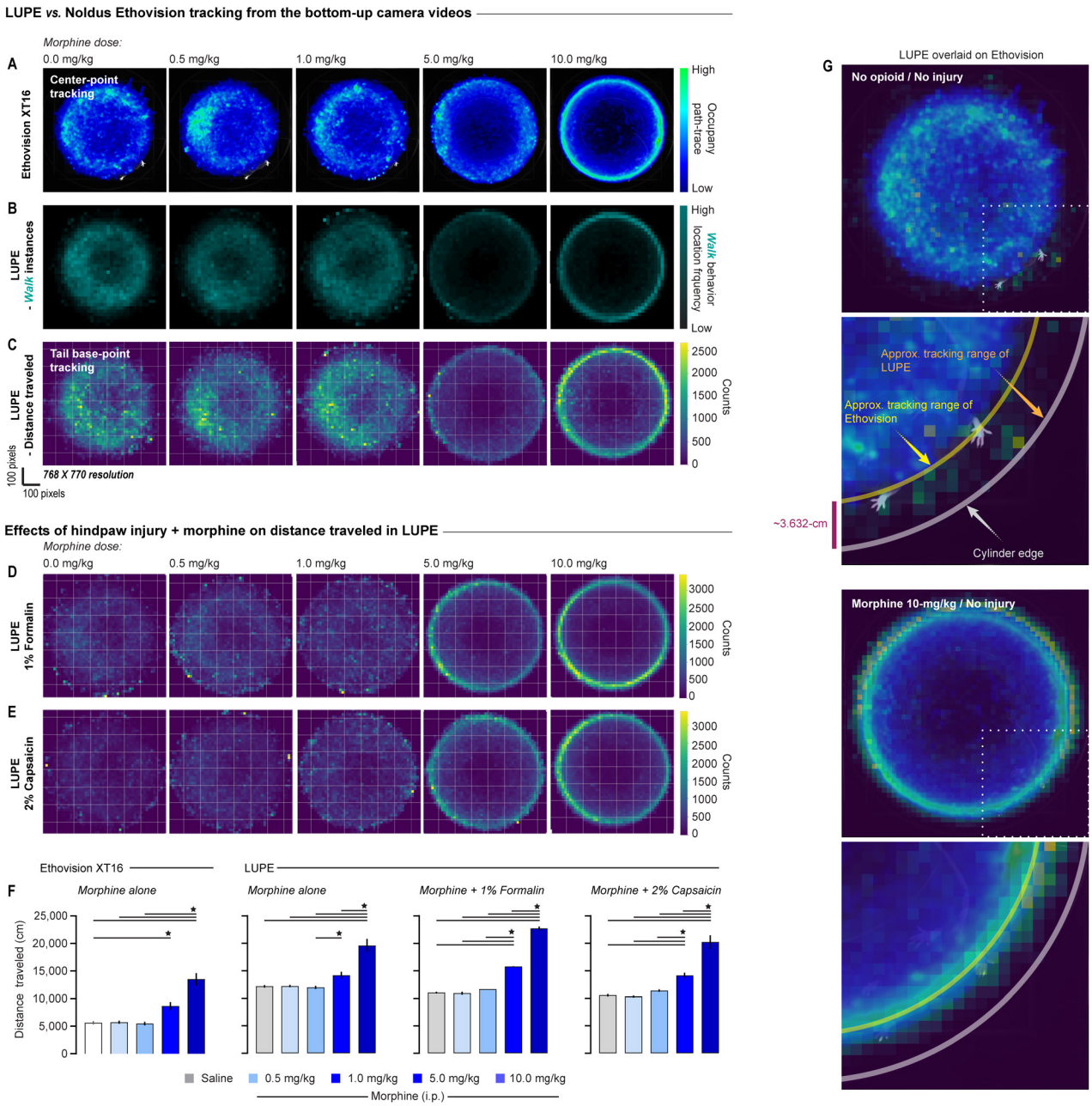

Fig. S4. LUPE vs. Noldus Ethovision tracking from the bottom-up camera videos. Movement of mice in LUPE chamber across varying dosages of morphine (n=20/group) illustrated as heatmaps were compared between **(A)** center-point tracking through Ethovision tracking software (Noldus), and LUPE's pose-behavioral analysis for **(B)** frequency of where the walking behavior occurred and **(C)** tail base-point tracking. Distance traveled by mice after **(D)** 1% formalin (n=10/group) and **(E)** 2% capsaicin (n=20/group) intraplantar injection increased with higher dosages of morphine, with 5.0- and 10.0- mg/kg heatmaps illustrating the hyperlocomotive side effects. **(F)** Computational analysis of the distance traveled was converted from pixel values to centimeters and compared between Ethovision and LUPE. LUPE reports further distance traveled than Ethovision; however, the difference is proportional to the commercialized product. One-way ANOVA + Tukey for panels. ★ = P < 0.05. Errors bars = s.e.m. **(G)** Overlaying the heatmap images produced of the control (top) versus 10-mg/kg morphine response (bottom) demonstrates that Ethovision's automated, center-point tracking underestimates the distance traveled by tracking a smaller circumference of the LUPE chamber.

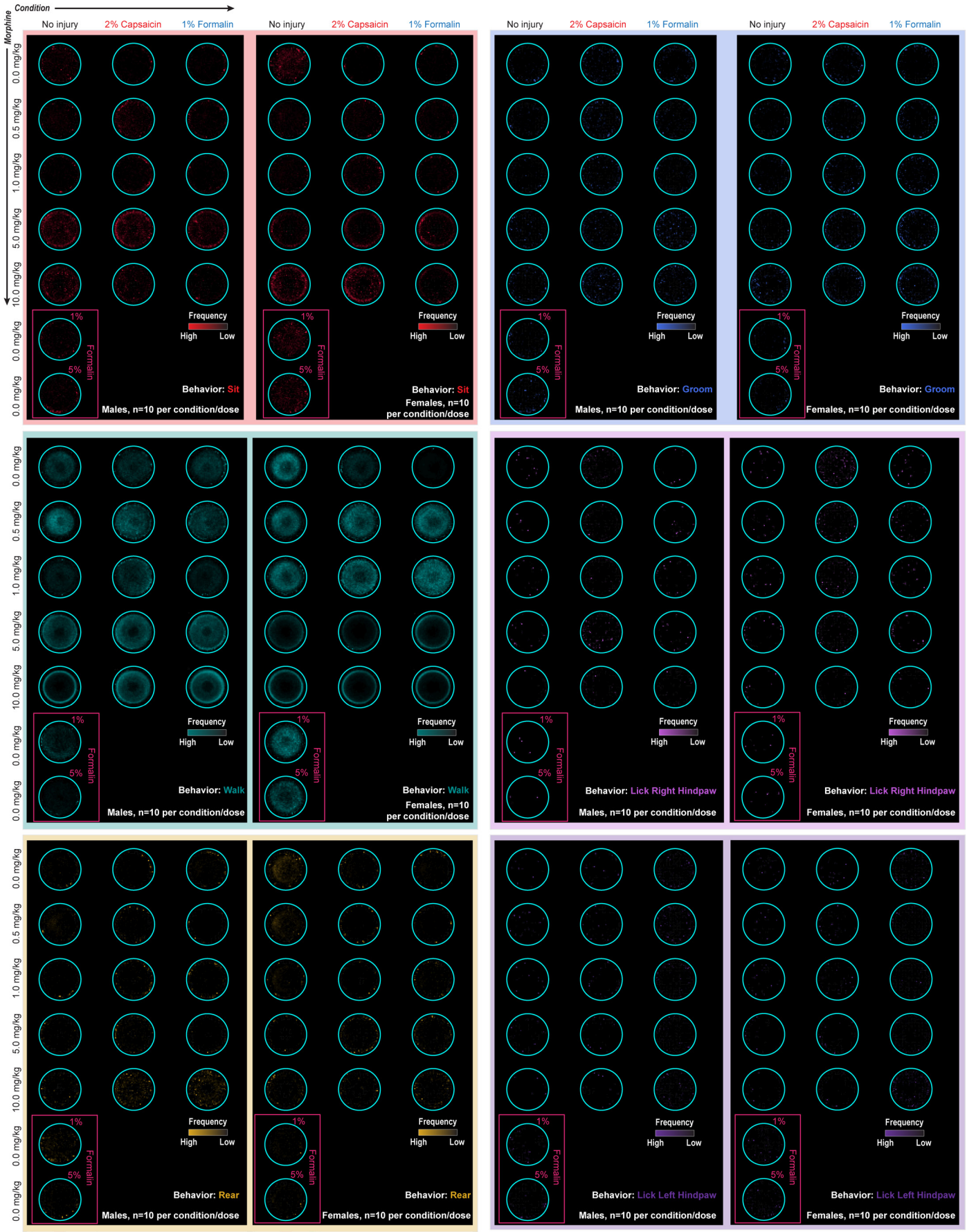

Fig. S5. LUPE-generated maps of behavior repertoire *occurrence frequency locations* within the chamber. (A) The location frequency of any individual behavior occurring within the 10-inch diameter cylinder is shown for male and females,

and for the effects of formalin or capsaicin injuries (X-axis), as well as the effects of subcutaneous doses of morphine sulfate (Y-axis). The six behavior repertoires are: Sit (red), Groom (blue), Walk (green), Lick Right Hindpaw (pink), Rear (yellow), Lick Lef Hindpaw (purple). N=10 mice per sex and per condition.

Fig. S6. LUPE-generated heatmaps of behavior repertoire *transitions* from a current behavior (Y-axis) to the next behavior (X-axis). (A) Male mice transition probabilities. (B) Female mice transition probabilities. N=10 mice per sex and per condition.

Fig. S7. LUPE-generated pie chats of behavior repertoire *percent total frames* for male (A) and female mice (B). N=10 mice per sex and per condition.

Fig. S8. **LUPE-generated bar graphs of behavior repertoire *instances* for male (A) and female mice (B). N=10 mice per sex and per condition.**

Fig. S9. **LUPE-generated bar graphs of behavior repertoire *duration per instance* for male (A) and female mice (B). N=10 mice per sex and per condition.**

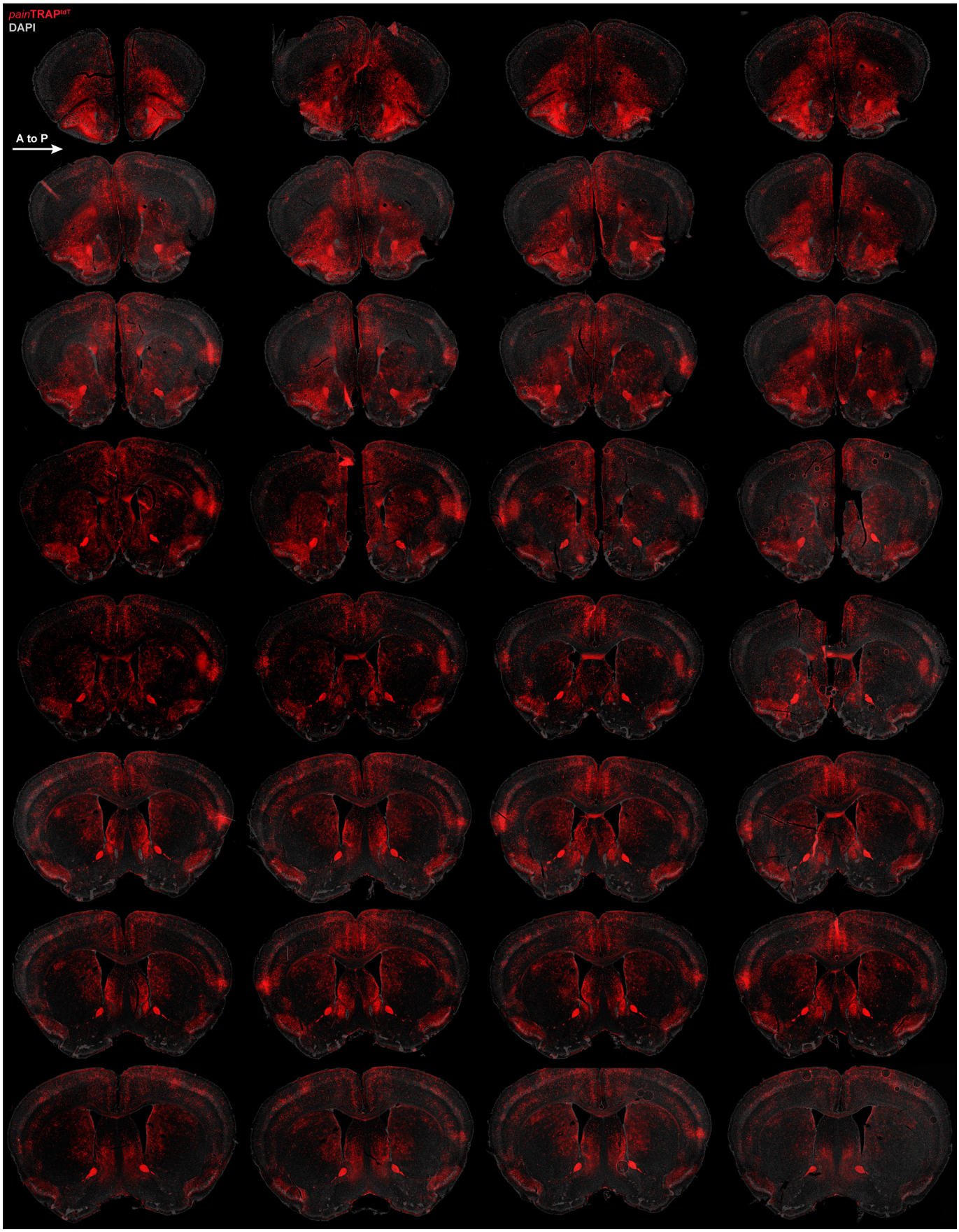

Fig. S10. **Representative images from anterior-to-posterior ACC of n=1 male *pain*TRAP-tdTomato mouse. The A-P coordinates move from left-right to top-bottom.**

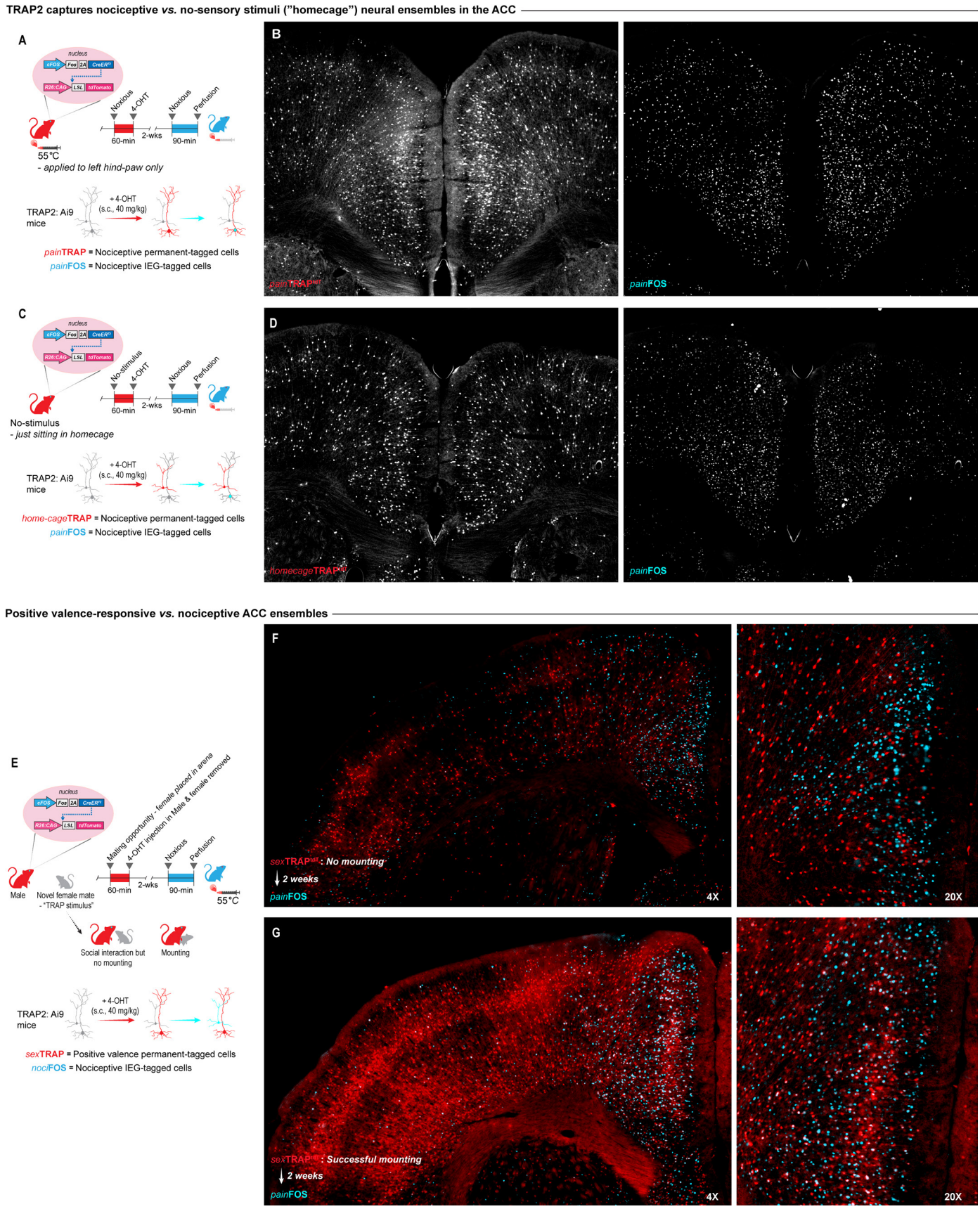

Fig. S11. TRAP2 conditions in the ACC. (A,B) Schematic of the *pain*TRAP-tdTomato protocol and *pain*FOS re-activation, and representative grayscale channel image of tdTomato and FOS. **(C,D)** Schematic of the *home-cage*TRAP-tdTomato protocol and *pain*FOS re-activation, and representative grayscale channel image of tdTomato and FOS. **(E)** Schematic of the *sex*TRAP protocol in sexually naïve, male TRAP2;Ai9 mice given a 1-hour mating opportunity with a female conspecific.

A video camera placed next to the interaction chamber was used to determine if the males mounted the females. **(F)** Representative *sex*TRAP tagged cells in ACC in males that investigeed the females but that did not mount them. **(G)** Representative *sex*TRAP tagged cells in ACC in males that successfully mounted the female.

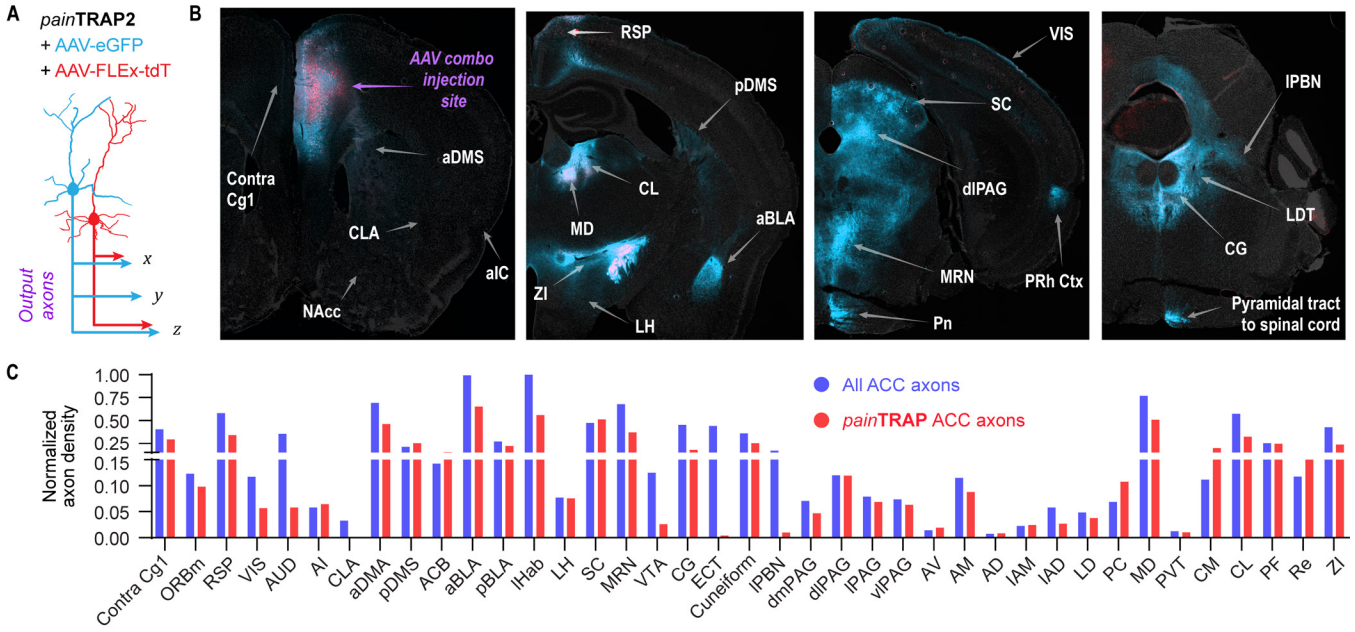

Fig. S12. Mapping nociceptive ACC axonal outputs. (A) Design to label all putative outputs of the ACC (Blue: AAV-*hSyn*-GFP) *vs.* the *pain*TRAP nociceptive cell-types (Red: AAV-*hSyn*-FLEx-tdTomato). (B) Representative images from the ACC injection site and brain-wide location of axons. (C) Quantification of axon densities normalized to the lateral habenula (the area with the largest density of *All ACC axons*).

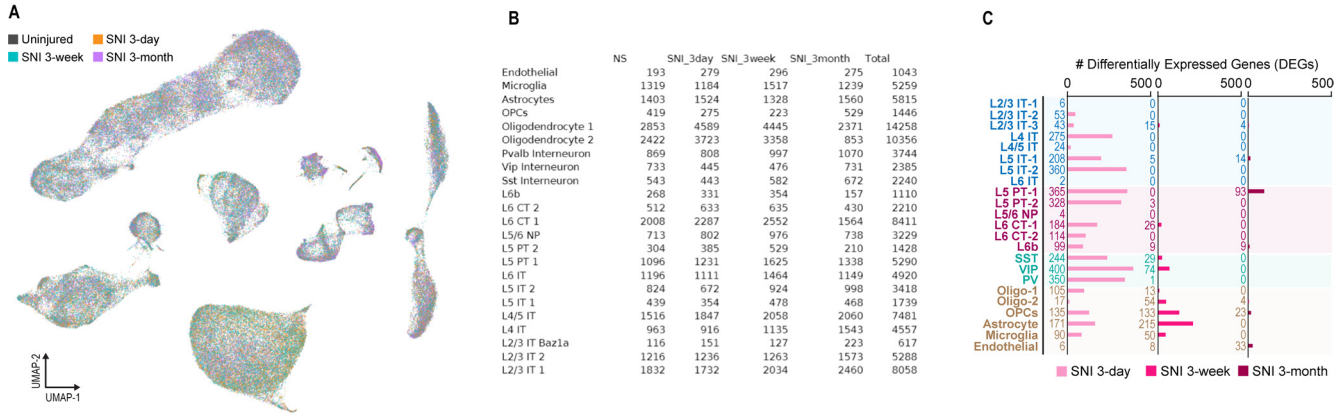

	NS	SNI_3day	SNI_3week	SNI_3month	Total
Endothelial	193	279	296	275	1043
Microglia	1319	1184	1517	1239	5259
Astrocytes	1403	1524	1328	1560	5815
OPCs	419	275	223	529	1446
Oligodendrocyte 1	2853	4589	4445	2371	14258
Oligodendrocyte 2	2422	3723	3358	853	10356
Pvalb Interneuron	869	808	997	1070	3744
Vip Interneuron	733	445	476	731	2385
Sst Interneuron	543	443	582	672	2240
L6b	268	331	354	157	1110
L6 CT 2	512	633	635	430	2210
L6 CT 1	2008	2287	2552	1564	8411
L5/6 NP	713	802	976	738	3229
L5 PT 2	304	385	529	210	1428
L5 PT 1	1096	1231	1625	1338	5290
L6 IT	1196	1111	1464	1149	4920
L5 IT 2	824	672	924	998	3418
L5 IT 1	439	354	478	468	1739
L4/5 IT	1516	1847	2058	2060	7481
L4 IT	963	916	1135	1543	4557
L2/3 IT Baz1a	116	151	127	223	617
L2/3 IT 2	1216	1236	1263	1573	5288
L2/3 IT 1	1832	1732	2034	2460	8058

Fig. S13. (A) Intermixed nuclei with UMAP space from Uninjured mice and the three post-Spared Nerve Injury (SNI) timepoints: 3-days, 3-weeks and 3-months. **(B)** The number of analyzed nuclei per injury condition for each cell-type cluster. **(C)** The number of DEGs per cell-type for each injury condition compared to the Uninjured condition.

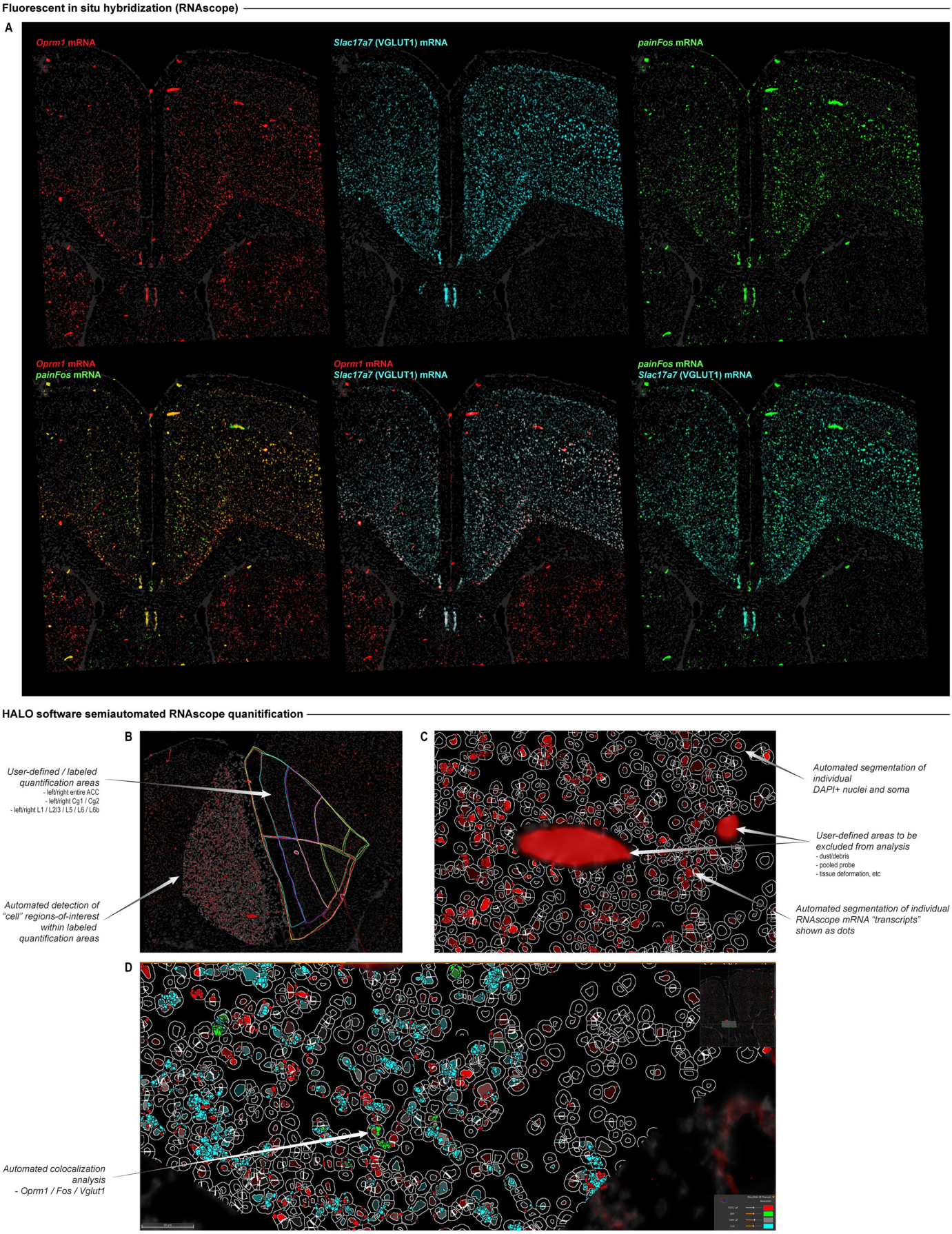

Fig. S14. Fluorescent in situ hybridization (FISH) for *Oprm1* cell-types across ACC subregions and layers. (A) Representative 20X stitched images for *Oprm1*, *painFos* and *Slc17a7* mRNA using RNAscope FISH. **(B-D)** HALO deep-learning software for histology quantification within user-defined areas, such as ACC layers.

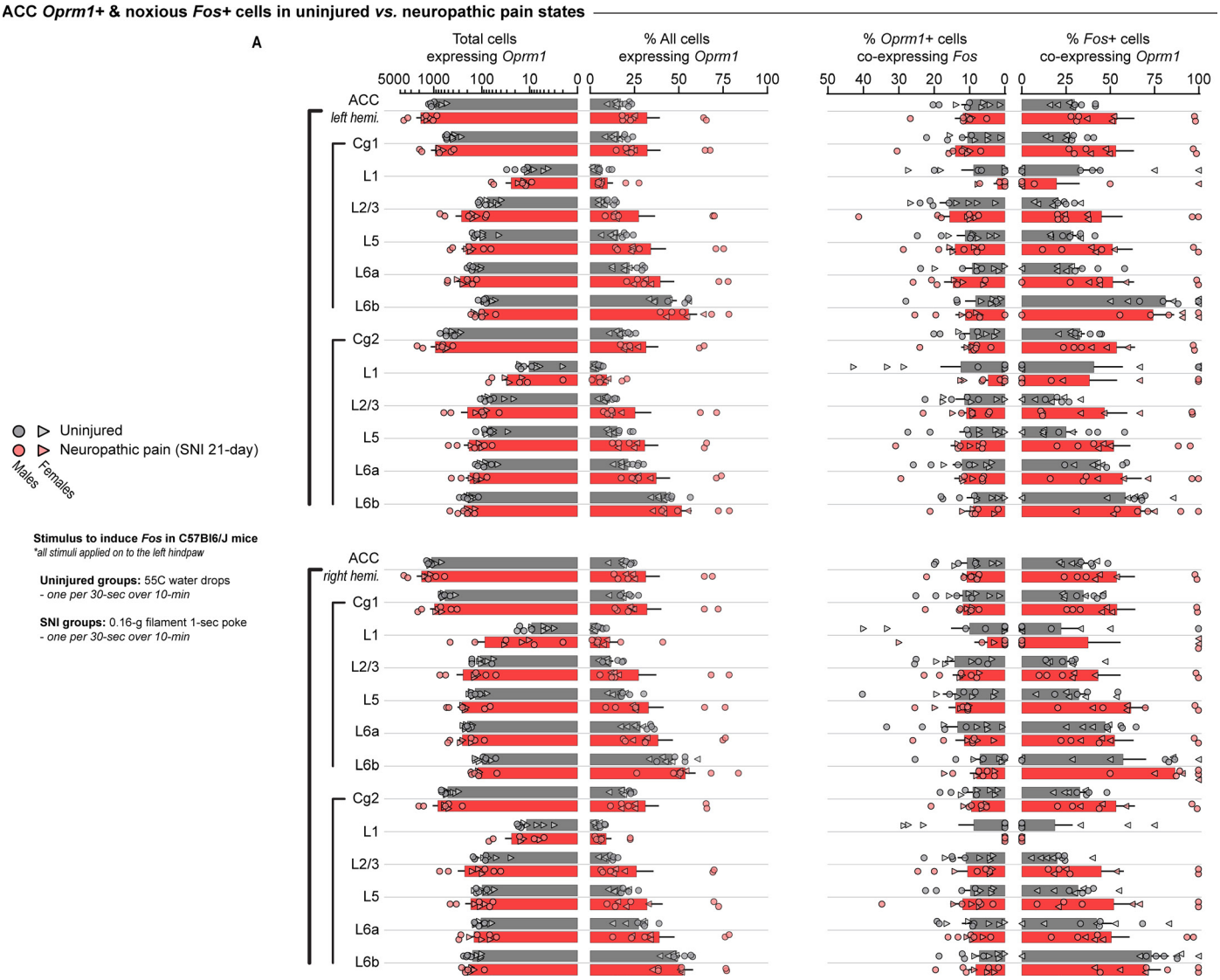

Fig. S15. *Oprm1* mRNA quantification across ACC subregions and layers in male and female mice, with or without neuropathic pain. N=8 per group/condition (n=5 male and n=3 female), all counted using HALO.

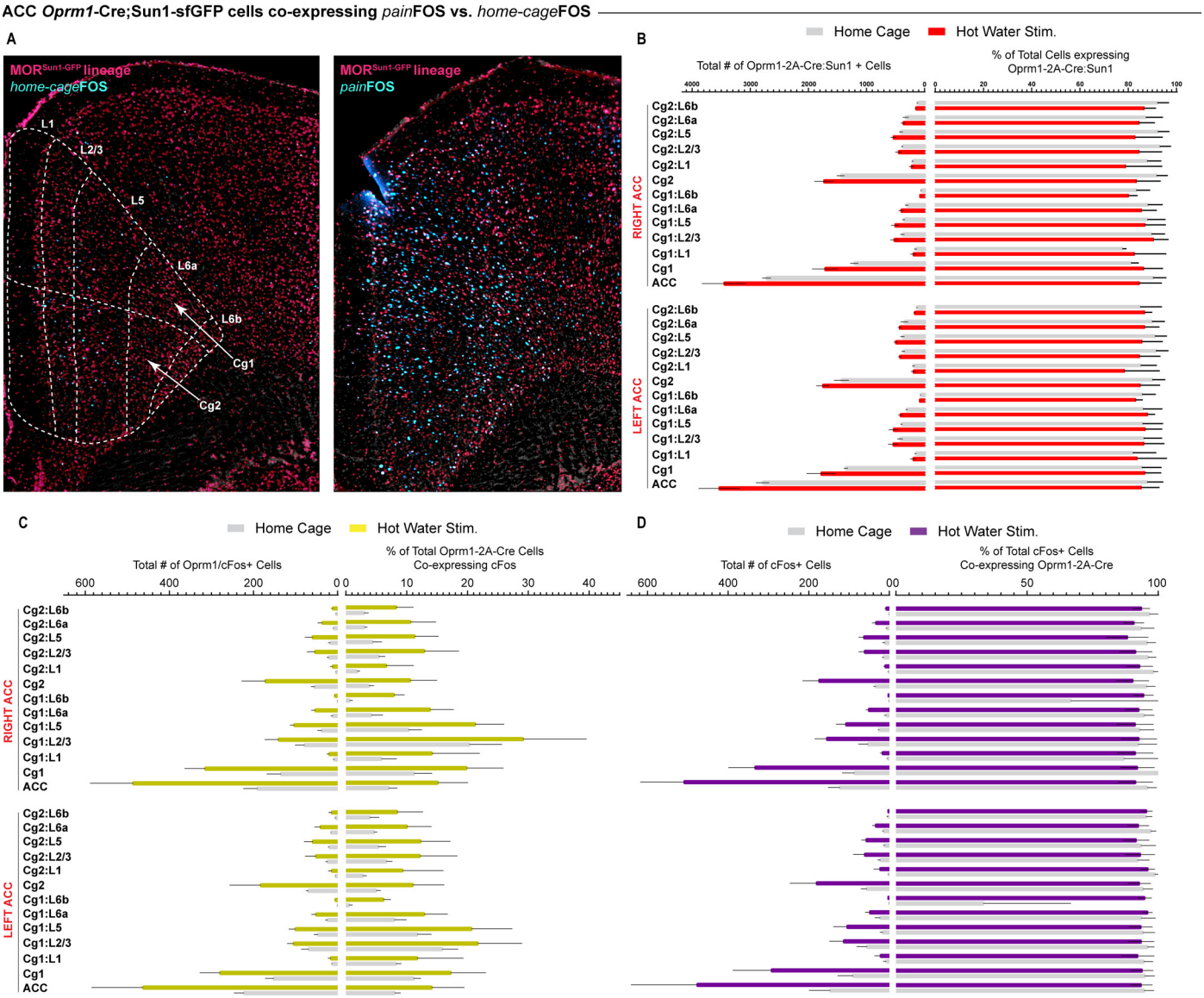

Fig. S16. MOR-lineage cell quantification across ACC subregions and layers in uninjured male and female mice. (A) Representative images from *Oprm1*-2A-Cre;Sun1-sfGFP mice (MOR lineage labeled cells) with basal FOS (home-cage) or *pain*FOS expression (N=3 male and 3 female per group, per condition). **(B-D)** HALO quantifications for overlapping MOR-lineage and *pain*FOS or *home-cage*FOS-expressing cell-types.

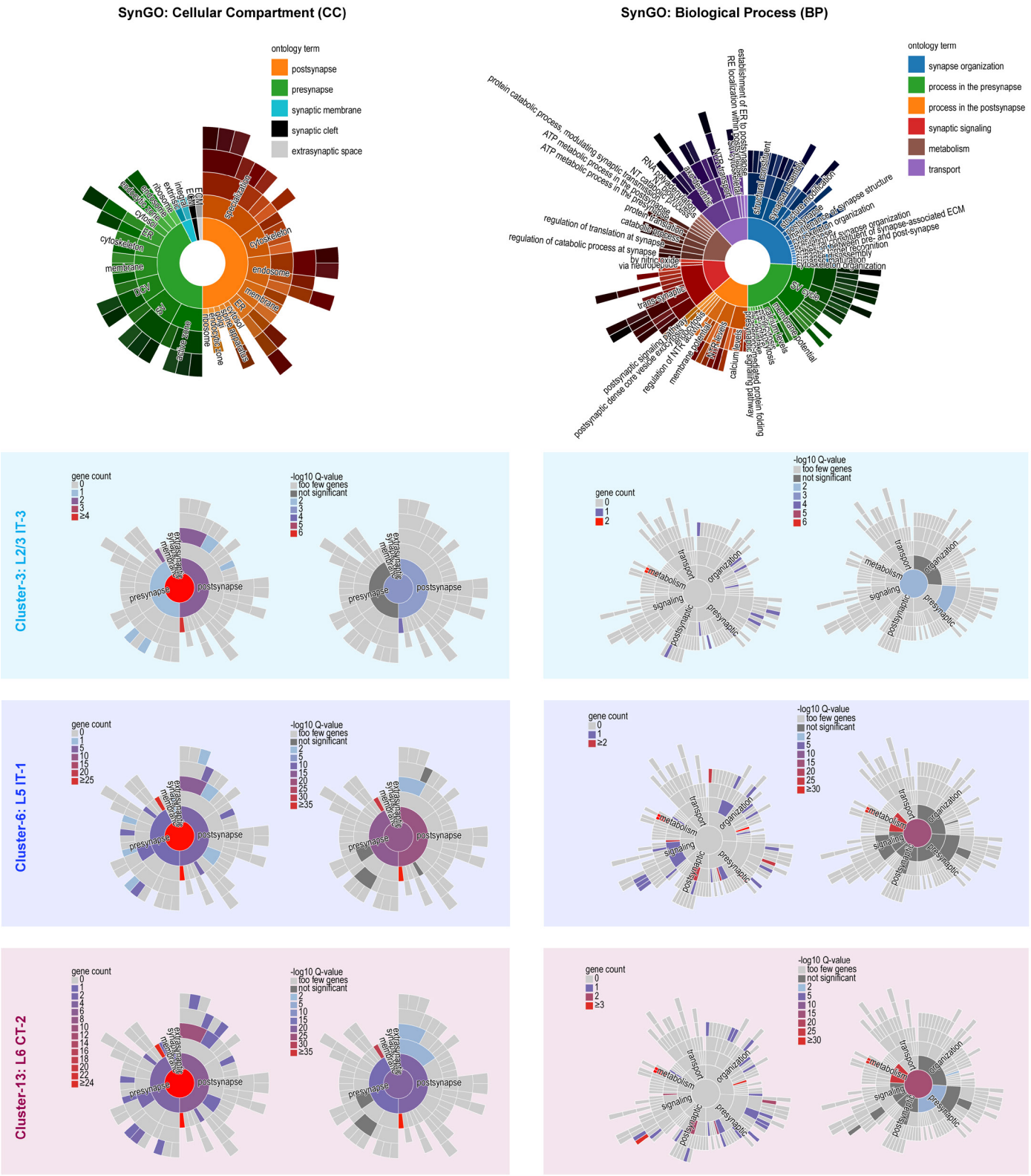

Fig. S17. Synaptic Gene Ontology (SynGO) analysis for differential expressed genes (DEGs) in ACC nociceptive cell-types (L2/3 IT-3 (light blue), L5 IT-1 (dark blue), L6 CT-2 (maroon) 3-days after SNI compared to Uninjured. *Left*: DEG gene count and logQ10 enrichment related to Cellular Components, such as presynapse. *Right*: DEG gene counts and logQ10 enrichment related to Biological Processes, such as vesical recycling.

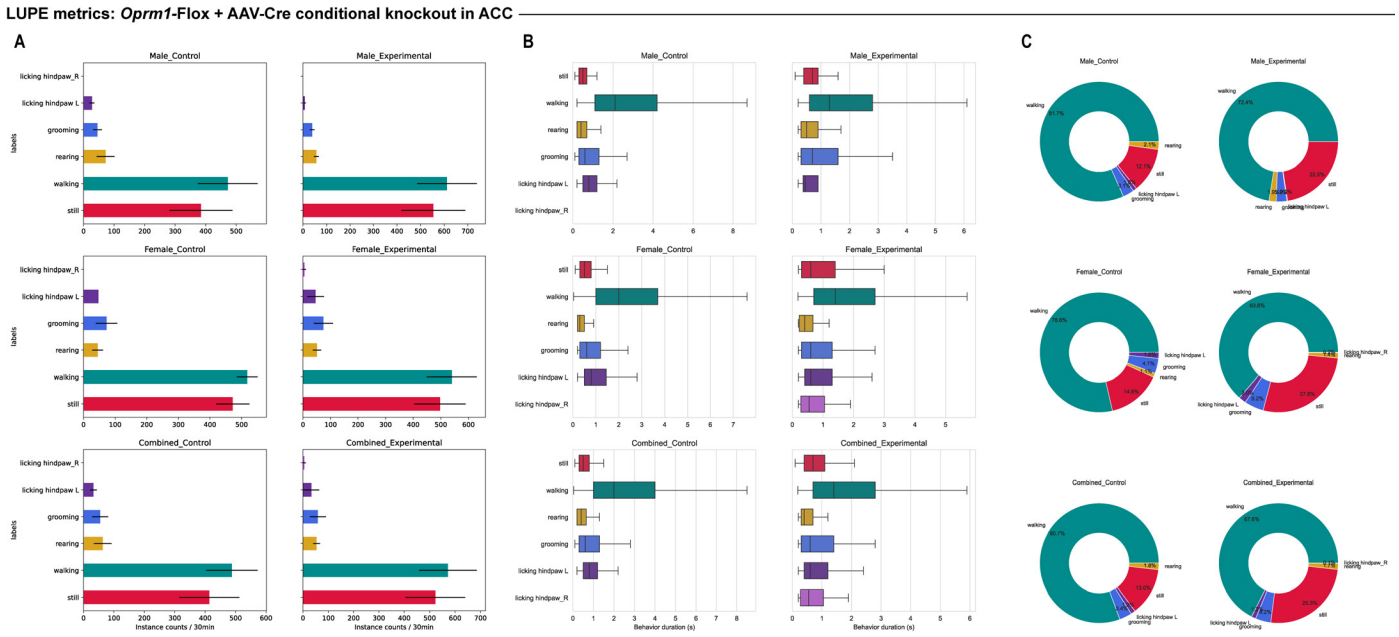

Fig. S18. LUPE-generated graphs of behavior repertoire instances (A), duration per instance (B), and percentage of frames from a 30-min recording (C) in male and female *Oprm1*-Flox/Flox mice injected with either AAV-GFP (Control) or AAV-GFP-Cre (Experimental).

Fig. S19. LUPE-generated graphs of behavior repertoire instances (A,D), duration per instance (B, E), and percentage of frames from a 30-min recording (C, F) in male and female MOR KO mice injected with either AAV-FLEx-GFP (Control) or AAV-FLEx-hMOR-mCherry (Experimental). Panels A-C are mice injected only with morphine (0.5-mg/kg, i.p.), while Panels D-F are mice injured with 1% formalin (i.pl) + morphine (0.5-mg/kg, i.p.).

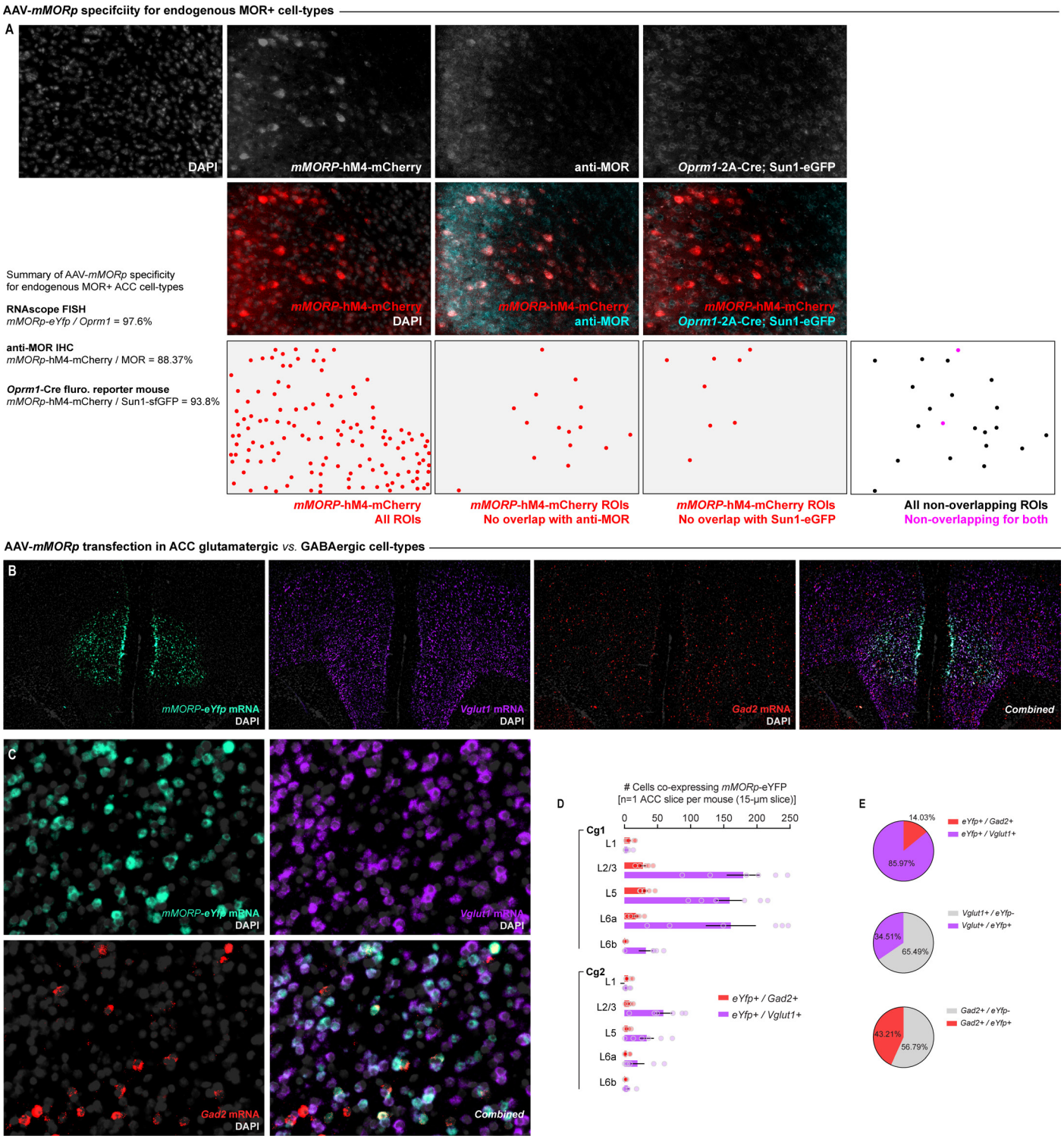

Fig. S20. AAV-mMORp transfection in ACC Oprm1+ cell-types. **(A)** AAV-mMORp-hM4-mCherry DREADD expression in Cg1 ACC of Oprm1-2A-Cre;Sun1sf-GFP mice co-stained for anti-MOR immunoreactivity. **(B)** RNAscope FISH for eYfp (AAV-mMORp-eYFP), Slc17a7 (Vesicular glutamate transporter 1, VGLUT1) and Gad2 (Glutamic acid decarboxylase 2, GAD2). **(C)** 20X images of panel B. **(D)** HALO quantification of eYfp overlaps with Slac17a7+ and Gad2+ cells. N=6 separate hemisphere injection sites from n=3 mice.

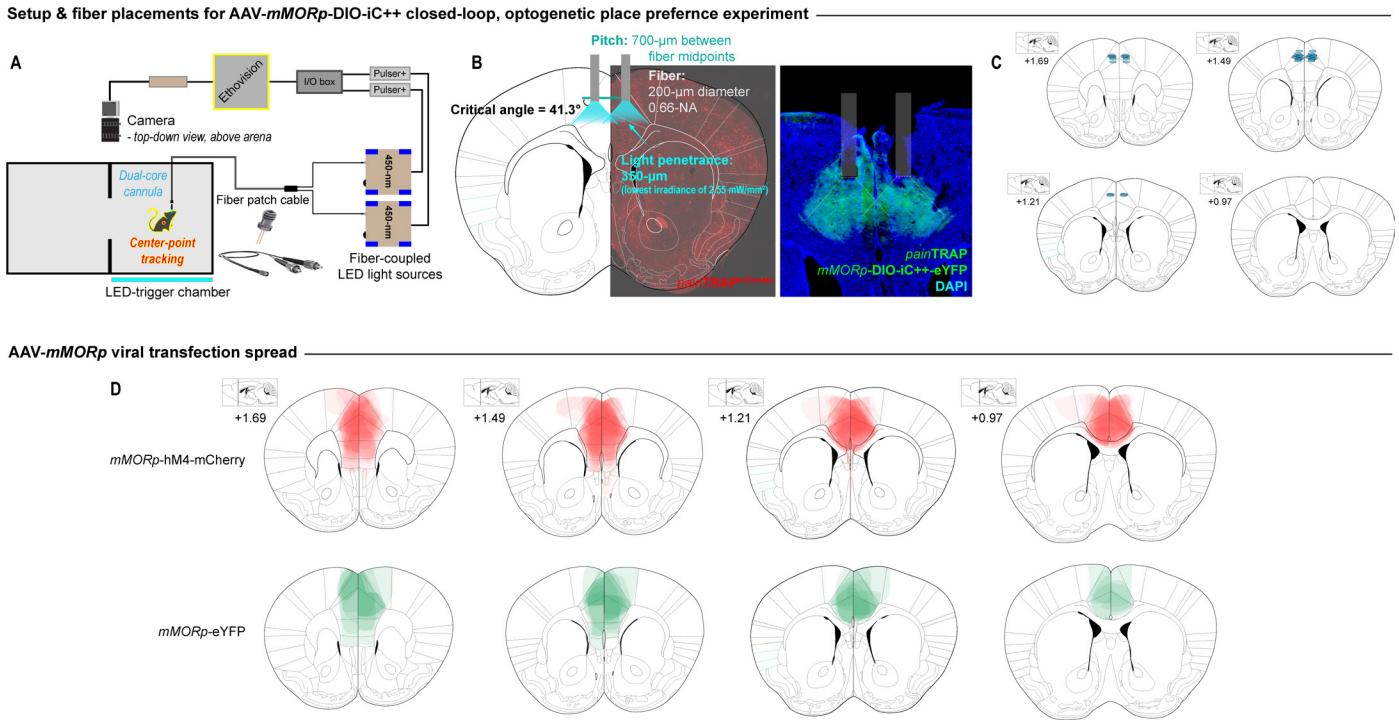

Fig. S21. (A) Real-time place preference setup with Ethovision triggering an external LED system to administer blue light to the ACC of *pain*TRAP2 mice transfected with the inhibitory chloride channel opsin, AAV-mMORp-DIO-iC++ . **(B)** Bilateral fiber optic design for LED light penetrance to the ACC (left), with a representative image of the cannula tracks over the dorsal Cg1 ACC expressing iC++ in *pain*TRAP neurons. **(C)** Cannula tip placements, as determined from post-hoc histology for all mice included in the final analysis. **(D)** Viral spread maps for AAV-*mMORp*- eYFP vs. hM4-mCherry.

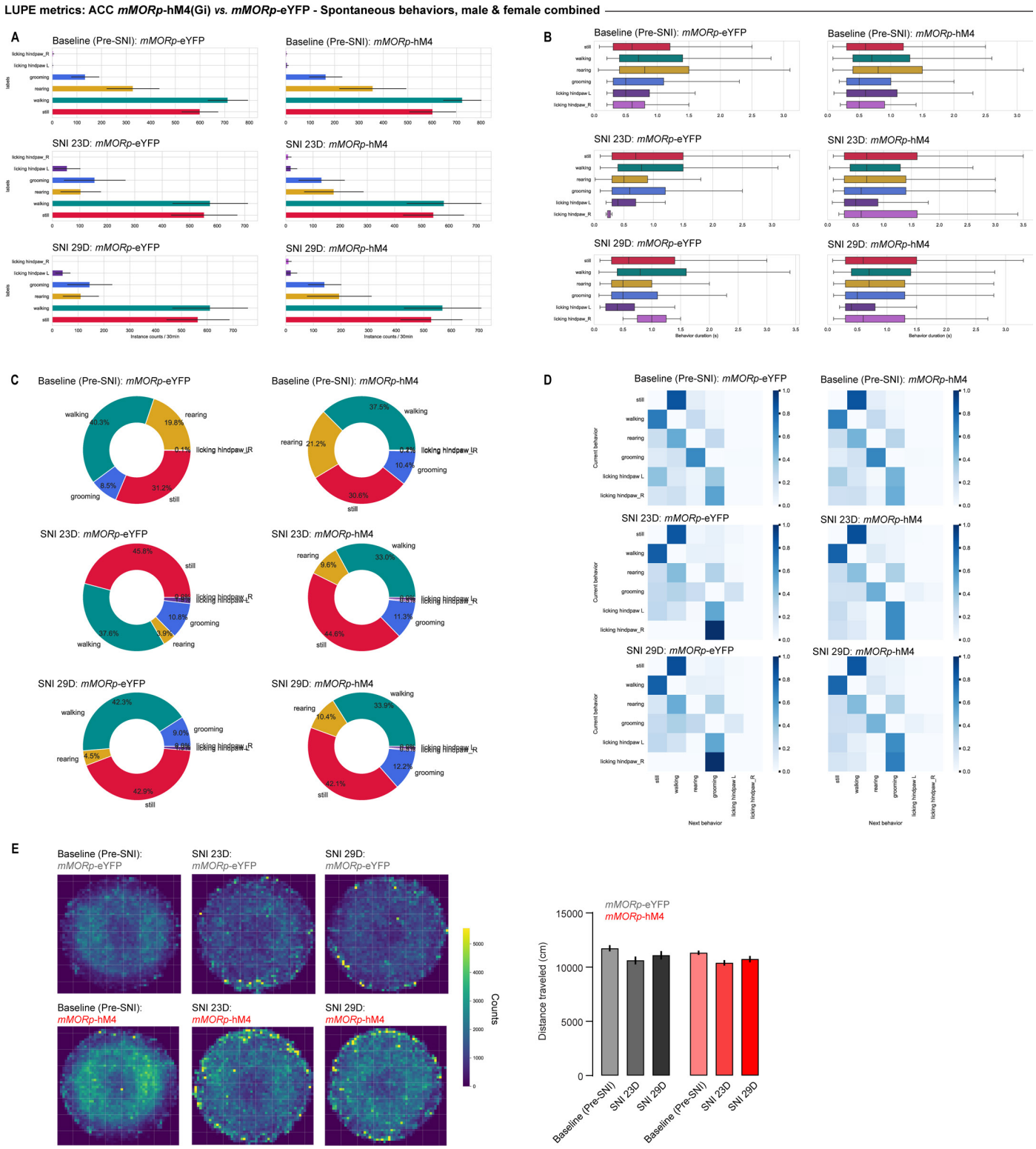

Fig. S22. LUPE-generated graphs of behavior repertoire **(A)** instances, **(B)** duration per instance, **(C)** percentage of frames from a 30-min recording, and **(D)** behavior transition probability in all male and female C57Bl6/J mice combined, before and after SNI to the left sciatic nerve, and the effect of acute (21D timepoint) and chronic (28D timepoint) ACC DREADD inhibition of MOR+ cell-types. Mice were injected with either AAV-*mMORp*-eYFP (Control) or AAV-*mMORp*-hM4-mCherry (Experimental). **(E)** Group average *Walk* behavior instance frequency mapped across the LUPE chamber. **(F)** Distance traveled over 30-min in mice injected with DCZ (0.3-mg/kg).

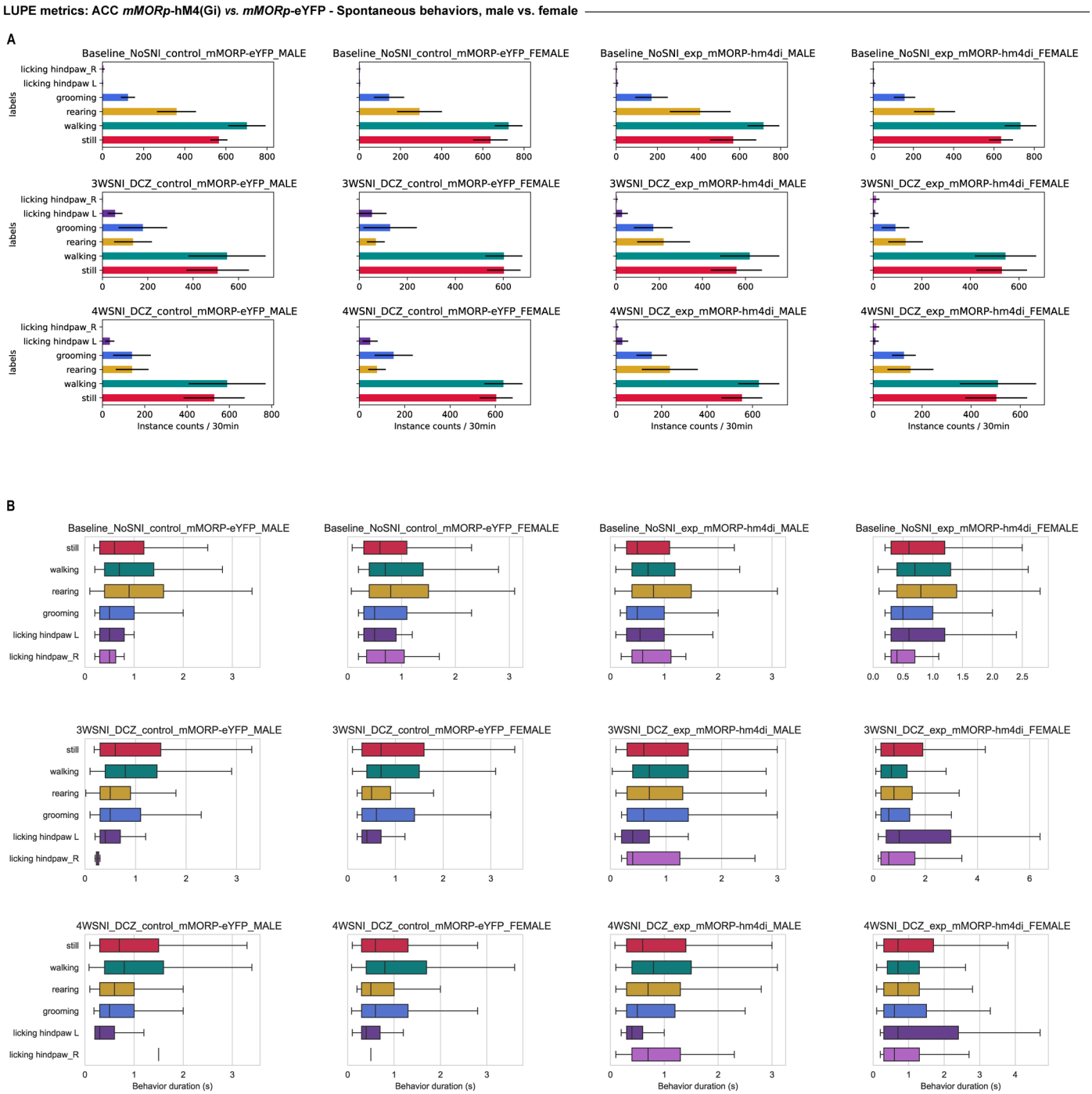

Fig. S23. Same data as in Fig. S22 A and B but shown for male and females separately.

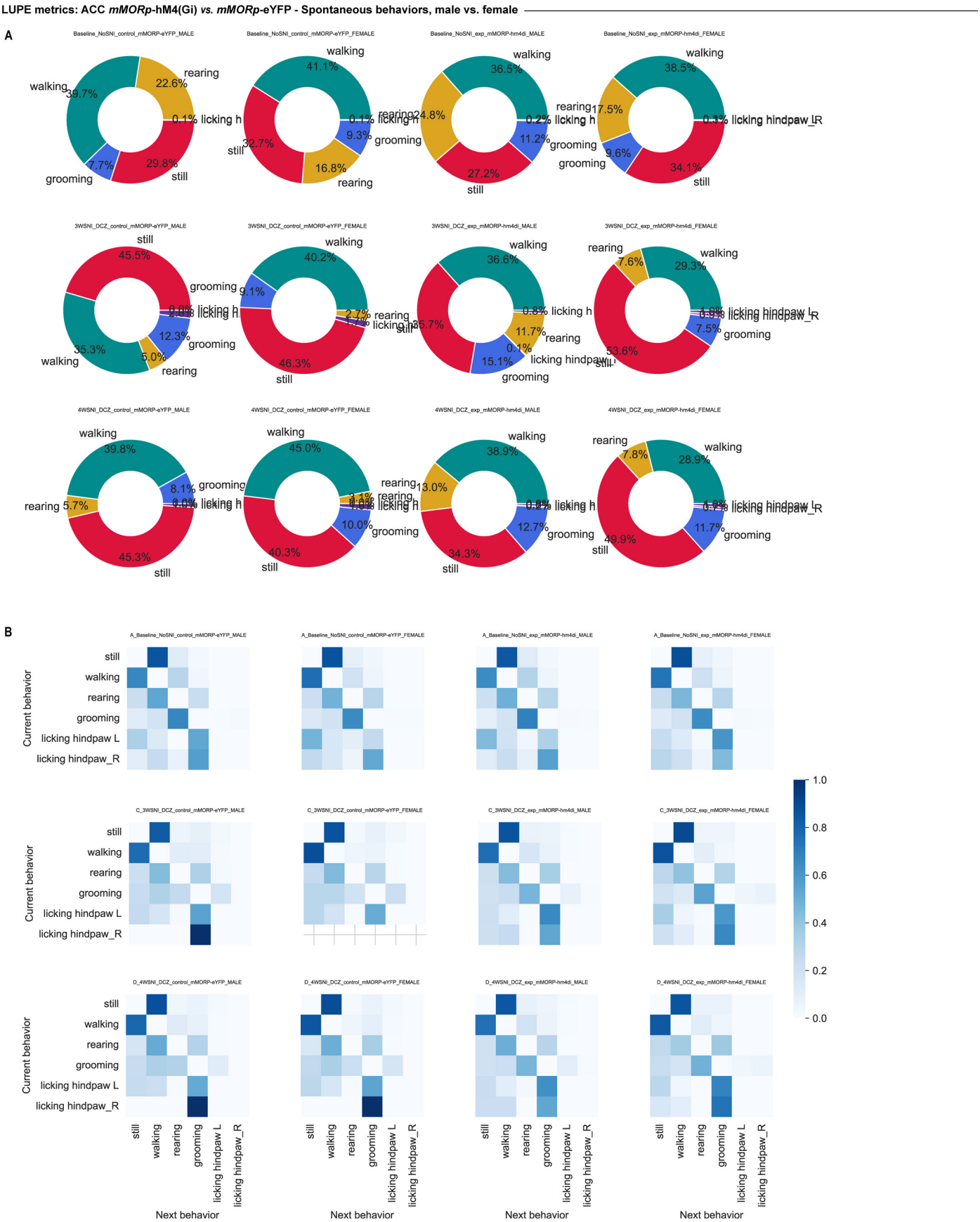

Fig. S24. Same data as in Fig. S22 C and D but shown for male and females separately.